

Nomenclature

Roman Symbols

D_r Relative density

E Young's modulus of the material

Greek Symbols

ν Poisson's ratio (or) Fluid viscosity

Φ Dilatancy angle

Subscripts

y Yield or failure

Draft - v1.0

Tuesday 20th January, 2015 – 10:11

Chapter 4

Multi-scale modelling of dry granular flows

4.1 Introduction

In nature, instabilities of slopes or cliffs can manifest themselves in dramatic events involving the sudden release of a large mass of soil. The prediction of these catastrophic events presents several challenges, one difficulty being our incomplete understanding of granular flow dynamics (Rondon et al., 2011). Understanding the mechanics is of particular importance for risk assessment. Small scale laboratory experiments are usually unable to properly capture the dynamics of geophysical events. However, they can be useful to precisely study the physical mechanisms, which may play a crucial role in real flows (Iverson, 1997).

Conventionally, granular materials such as soils are modelled as a continuum. On a macroscopic scale, granular materials exhibit many collective phenomena and the use of continuum mechanics to describe the macroscopic behaviour can be justified. However on a grain-scale, granular materials exhibit complex solid-like and/or fluid-like behaviour depending on how the grains interact with each other. Numerical studies at grain-scale allow a precise understanding of the internal flow structure. However, even in simplified geometries such as those investigated in the laboratory-scale experiments, DEM suffers from a serious short-coming in the number of grains that can be simulated in a reasonable time. This is a critical issue for more complex geometries or when granular processes which occur on a long time-scale are considered. For this reason, most numerical studies are performed in 2D or simple particles shapes and size distributions are considered.

Classical modelling strategies based on the finite element method (FEM) cannot be used for the simulation of very large deformations due to mesh distortion effects. In various

25 applications of FEM, this problem is treated by means of technical tools such as re-meshing.
 26 These methods are, however, not robust and lead to round-off errors and are sensitive to
 27 the mesh characteristics. Recent works on granular materials suggest that a continuum law
 28 may be incapable of revealing in-homogeneities at the grain-scale level, such as orientation
 29 of force chains, collapse of local voids and grain rearrangements, which are purely micro-
 30 structural effects (Rycroft et al., 2009). Discrete element approaches are capable of simulating
 31 granular materials as discontinuous systems allowing one to probe into local variables such as
 32 position, velocities, contact forces, etc. The fundamental question is how to model granular
 33 materials which exhibit complex phenomena. It is important to understand the mechanics
 34 of granular flows and the ability and limitations of continuum methods in modelling the
 35 granular flow dynamics.

36 4.2 Granular column collapse

37 The collapse of a granular column, which mimics the collapse of a cliff, has been extensively
 38 studied in the case of dry granular material (Hogg, 2007; Kerswell, 2005; Lajeunesse et al.,
 39 2004; Lo et al., 2009; Lube et al., 2005; Staron and Hinch, 2007; Zenit, 2005). The granular
 40 column collapse experiment involves filling a rectangular channel of height H_0 and width L_0
 41 with a granular material of mass m (??). The granular column is then released *en masse* by
 42 quickly removing the gate, thus allowing the granular material to collapse onto a horizontal
 43 surface, forming a deposit having a final height H_f and length L_f . Despite the complexity
 44 of the intermediate flow dynamics, experimental investigations have shown that the flow
 45 evolution, the spreading velocity, the final extent of the deposit, and the energy dissipation
 46 can be scaled in a quantitative way independent of the substrate properties, grain size, density,
 47 the shape of the granular material and the released mass (Lajeunesse et al., 2005; Lube
 48 et al., 2005; Staron and Hinch, 2007). Granular collapse has also been studied using DEM,
 49 which allows precise measurement of the internal flow structure (Lo et al., 2009; Staron and
 50 Hinch, 2007; Staron et al., 2005; Utili et al., 2014). Power laws relating the final run-out and
 51 height to the initial aspect ratio ($a = H_0/L_0$) of the column were observed. These findings
 52 immediately pose a question: are these simple scaling laws fortuitous, an oversimplification,
 53 or in fact indicative of a simple dynamical balance?

54 Granular flows are conventionally modelled as a frictional dissipation process in contin-
 55 uum mechanics but the lack of influence of inter-particle friction on the energy dissipation
 56 and spreading dynamics (Lube et al., 2005) is surprising. However, Kerswell (2005) showed
 57 the run-out behaviour has a clear material dependence. Although, the collapse of a granular
 58 column on a horizontal surface is a simple case of granular flow, a proper model that describes

the flow dynamics is still lacking. Simple mathematical models based on conservation of horizontal momentum capture the scaling laws of the final deposit, but fail to describe the initial transition regime. From a theoretical point of view, the spreading has been described using depth averaged equations (Kerswell, 2005; Larrieu et al., 2006). The depth-averaged and Saint-Venant equations, however, struggle to recover the precise dynamic behaviour of the system (Warnett et al., 2013) and only succeed in predicting the scaling observed for an aspect ratio less than one. Describing the behaviour of cases with larger aspect ratios and capturing the initial stage of the collapse, when the grains experience a rapid change of direction from vertical to horizontal, remain open challenges.

In the present study, multi-scale numerical modelling, i.e. grain-scale modelling and continuum analyses, of the quasi-two-dimensional collapse of granular columns are performed using two-dimensional the Discrete Element Method (DEM) and the Generalised Interpolation Material Point Method (GIMP method). The GIMP method, a hybrid Eulerian–Lagrangian approach, with a Mohr-Coloumb failure criterion is used to describe the continuum behaviour of the granular column collapse. Whereas, the micro-mechanics of the flow is captured using DEM simulations. In this section, the run-out behaviour of quasi-two-dimensional collapse using both MPM and DEM will be studied for initial aspect ratios varying from 0.2 to 10. The flow kinematics and the run-out behaviour between the grain-scale and the continuum simulations highlights the limitations of the continuum approach in modelling dense granular flows and their ability in capturing the complex flow kinematics which are due to micro-scale rheology.

4.2.1 Numerical set-up

In this study, the numerical set-up of granular column collapse is analogous to the experimental investigation performed by Lajeunesse et al. (2004). The experimental configuration of Lajeunesse et al. (2004) is shown in ???. A granular material of mass m was poured into a container to form a rectangular heap of length L_0 and height H_0 . The internal friction angle and the wall friction between the wall and the glass beads measured by Lajeunesse et al. (2004) are listed in table 4.1. The gate was then quickly removed to release the granular mass that spreads in the horizontal channel until it comes to rest. The final run-out distance L_f and the collapsed height H_f were measured. The run-out distance and collapse height exhibit a power law relation with the initial aspect ratio ‘ a ’ ($= H_0/L_0$) of the column.

Granular materials when released suddenly on a horizontal surface exhibit transient flow. In this study, the mechanism of flow initiation, spreading dynamics and energy dissipation are studied for varying initial aspect ratios of the granular column. The particle size distribution (PSD) is one of the most important factors controlling landslide initiation and soil permeabil-

Table 4.1 Material properties of glass ballotini used in granular column collapse (Lajeunesse et al., 2004).

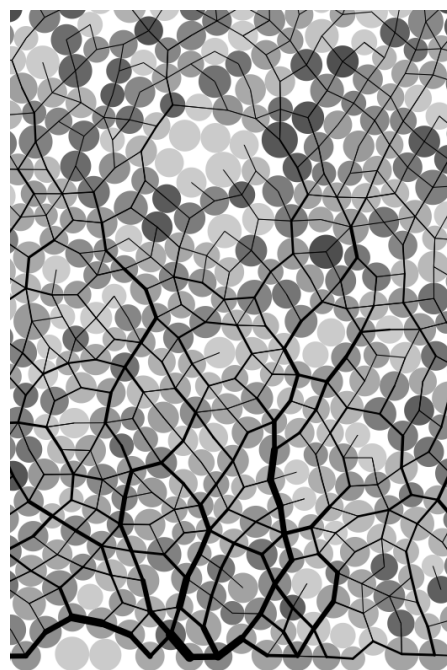
Parameter	Value
Mean grain diameter	1.15 mm
Repose angle	$22 \pm 0.5^\circ$
Avalanche angle	$27.4 \pm 0.5^\circ$
Wall friction angle	$24.8 \pm 0.2^\circ$

94 ity (Utili et al., 2014). Due to the non-availability of the PSD used in the experiment, a PSD
 95 curve was generated that matches the range of grain size used in the experiment. A cumula-
 96 tive β distribution (described in ??) was used to generate a graded sample with a mean grain
 97 diameter of 1.15mm (figure 4.1b). The DEM sample was composed of ~ 3000 disks with a
 98 uniform distribution of diameters by volume fractions in the range $[d_{min}, d_{max}] = 0.92 - 1.38$
 99 mm with poly-dispersity $r = \frac{d_{max}}{d_{min}} = 1.5$. The number of DEM grains used in this study is
 100 relatively small due to the practicality of simulating coupled fluid-grain interactions at a large
 101 scale. Coupled fluid-grain simulations are computationally very expensive. Nevertheless,
 102 this study utilises sophisticated hardware and software technologies, available at this time,
 103 to simulate the largest possible REVs that provide reasonable description of granular flow
 104 behaviour. Marketos and Bolton (2009) observed that the boundary-grain interface may
 105 influence the fabric and voids ratio of the material in contact. The boundary effect is found to
 106 extend up to 2 mean grain diameters from a smooth, solid boundary over which the granular
 107 material had been placed. Sufficient number of grains are used to avoid any such boundary
 108 effects.

109 The granular column was prepared by allowing randomly placed grains to undergo
 110 ballistic deposition with a constant potential head between layers of soil grains. A snapshot
 111 of the sample generated is shown in figure 4.1a. A DEM sample with soil grains arranged in
 112 a regular hexagonal lattice was also used to understand the influence of crystallisation and
 113 jamming on the run-out behaviour.

114 The overlap between grains is determined by the stiffness k_n of the spring in the normal
 115 direction. Typically, an average overlap in the range 0.1 to 1.0% is desirable (Zenit, 2005)
 116 and the spring constant is chosen to produce grain overlaps in this range. The stiffness is

4.2 Granular column collapse



(a) A snapshot of a DEM sample prepared using ballistic deposition technique.

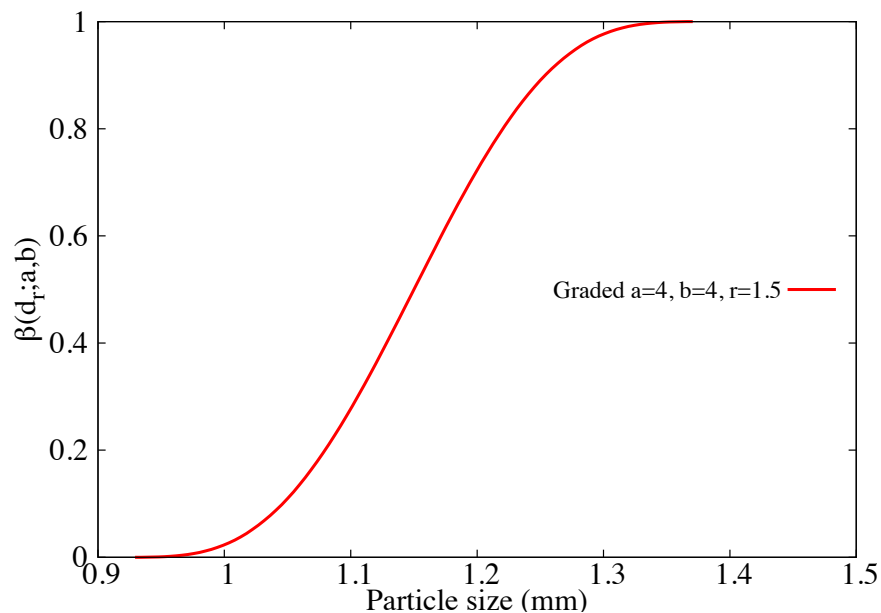
(b) Particle size distribution of the DEM sample generated using the cumulative β distribution approach.

Figure 4.1 The DEM sample used for the granular column collapse simulation and its grain size distribution curve.

¹¹⁷ determined as

$$\text{118} \quad k_n = \frac{2\pi G}{(1-\nu) [2\ln(\frac{2r}{A}) - 1]} \quad (4.1)$$

$$\text{119} \quad A = \left[\frac{2r(1-\nu)f_n}{\pi G} \right]^{\frac{1}{2}}, \quad (4.2)$$

¹²⁰ where f_n is the normal contact force; G is the shear modulus; ν is the Poisson's ratio and r is
¹²¹ the radius of the grain. A simpler form of stiffness for a spherical grain is defined as

$$\text{123} \quad k_n = 4Er, \quad (4.3)$$

¹²⁴ where E is the Young's modulus of the material and r is the radius of the grain. Cambou et al.
¹²⁵ (2009) observed that the contact model has negligible influence on the run-out behaviour of
¹²⁶ rapid granular flows. The granular collapse simulations performed using non-linear Hertz-
¹²⁷ Mindlin contact model and the linear-elastic contact model showed no significant difference
¹²⁸ in the granular flow behaviour (Utili et al., 2014). A linear-elastic contact model is used in the
¹²⁹ present study due to its simplicity and lower computation time requirement. The maximum
¹³⁰ tangential force is limited by the Mohr-Coloumb criterion.

¹³¹ Staron and Hinch (2007) observed that the coefficient of restitution ε dramatically changes
¹³² the behaviour of the system as $\varepsilon \rightarrow 1$; in particular, this dramatic change is expected to
¹³³ become more important for increasing values of a . On the contrary, for $\varepsilon \leq 0.8$, the influence
¹³⁴ of the coefficient of restitution becomes negligible. In the present study, a value of 0.75 is
¹³⁵ adopted as the coefficient of restitution, similar values were adopted by Girolami et al. (2012)
¹³⁶ and Zenit (2005). The normal damping coefficient C_n is appropriately chosen to achieve the
¹³⁷ required coefficient of restitution ε :

$$\text{138} \quad C_n = 2\gamma\sqrt{m_{ij}k_n}, \quad (4.4)$$

$$\text{139} \quad \text{where } \gamma = -\frac{\ln(\varepsilon)}{\sqrt{\pi^2 + \ln^2(\varepsilon)}}, \quad \text{and } m_{ij} = \frac{m_i m_j}{m_i + m_j}. \quad (4.5)$$

¹⁴⁰ The micro-mechanical parameters used in this study are presented in table 4.2. A rolling
¹⁴¹ resistance was adopted in order to model the shape effect of non-spherical grains (Iwashita
¹⁴² and Oda, 1998). Due to the unsteady nature of the flow, the grains get dispersed on the
¹⁴³ horizontal plane as discrete bodies start to separate from the main mass, hence the run-out
¹⁴⁴ distance is calculated as the position of the farthest grain which has at least one contact with
¹⁴⁵ the main mass.

4.2 Granular column collapse

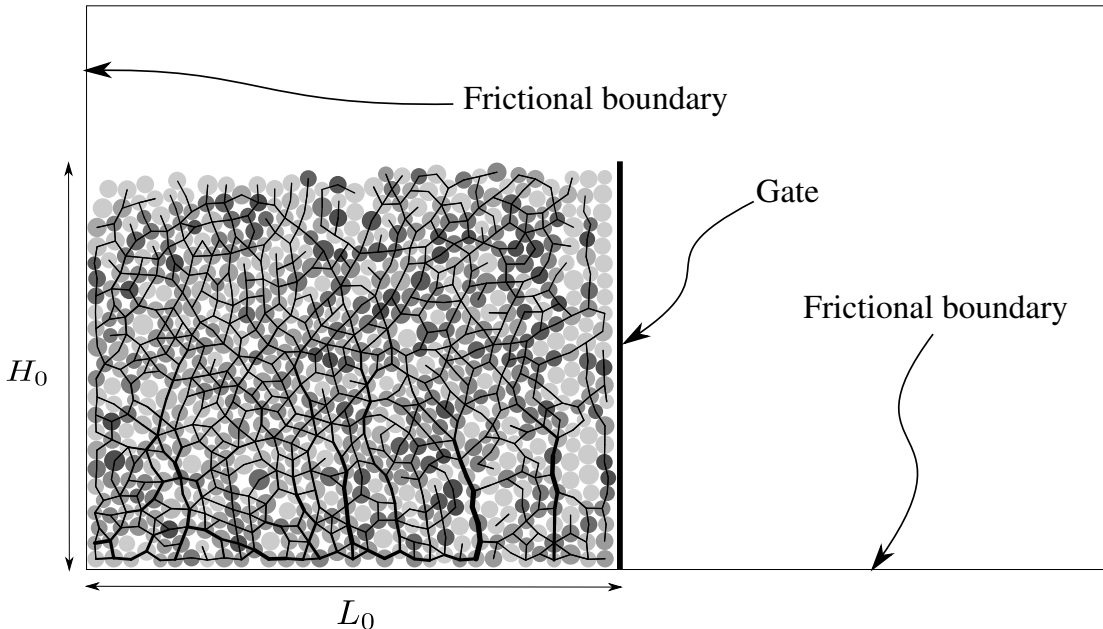


Figure 4.2 DEM set-up for a granular collapse simulation ($a = 0.8$). Shows the grains in a stable state under the influence of gravity.

The configuration of the granular column collapse using DEM is show in figure 4.2 for 147
a column with an initial aspect ratio of 0.8. The soil grains were packed using ballistic 148
deposition technique once a stable state was reached, the gate was opened allowing the 149
granular column to collapse and flow. Frictional boundaries were specified on the left and 150
the bottom boundaries. 151

The GIMP method with a Mohr-Coloumb constitutive model was used to simulate 152
plane strain collapse of granular columns. Crosta et al. (2009) observed that the Mohr- 153
Coloumb model with non-associate flow rule is able to capture granular collapse dynamics 154
and models the strong vertical motion. This method does not suffer the limitations of typical 155
shallow water equation techniques. In order to understand the ability and limitations of 156
continuum approaches in capturing the local rheology, it is important to scale the grain-scale 157
material properties, such as the inter-particle friction and stiffness, to the continuum scale 158
(macroscopic friction and Young's modulus). Crosta et al. (2009) observed that the friction 159
angle plays a significant role on the run-out behaviour. 160

In the MPM simulations, the granular flow was assumed to be in the critical state and 161
the critical state friction angle was used as an input in the Mohr-Coloumb model. In order 162
to obtain the critical state friction angle of the granular sample, a shear test is performed 163
using 1078 DEM grains. A bi-periodic boundary condition was adopted on the sides of the 164
sample (figure 4.3a). Two layers of fixed grains (shown in black) were placed at the top and 165

Table 4.2 Micro-mechanical parameters used in DEM simulations of granular column collapse.

Parameter	Value
Young's modulus of glass bead	$70 \times 10^9 \text{ N/m}^2$
Poisson's ratio	0.22 - 0.24
Diameter of glass beads	0.92 to 1.38 mm
Normal and shear stiffness of grains	$1.6 \times 10^8 \text{ N/m}$
Normal and shear stiffness of wall	$4 \times 10^8 \text{ N/m}$
Inter-particle friction coefficient, μ	0.53
Wall friction coefficient	0.466
Coefficient of restitution, ε	0.75
Rolling spring constant	$1.0 \times 10^3 \text{ Nm/rad}$
Coefficient of rolling damping	$1.0 \times 10^{-1} \text{ Nms/rad}$

166 the bottom of the shear sample. A normal stress σ'_n and a horizontal velocity v was applied to
 167 the fixed grains at the top of the shear sample. As the normal effective stress was varied, the
 168 average shear stress in the sample was measured. The stresses were smoothed by averaging
 169 across time steps. The sample was sheared until the critical state was reached. The slope of
 170 shear stress versus normal effective stress gives the critical state friction angle. A critical
 171 state friction angle of 22.2° was obtained. The macroscopic friction angle was in the range
 172 observed by Estrada et al. (2008) and Mitchell and Soga (2005). The Young's modulus of
 173 the granular assembly was obtained as the initial slope of the stress-strain plot of a uni-axial
 174 compression of a laterally confined granular column using DEM.

175 Guilkey et al. (2003) suggests using at least four material points per cell for large
 176 deformation problems. In the present study there were 16 material points per cell. If the
 177 mesh is too fine and the number of particles is too large, the particle size $2l/p$ decreases, and
 178 the GIMP interpolation function tends to approach the original MPM function, as shown
 179 by Bardenhagen and Kober (2004). Hence, GIMP loses the merit that it reduces the numerical
 180 noise due to material points crossing the background mesh. In addition, the probability of
 181 particles crossing the background mesh increases with decrease in the mesh size, hence,
 182 more noise may be produced (Abe et al., 2013). The effect of the number of material points
 183 per cell on the run-out behaviour is discussed later in section 4.4.2.

184 The initial set-up of a granular column collapse ($a = 1$) using MPM is shown in figure 4.4.
 185 For all the MPM simulations, a cell size of $2 \times 10^{-3} \text{ m}$ with 16 material points per cell was
 186 adopted (figure 4.4a). The granular columns were discretised into 40,000 to 160,000 material
 187 points. Each material point represents one-eighth of a DEM soil grain. Since, the scale of
 188 the problem being modelled is small and it is important to precisely define the flow surface,
 189 a larger number of material points are used to represent the geometry. The initial vertical

4.2 Granular column collapse

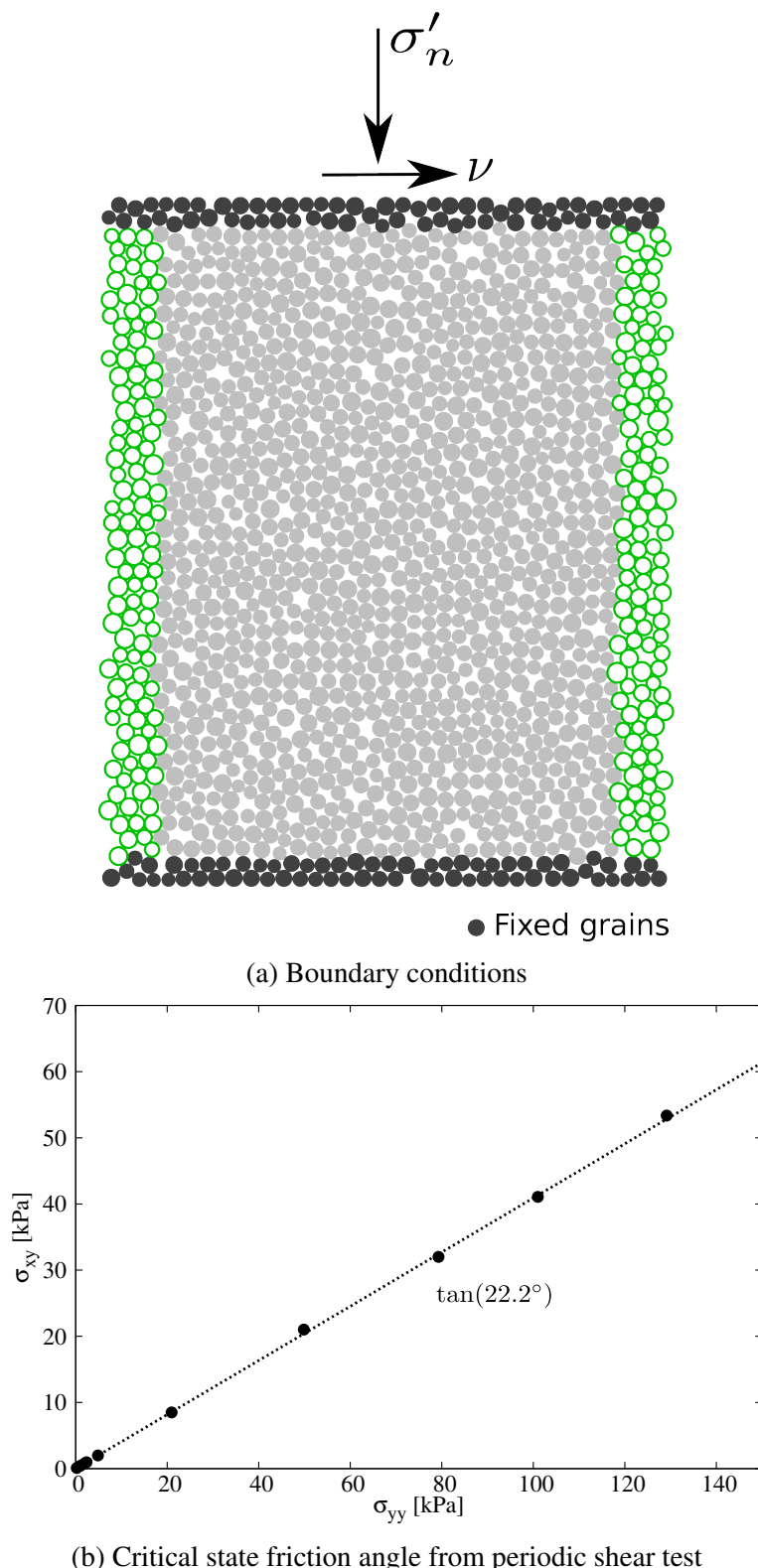


Figure 4.3 Periodic shear test using DEM to obtain macroscopic friction angle.

Table 4.3 Parameters used in continuum simulations of granular column collapse.

Parameter	Value
Material point spacing	0.5 mm
Number of material points per cell	16
Mesh length	2×10^{-3} m
Young's Modulus, E	1.98×10^6 N/m ²
Poisson's ratio, ν	0.22 to 0.24
Friction angle, ϕ	$22.2 \pm 0.2^\circ$
Dilatancy angle, Φ	0°
Density, ρ	1925 kg/m ³
Wall friction	0.466
Time step increment	1.0×10^{-6} s

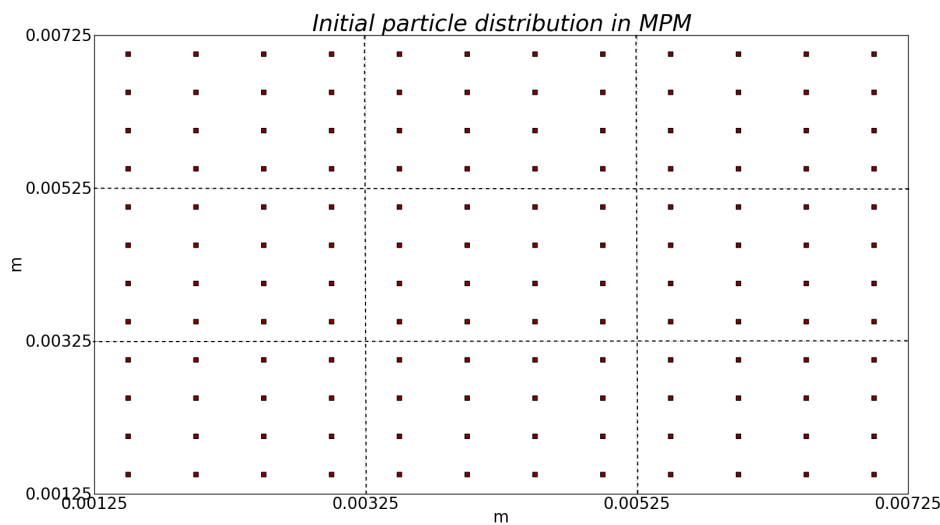
190 effective stress simulated in MPM, before the collapse stage, is shown in figure 4.4b. The
 191 extent of the background mesh in MPM is much larger than the initial column. In MPM, the
 192 material points move inside the grid, so it is important to have a sufficiently large domain
 193 for the collapse. Frictional boundaries are applied as constraints on the nodal accelerations
 194 on the left and the bottom boundaries. The parameters used for the continuum analyses are
 195 presented in table 4.3.

196 4.2.2 Deposit morphology

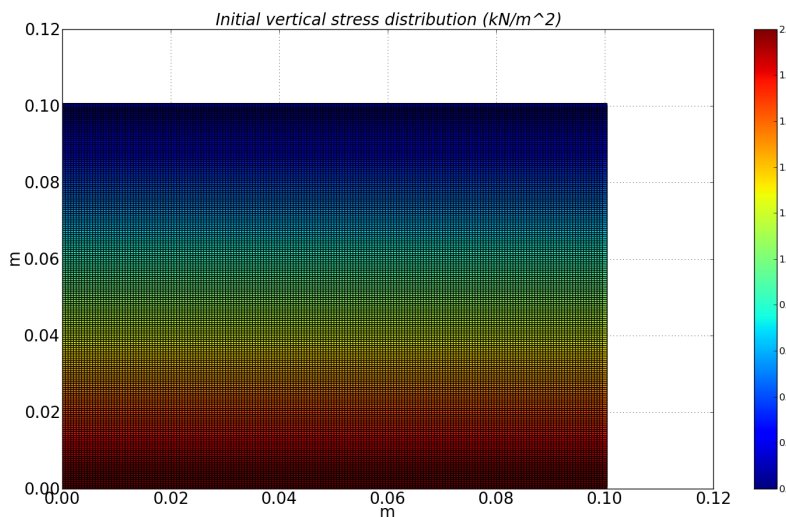
197 A series of two-dimensional plane-strain MPM and DEM simulations of granular column
 198 collapse were performed by varying the initial aspect ratio of the column from 0.2 to 10. The
 199 evolution of run-out and the flow kinematics observed in both approaches were compared
 200 to understand the ability and limitations of these approaches. The normalised final run-out
 201 distance, $\Delta L = (L_f - L_0)/L_0$, as a function of the initial aspect ratio a of the column is
 202 presented in figure 4.5. Similar to the experimental behaviour a power law relation between
 203 the run-out and the initial aspect ratio of the column is observed. Two distinct flow regimes
 204 can be seen: (a) for $a < 2.7$ a linear relation between the spread and aspect ratio can be
 205 observed, and (b) for $a > 2.7$ a power-law relationship exists. In the present study, the
 206 following scaling law for the run-out (using DEM) is observed:

$$207 \frac{L_f - L_0}{L_0} \approx \begin{cases} 1.67a, & a \lesssim 2.7 \\ 2.7a^{2/3}, & a \gtrsim 2.7 \end{cases} \quad (4.6)$$

4.2 Granular column collapse



(a) Initial arrangement of material points in the mesh. Closer view of 16 material points per cell for a column with an initial aspect ratio of 1. Cell size of 2×10^{-3} m.



(b) Initial vertical effective stress in MPM for a column with an aspect ratio of 1.

Figure 4.4 MPM initial mesh and vertical stress for a granular column collapse simulation ($a=1$).

Both, MPM and DEM simulations are able to capture the linear relationship for $a < 2.7$, and the simulation results agree with the experimental investigation (Lajeunesse et al., 2005). This shows that a simple frictional dissipation model is able to capture the flow dynamics for columns with small aspect ratios. For $a < 2.7$, the normalised run-out distances predicted using DEM simulations are very close to those observed in the experiment. DEM simulations with a hexagonal packing show shorter run-out distances in comparison to the randomly packed sample. This difference in the run-out behaviour might be due to crystallisation and jamming effects in hexagonal packing. The small difference in the final run-out between the DEM and the experimental results can be attributed to the variation in the packing of grains and the three-dimensional grain shape. Also, the experimental data corresponds to granular column collapse in a rectangular channel, where the collapse is not the pure two-dimensional collapse that is in the case of numerical simulations. Most aerial and sub-marine landslides have a large lateral extent, i.e., plane-strain condition, hence in the present study two-dimensional simulations are performed. Although two-dimensional simulations don't capture movement of the grains perpendicular to the plane of the experiment, it simplifies the configuration so as to compare DEM simulations with MPM. Also, Balmforth and Kerswell (2005) observed that the side-walls in quasi-two-dimensional collapse do not influence the power-law behaviour but affect the numerical constant, which depends on the material properties.

A significant difference in the final run-out between MPM, which is based on a simple frictional model for dissipation of potential energy, and DEM simulations, indicates a change in the mechanism of energy dissipation for columns with large aspect ratios ($a > 2.7$). A transition in the run-out behaviour at an aspect ratio of 2.7 indicates a change in the flow kinematics. Similar behaviour in the run-out distance was observed by Bandara (2013) for columns with large aspect ratios ($a \geq 2$). Mast et al. (2014) observed a 40% increase in the final run-out distances, for large aspect ratios, than reported in the literature. Previous studies have failed to describe the mechanism of energy dissipation in continuum approaches and the reason for longer run-out distance. Section 4.2.4 discusses the reason behind the difference in the run-out behaviour between continuum and experimental findings.

The longer run-out distance in MPM simulations at large aspect ratios might be influenced by the amount of material mobilised during the collapse. In tall columns, the entire column participates in the flow, in contrast to short columns where the collapse is due to avalanching of the flanks. It is possible that MPM simulations collapse more resulting in longer run-out distances. Figure 4.6 shows the normalised final height as a function of the initial aspect ratio of the column. Similar to the run-out behaviour, the normalised-height also shows two distinct regimes. The scaling of final height of the column with the initial aspect ratio of the

4.2 Granular column collapse

column can be written as

$$\frac{H_f}{L_i} \propto \begin{cases} a, & a \lesssim 0.7 \\ a^{2/3}, & a \gtrsim 0.7 \end{cases} \quad (4.7)$$

244

245

246

The final heights predicted by both DEM and MPM simulations match the experimental data for columns with smaller aspect ratios ($a \leq 0.7$). A linear relationship between the final height and the aspect ratio indicates that only a part of the granular column is mobilised during the collapse. For tall columns, both approaches predict similar normalised heights. However, the normalised height observed in MPM is higher than in DEM simulations, which is in contrast to the idea of an increase in the amount of material mobilised during the collapse in MPM simulations resulting in longer run-out distance. Hence, the longer run-out observed in MPM simulations is due a change in the flow dynamics at higher aspect ratios, which is not captured in MPM simulations. The final height of a column is controlled by the amount of static region in the granular column collapse, while the run-out distance is essentially a function of the flowing mass. Hence, it is important to compare the evolution of flow and the internal flow structure in DEM and MPM simulations.

247

248

249

250

251

252

253

254

255

256

257

258

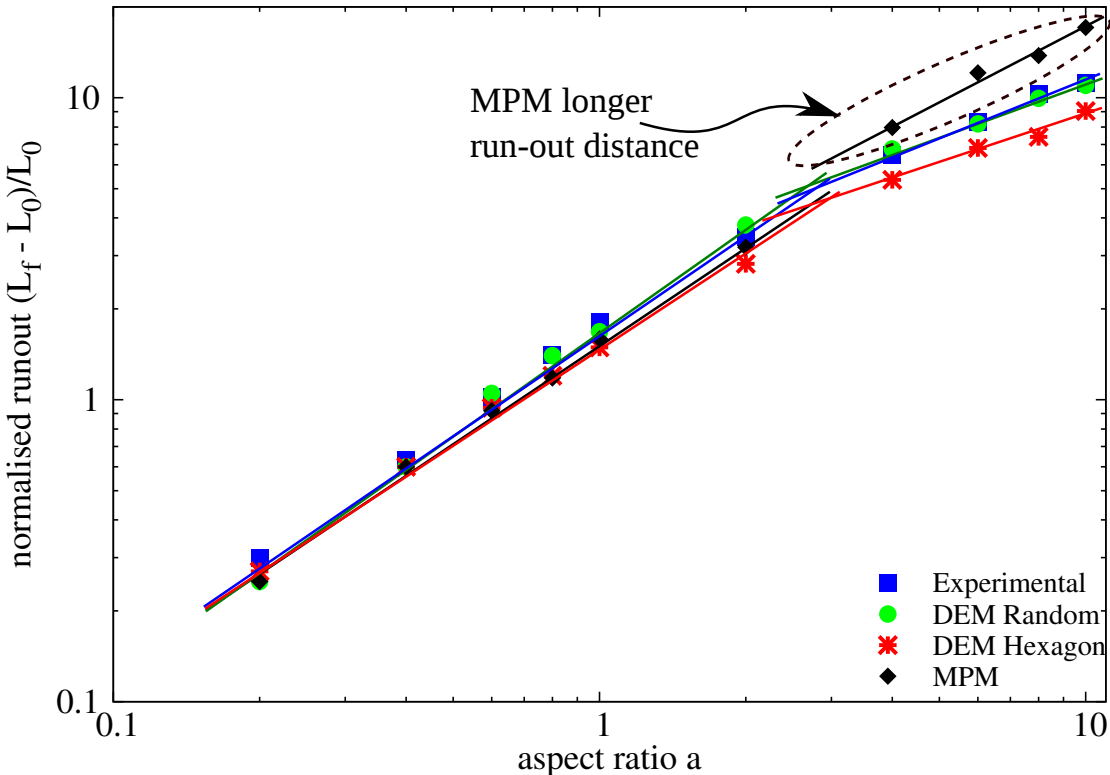


Figure 4.5 Normalised final run-out distance for columns with different initial aspect ratios.

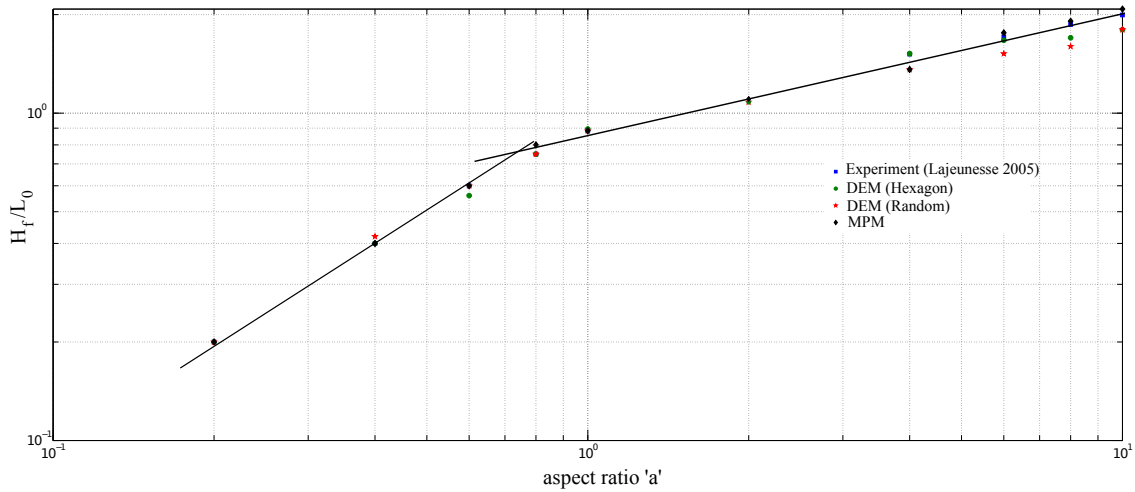


Figure 4.6 Normalised final collapse height for columns with different initial aspect ratios.

259 4.2.3 Flow evolution and internal flow structure

260 The normalised run-out and height as a function of the aspect ratio indicate that, for a
 261 given granular material and substrate properties, the flow dynamics and the final deposit
 262 morphology are independent of the volume of granular material released, but depend only
 263 on the geometry of the column. A power law relationship is observed between the run-out
 264 distance and the initial aspect ratio of the column. A transition in the run-out behaviour at an
 265 aspect ratio of 2.7 indicates a change in the flow dynamics.

266 Dimensional analysis of granular column collapse reveals an intrinsic time defined as
 267 $\sqrt{H_0/g}$. This intrinsic time is a transient time of order τ_c , at which the flow is fully developed,
 268 i.e., the potential energy available at the initial stage of collapse is now fully converted to
 269 kinetic energy. Numerical simulation of the velocity profile of a granular column ($a=0.4$) at
 270 the critical time τ_c is presented in figure 4.7. At the critical time, the velocity field depends
 271 only on the position of the grain along the sliding mass. The maximum velocity is observed at
 272 the front of the flowing mass corresponding to that of a plug flow in the horizontal direction.
 273 Particulate and continuum simulations show similar run-out distances at the critical time.
 274 Both approaches show similar quantities of material destabilised above the failure surface.
 275 However, the crystalline arrangement of soil grains in a hexagonal packing results in a
 276 different flow mechanics, which also shows the effect of jamming at the flow front. The
 277 continuum nature of MPM results in a slightly different geometry of the material destabilised
 278 above the failure surface in comparison to DEM simulations. The velocity profile is similar
 279 to a steady granular surface flow observed by Lajeunesse et al. (2004).

For short columns ($a < 2.7$), the flow is initiated by a failure at the edge of the pile along a well-defined shear-failure surface. The granular mass fails through avalanching of flanks producing a truncated cone-like deposit (' $a' < 0.7$) or conical deposit (' $a' > 0.7'). The grains located above the failure surface move "*en masse*" leaving a static region underneath the failure surface. For columns with lower initial aspect ratios, the run-out distance is proportional to the mass flowing above the failure surface. The spreading results from a Coulomb-like failure of the edges and implies no free fall of the column. In this case, the effective friction properties of the flow can be simply predicted from the shape of the final deposit. The amount of mass mobilised during the collapse is significantly affected by the angle of the failure surface.$

Figure 4.7 shows that both numerical techniques predict a distinct failure surface when the flow is fully developed at critical time τ_c . The angle of the failure surface is found to be about 55° . The failure surface begins from the toe of the column and propagates inwards at an angle of 50 to 55° . The formation of the "truncated conical deposit" or "conical deposit" depends on the initial length of the column, as the angle of the failure surface is found to be independent of the aspect ratio. The failure angle is consistent with the interpretation in terms of *active Coulomb failure*, which leads to a predicted failure angle $\phi_y = 45^\circ + \phi/2$, where ϕ is the friction angle of the granular material. In the present study, the macroscopic friction angle is 22° , which leads to $\phi_y = 45^\circ + 22^\circ/2 = 56^\circ$, which is in good agreement with the numerical simulations and the experimental observations by Lajeunesse et al. (2004). The shear-failure angle has a direct effect on the transition between the truncated cone and the conical deposit occurring at an aspect ratio of 0.7 .

The final profile of the granular column with an initial aspect ratio of 0.4 obtained from DEM and MPM simulations are shown in figure 4.8. Both MPM and DEM show similar run-out behaviour. The continuum approach is able to capture the flow dynamics of short columns, where the failure mechanism is active Coulomb failure. In dense hexagonal packing, the failure surface is steep due to crystallisation effects. The variation in the angle of the failure surface causes a difference in the amount of material destabilised, and in turn the run-out distance. This crystallisation phenomenon is found to have a significant influence on the final deposit of the granular column.

MPM and DEM simulations of the velocity profile of a granular column with an initial aspect ratio of 6 at critical time τ_c is shown in figure 4.9. For tall columns ($a > 2.7$), the flow is still initiated by a well defined failure surface as can be seen in figure 4.9. However, in this case the initial granular column is much higher than the top of the failure surface. Due to gravity most of the grains in the column experience free-fall consuming the column along their way. When they reach the vicinity of the failure surface, the flow gets deviated along

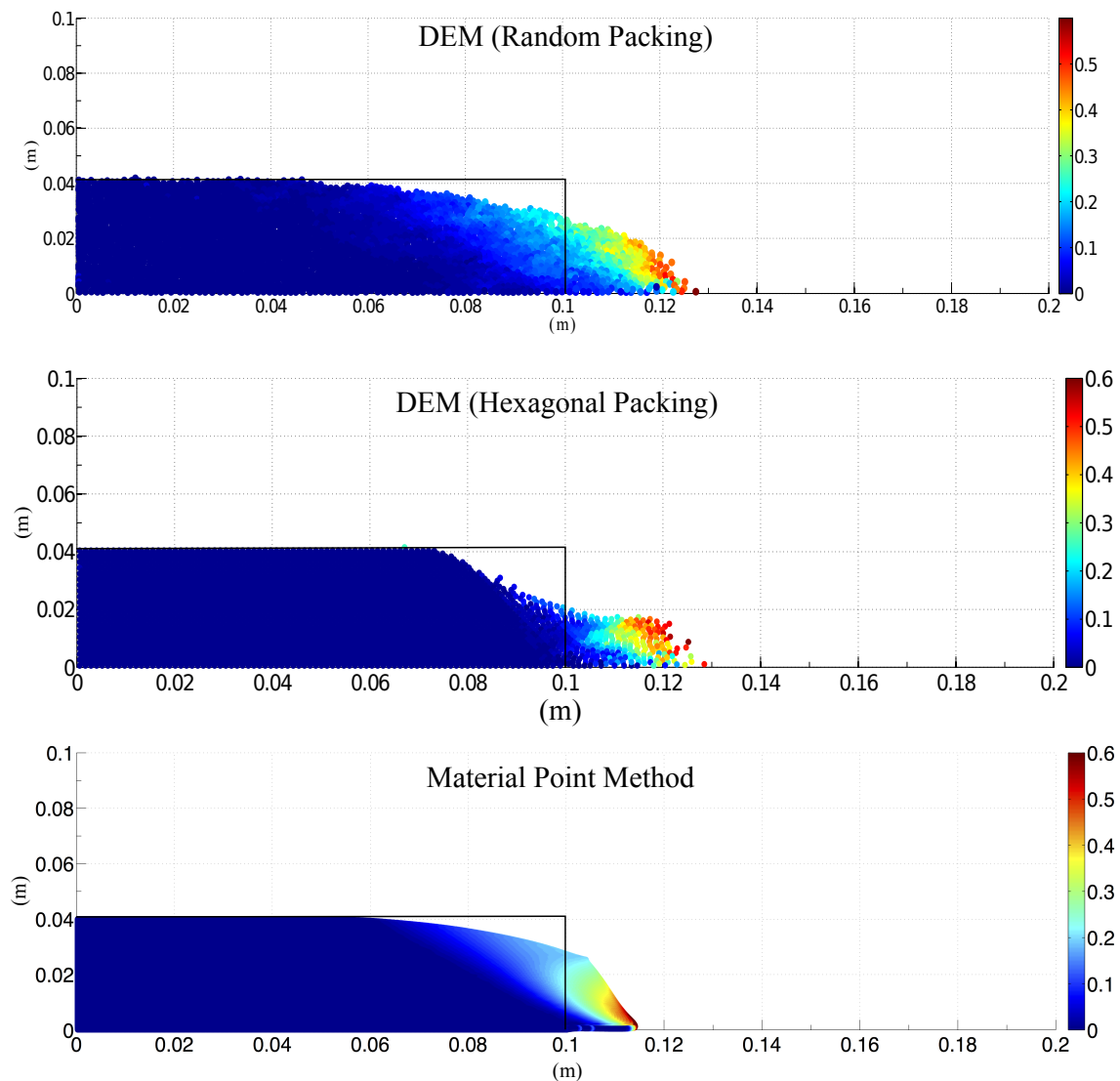


Figure 4.7 Velocity profile of a granular column collapse ($a = 0.4$, $t = \tau_c$). Velocity is shown in m/s.

4.2 Granular column collapse

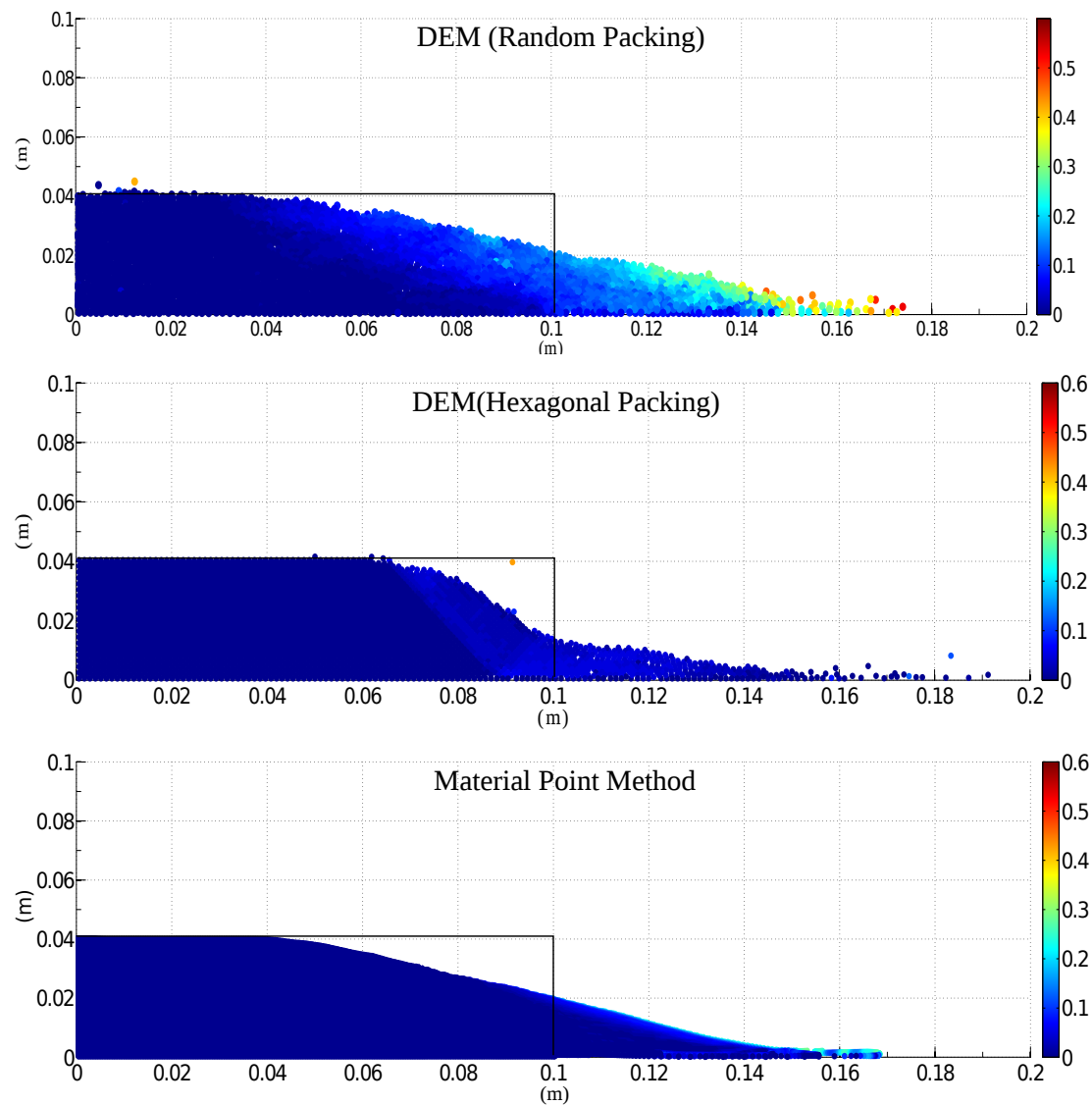


Figure 4.8 Velocity profile of a granular column collapse ($a = 0.4$, $t = 3 \times \tau_c$). Velocity is shown in m/s.

316 the horizontal direction releasing a huge amount of kinetic energy gained during the free fall.
 317 For larger aspect ratios ($a > 0.7$), the resulting static region is a cone, the final height of the
 318 cone H_f lies above the summit of the failure surface.

319 An initial failure surface starting from the toe end of the column at an angle of about 55°
 320 can be observed at the critical time τ_c . As the collapse of the granular column progresses,
 321 successive failure planes parallel to the initial failure surface are formed and shear failure
 322 occurs along these planes. The presence of several shear bands in the final profile of
 323 the collapsed granular column confirms this behaviour. This observation throws light on
 324 the mechanics of propagation of shear bands in massive landslides such as the Storegga
 325 submarine landslide, where the propagation of shear bands is found to have caused long
 326 run-out distances (Dey et al., 2012). After the initial stage of collapse in tall columns, the
 327 flow behaviour becomes similar to that of columns with lower initial aspect ratios as the flow
 328 starts descending along the failure plane. Hexagonal packing results in crystallisation, which
 329 has a significant effect on the run-out distance by forming a series of parallel shear bands,
 330 resulting in an unnatural flow kinematics. The final profile of the collapsed granular column
 331 with an initial aspect ratio of 6 is presented in figure 4.10. For tall columns, the dissipation
 332 process is more complex due to the free-fall dynamics. The vertical acceleration of the grains
 333 induces a non-trivial mass distribution in the flow during spreading. Staron and Hinch (2007)
 334 observed that the mass distribution plays a dominant role in the power-law scaling observed
 335 in the run-out.

336 Regardless of the experimental configuration and the initial aspect ratio of the columns,
 337 the flow is initiated by a well-defined rupture surface, above which the material slides down
 338 leaving a static region underneath the failure plane. Depending on the aspect ratio of the
 339 column, two asymptotic behaviours are observed. For smaller aspect ratios, the flow is
 340 dominated by friction where as the large aspect ratio columns are influenced by the pressure
 341 gradient.

342 To study the influence of aspect ratio on the flow dynamics of granular columns, the
 343 flow front $L(t)$ and the maximum height of column $H(t)$ are tracked. The evolution of scaled
 344 height (H_f/L_0) and the run-out distance $(L_f - L_0)/L_0$ with time for granular columns with
 345 initial aspect ratios of 0.4 and 6 are presented in figure 4.11. Three distinct regions can be
 346 observed in the flow evolution of a granular column collapse regardless of the initial aspect
 347 ratio of the column. An initial transient acceleration phase is observed for a time $0.8\tau_c$. The
 348 critical time, τ_c is evaluated as the time at which the potential energy available for the flow
 349 has been converted to kinetic energy. This phase is followed by a heap movement of granular
 350 material at the foot of the column with a constant spreading velocity V for about $2\tau_c$. When
 351 time is longer than the critical time ($t > \tau_c$), the velocity varies linearly with depth in the

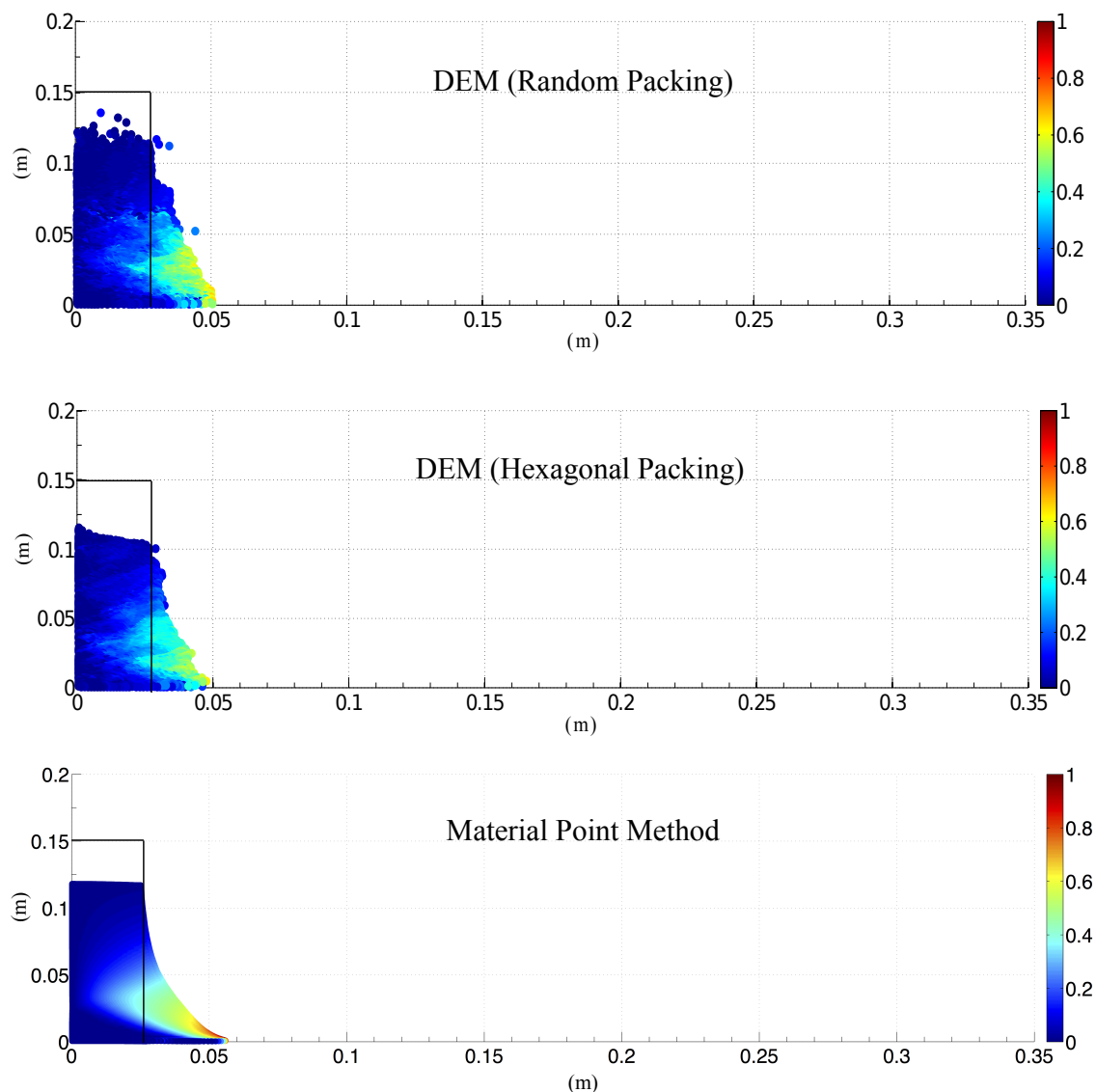


Figure 4.9 Velocity profile of a granular column collapse ($a = 6, t = \tau_c$). Velocity is shown in m/s.

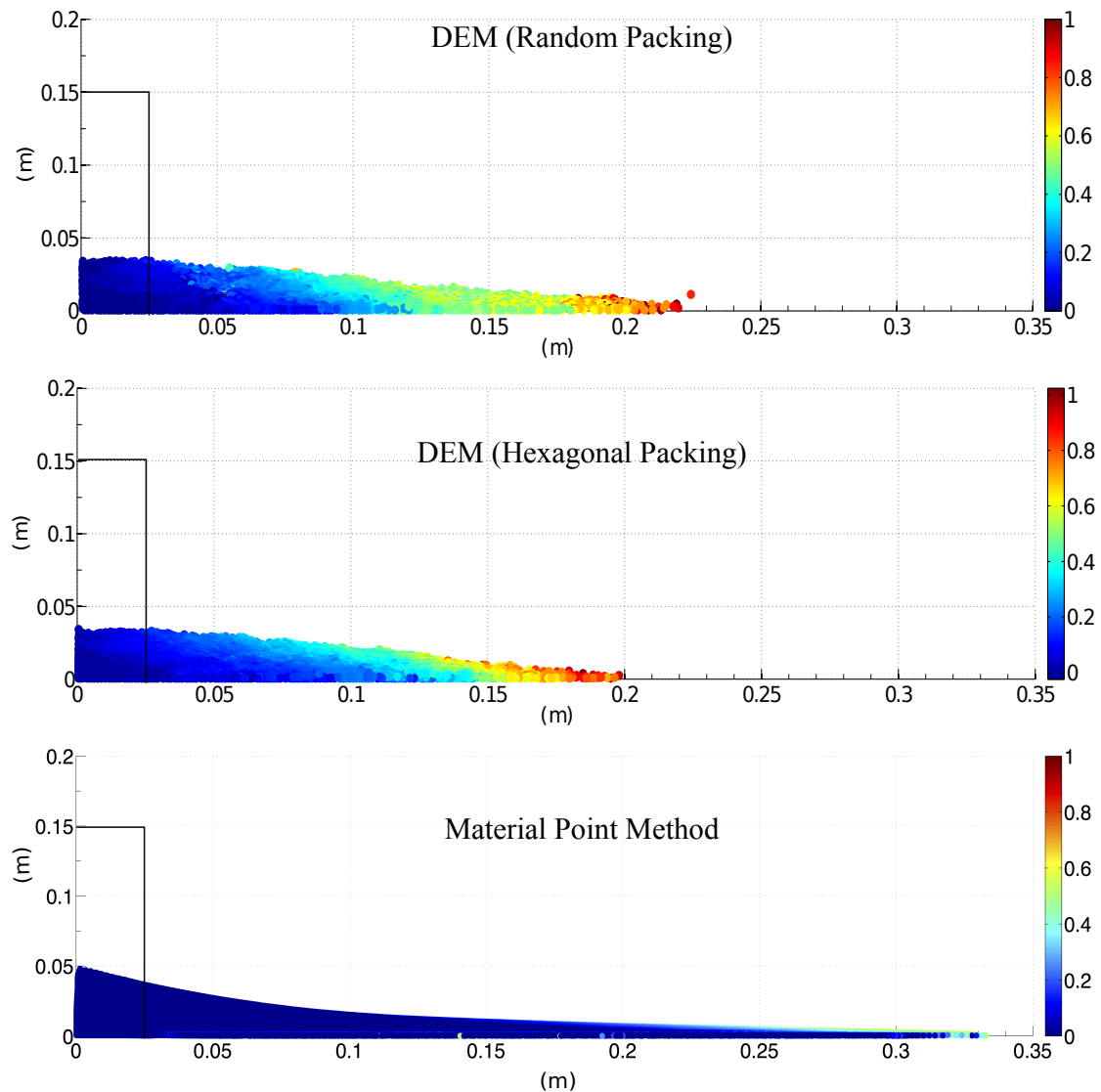


Figure 4.10 Velocity profile of a granular column collapse ($a = 6$, $t = 3 \times \tau_c$). Velocity is shown in m/s.

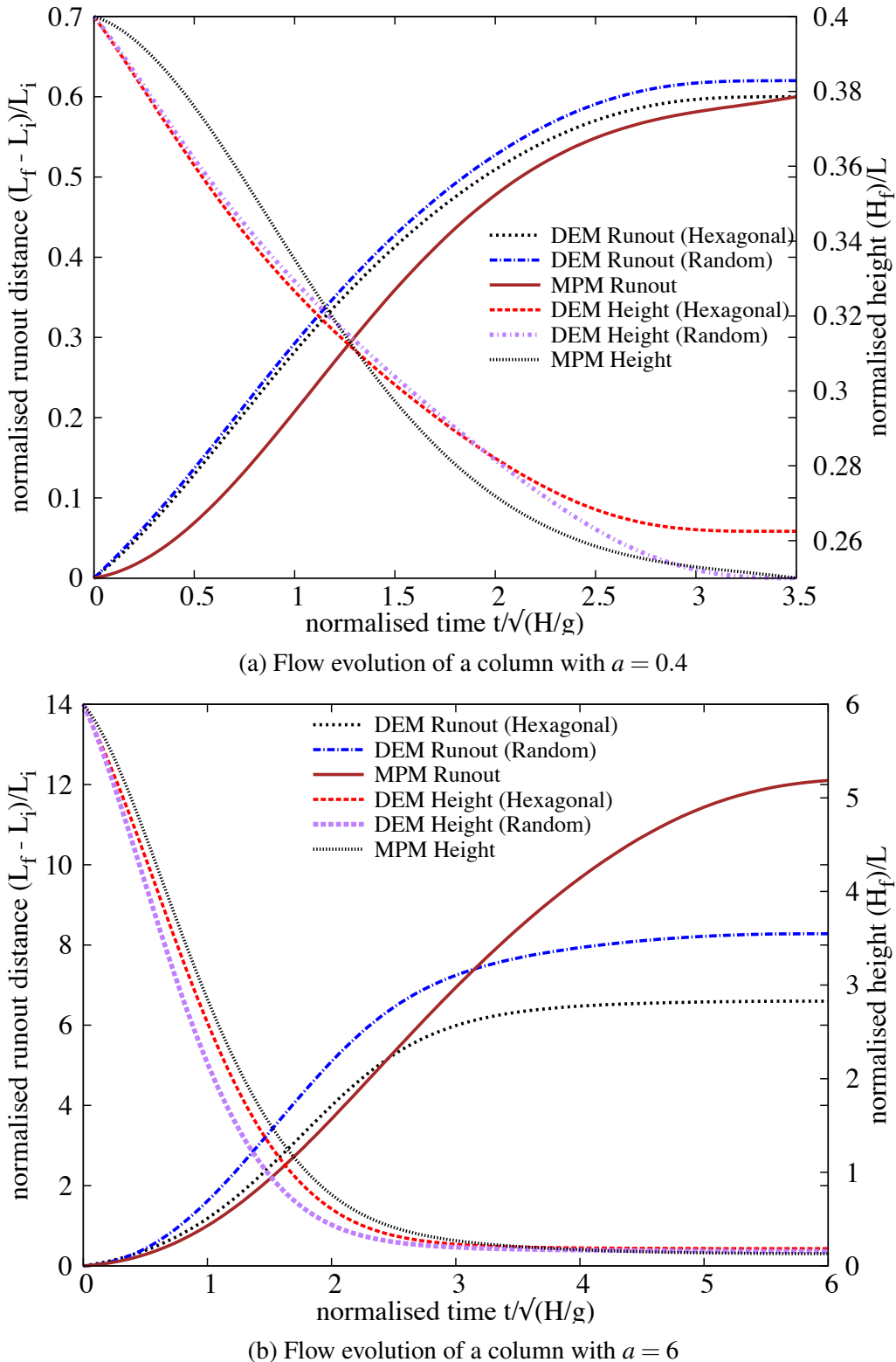
flowing layer and decreases exponentially with depth near the static layer. This velocity profile is similar to those observed in steady granular surface flows (Lajeunesse et al., 2004). Most of the run-out happens during this phase. The final phase involves deceleration of the flow front and the flow comes to rest after about $0.6\tau_c$. The spreading of the granular column ceases after a time on the order of about $3\tau_c$, however some motion still persists along the free surface behind the flow front for a much longer time due to internal rearrangement, the duration of which can last up to $t \approx 6\tau_c$.

In short columns, the critical time observed in both hexagonal and random packing of grains matches the experimental observations. However, the material point method takes longer for the flow to be fully mobilised; this can be attributed to the continuum nature of MPM which takes $\sim 20\%$ longer to destabilise the initial stress conditions. However, the actual run-out duration of the flow is similar to DEM and the granular mass comes to rest at about $t = 3\tau_c$, this is due to a steeper decline in the potential energy in MPM compared to DEM simulations.

For columns with larger aspect ratios, the continuum and particulate approaches simulate similar flow evolution up to $3\tau_c$, beyond which particulate simulation decelerates and comes to rest, while the flow continues to evolve in MPM simulation resulting in longer run-out distance. The flow comes to rest at time $t = 6\tau_c$. The three phases in a granular flow can be distinctly observed in the flow evolution plot for a column with an initial aspect ratio of 6 (figure 4.11b). The flow evolution behaviour observed in the case of DEM simulation matches the experimental observation by Lajeunesse et al. (2004). Hexagonal packing predicts longer time for the flow to evolve, which can be attributed to jamming of grains. In MPM simulations, the failure starts at the toe of the column and slowly propagates up to form the failure surface. This results in slower initiation of the flow. In DEM, however, the initial stage of collapse is characterised by free-fall under gravity. It can be observed that MPM overestimates the critical time by 50%. Although MPM and DEM simulations show the same run-out at time $t = 3\tau_c$, the flow evolution between both the approaches is different. The MPM simulations show that the granular flow continues to accelerate beyond $3\tau_c$ and ceases at around $6\tau_c$. In order to understand the difference in the flow dynamics in the case of material point method, it is important to study the mechanism of energy dissipation.

4.2.4 Energy dissipation mechanism

The energy dissipation mechanism during collapse provides useful insights into the flow dynamics. In the case of small aspect ratios, the columns undergo no free fall. The spreading mainly results from the failure of the edges, while the top of the column remains essentially undisturbed in the central area. The amount of energy dissipated during the spreading δE

Figure 4.11 Flow evolution of granular column collapse ($a = 0.4$ and 6).

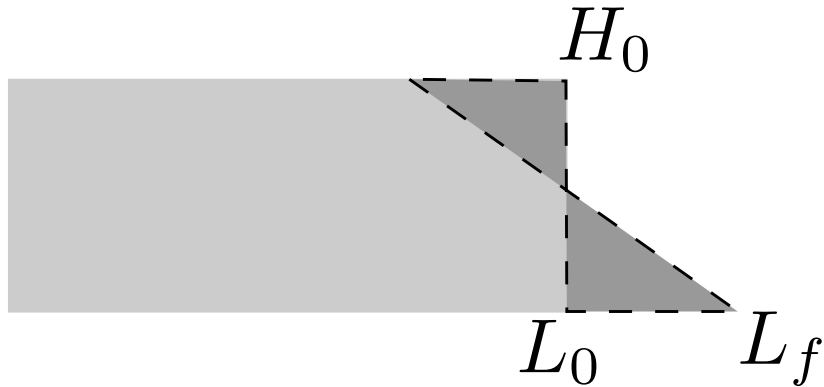


Figure 4.12 Scheme of collapse for small aspect ratio columns. The amount of energy δE lost in the process can be evaluated from the run-out distance $L_f - L_0$ (Staron and Hinch, 2007).

can be easily recovered using the simple shape of the final deposit and volume conservation 387
(figure 4.12). The difference in potential energy between the initial and the final states gives 388

$$\delta E = \frac{1}{6}g\rho(L_f - L_0)H_0^2, \quad (4.8) \quad 389$$

where ρ is the density of the packing. It is assumed that this energy is dissipated by the 390 work of frictional forces W_μ over the total run-out distance by the center of mass G of the 391 spreading material. The collapse involves two regions of dissipation: the amount of mass 392 destabilised $\frac{1}{4}(L_f - L_0)H_0$ over two thirds of the run-out distance $2(L_f - L_0)/3$ (considering 393 the triangular shape of the final deposit and the initial and the final positions of the centre 394 of mass). The effective coefficient of friction μ_e characterises the mean dissipation in the flow. 395 The work of friction forces is 396

$$W_\mu = \frac{1}{6}\mu_e g\rho(L_f - L_0)^2 H_0. \quad (4.9) \quad 397$$

Equating δE and W_μ gives $\mu_e(L_f - L_0) = H_0$. The scaling of the runout leads directly to 398 the relation $\mu_e = \lambda^{-1}$, where λ is the numerical constant in the power-law relation between 399 the run-out and the initial aspect ratio, which depends on the material properties. The amount 400 of energy δE dissipated during the spreading is compared with $W = N_p g m_p r_p$, where N_p is 401 the total number of grains, m_p is their mass, and r_p is the total horizontal distance run by each 402 of them. The dissipation energy δE is proportional to W . Staron and Hinch (2007) observed 403 that the coefficient of proportionality gives a measure of the effective friction and observed 404 a power law dependence between μ_e and internal friction angle μ : $\mu_e = 0.425\mu^{0.2}$. In this 405 study, an effective friction angle μ_e of 21° is observed, which is very close to the critical state 406 friction angle of 22° used in MPM simulations. The global effective friction angle obtained 407 from the simple macroscopic energy-dissipation analysis matches the critical state friction 408

409 used in MPM simulations. This proves that the energy dissipation mechanism modelled in a
 410 continuum sense as a frictional dissipation process captures the flow kinematics observed in
 411 DEM and experiments for short columns.

412 Figure 4.13a shows the time evolution of the normalised potential energy (E_p/E_0) and
 413 kinetic energy (E_k/E_0) for granular columns with an initial aspect ratio $a = 0.4$. The
 414 normalised potential and kinetic energy are computed as

$$415 \quad E_p = \sum_{p=1}^{N_p} m_p g h_p, \quad (4.10)$$

$$416 \quad E_{ki} = \frac{1}{2} \sum_{p=1}^{N_p} m_p v_p^2, \quad (4.11)$$

418 where N_p is the total number of grains, m_p is the mass of a grain p , h_p is the height and v_p is
 419 the velocity of the grain p . The cumulative dissipation energy is computed as

$$420 \quad \frac{E_d}{E_0} = 1 - \frac{E_k}{E_0} - \frac{E_p}{E_0}. \quad (4.12)$$

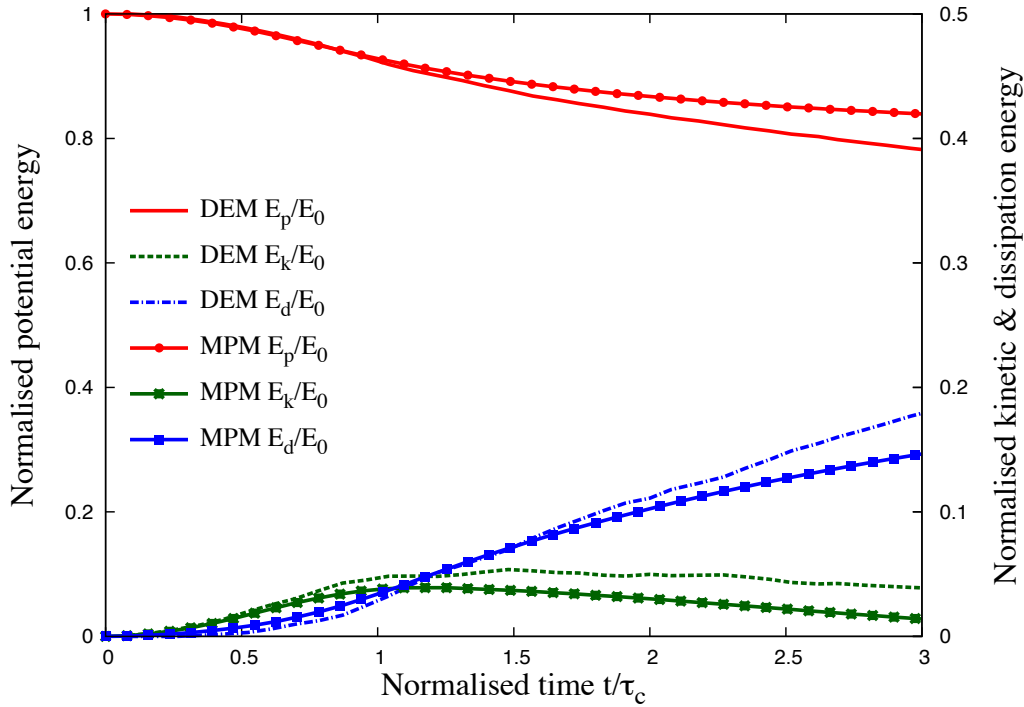
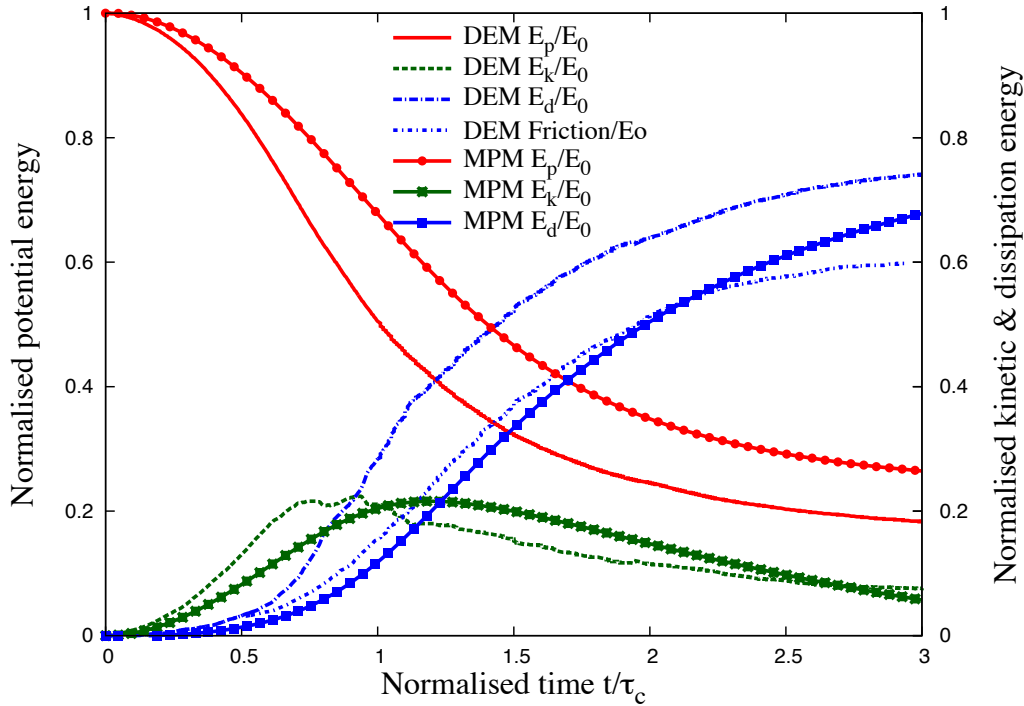
422 It can be observed that both MPM and DEM show similar energy dissipation mechanisms.
 423 The DEM simulation shows 3% more potential energy dissipation in comparison with MPM
 424 simulations. This small difference in the potential energy is due to grain rearrangements.
 425 This shows the ability of the continuum approach to capture the flow kinematics of columns
 426 with small aspect ratios ($a \leq 2.7$).

427 The evolution of normalised kinetic and potential energy of a tall column collapse ($a = 6$)
 428 are shown in figure 4.13b. It can be observed that the initial potential energy stored in the
 429 grains is converted to kinetic energy which is dissipated as the granular material flows down.
 430 Three successive stages can be identified in the granular column collapse. In the first stage,
 431 similar to short columns, the flow is initiated by a well defined failure surface. However, the
 432 centre of gravity of the granular column is much higher than the top of the failure surface,
 433 which results in free fall of grains under gravity consuming the column along their way.
 434 In this stage which lasts for ($t < 0.8\tau_c$), the initial potential energy stored in the grains is
 435 converted into vertical motion. In the second stage, when the grains reach the vicinity of the
 436 failure surface, they undergo collisions with the bottom plane and the neighbouring grains,
 437 thus causing the flow to deviate along the horizontal direction releasing a large amount of
 438 kinetic energy gained during the free fall (figure 4.10). In the third stage, the grains eventually
 439 leave the base area of the column and flow sideways (Lajeunesse et al., 2004). As the process

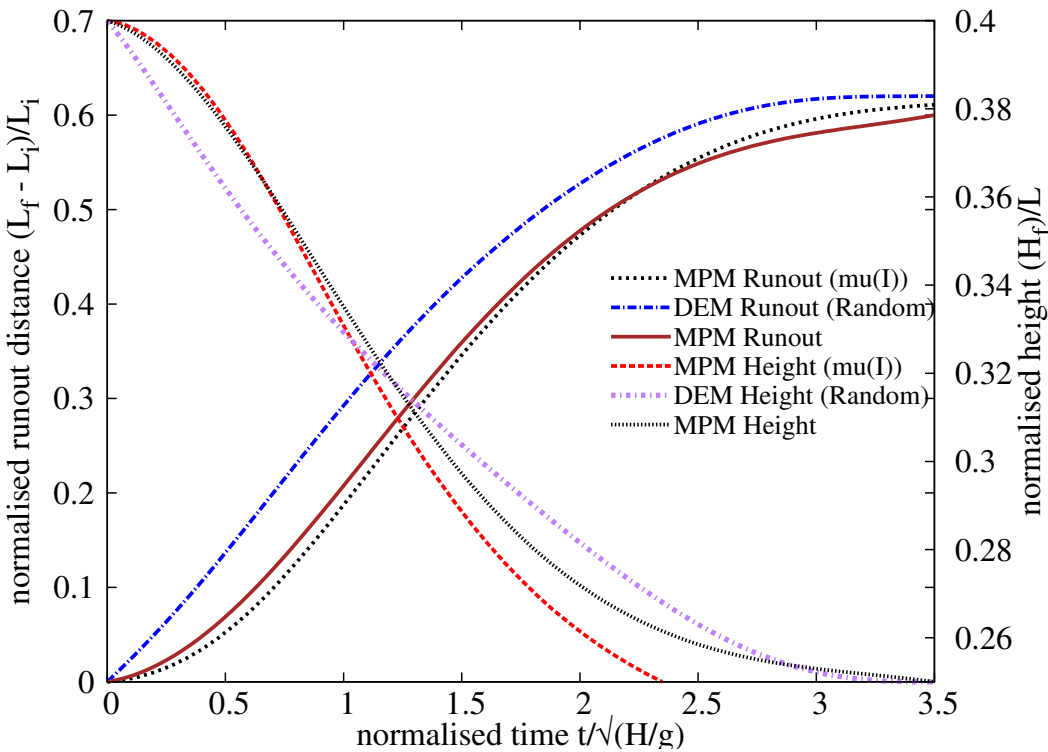
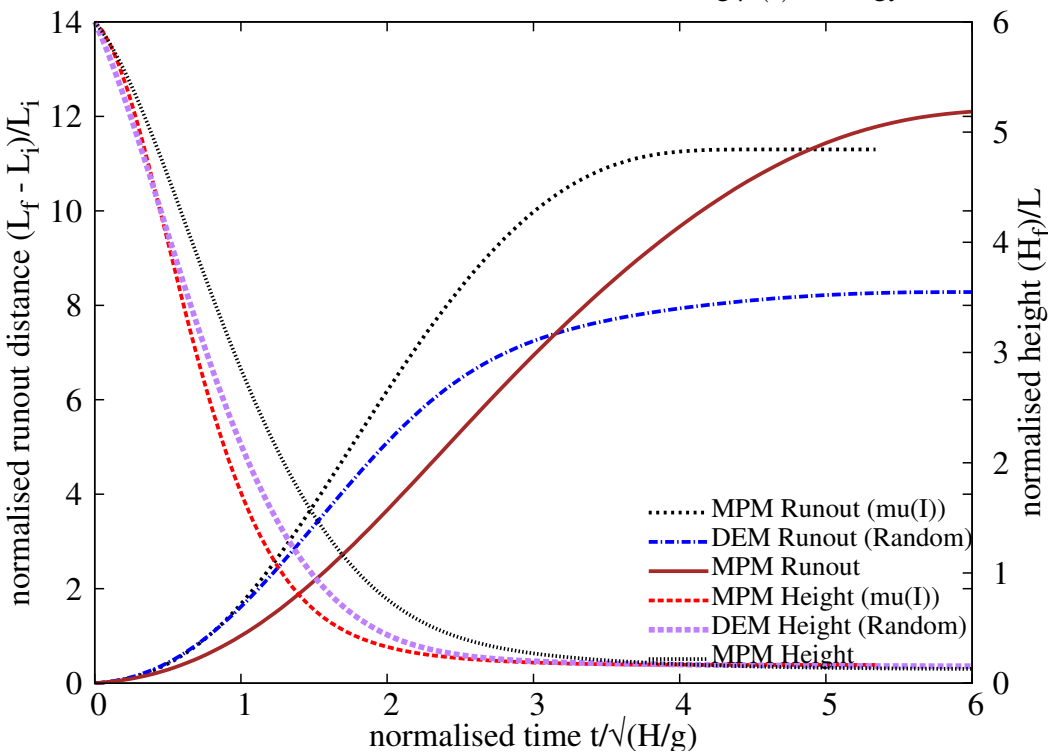
involves collective dynamics of all the grains, it is difficult to predict the exact trajectory of a grain, however, the overall dynamics can be explained. 440
441

DEM simulations model both collisional and frictional dissipation processes during the collapse of tall columns. However, MPM simulations assume that the total initial potential energy stored in the system is completely dissipated through friction over the entire run-out distance, which results in longer run-out distance. Figure 4.13b shows the evolution of normalised energies with time for MPM and DEM simulations. At the initial stage of collapse, characterised by free fall of grains under gravity, the DEM simulation, due to its particulate nature shows a rapid reduction in the potential energy in comparison with the MPM simulations, where the failure begins from the toe of the column. The continuum nature of the MPM simulations results in slower initiation of the collapse (figure 4.11b). It can be also observed from figure 4.13b that the dissipation of energy in MPM is 25% less than in the DEM simulations. In order to understand the mechanism of energy dissipation, it is important to separate the contribution from the cumulative frictional and collisional parts. The frictional dissipation (basal and internal friction) observed in DEM is almost identical to the frictional dissipation observed in MPM (figure 4.13b). The difference in the dissipation energy is due to the collisional regime, which occurs at $0.8\tau_c$. The total dissipation and the frictional dissipation curves diverge around $0.8\tau_c$ where the grains near the vicinity of the failure surface undergo collisions with the bottom plane and the neighbouring grains resulting in collisional dissipation of the stored potential energy. DEM simulation show drop in the peak kinetic energy at $\approx 0.8\tau_c$, which is at the beginning collisional dissipation stage. MPM lacks this collision dissipation mechanism, which results in longer run-out distances for columns with large aspect ratios. 462

The $\mu(I)$ rheology, discussed in ??, describes the granular behaviour using a dimensionless number, called the *inertial number I*, which is the ratio of inertia to the pressure forces. Small values of I correspond to the critical state in soil mechanics and large values of I corresponds to the fully collisional regime of kinetic theory. $\mu(I)$ rheology is adopted in MPM simulations to understand the characteristics of the flow regime. The Mohr-Coulomb model was used along with $\mu(I)$ rheology. The friction angle is changed according to a friction law (Da Cruz et al., 2005) that is dependent on the inertial number I as $\mu = \mu_{min} + bI$, where $\mu_{min} = 0.22$ and $b = 1$. Figure 4.14 shows the flow evolution of granular column collapse for aspect ratios a of 0.4 and 6 using $\mu(I)$ rheology. For short columns, the evolution of flow based on $\mu(I)$ rheology is identical to the MPM simulation using Mohr-Coloumb model. However, for tall columns, $\mu(I)$ rheology evolves at the same rate as the DEM simulations up to $t = 0.8\tau_c$, after which the MPM simulation continues to accelerate due to lack of collisional dissipation, while the DEM simulation decelerates with time. 475

(a) Energy evolution of a column with $a = 0.4$.(b) Energy evolution of a column with $a = 6$.Figure 4.13 Energy evolution of granular column collapse ($a=0.4$ and 6).

4.2 Granular column collapse

(a) Flow evolution of a column with $a = 0.4$ using $\mu(I)$ rheology.(b) Flow evolution of a column with $a = 6$ using $\mu(I)$ rheology.Figure 4.14 Flow evolution of granular column collapse using $\mu(I)$ rheology ($a=0.4$ and 6).

476 Figure 4.15 shows that the short column attains a maximum inertial number of 0.012,
477 which is in the dense granular flow regime, inertial number $\approx 10^{-3} < I < 0.1$ (Da Cruz
478 et al., 2005). However for the tall column, the maximum inertial number $I \approx 0.04$ is still
479 within the dense granular flow regime. DEM simulations, however, showed a collisional
480 regime that has inertial numbers higher than 0.1. This shows that continuum approach using
481 frictional laws are able to capture the flow kinematics at small aspect ratios, however they
482 are unable to precisely describe the flow dynamics of tall columns, which is characterised
483 by an initial collisional regime. This suggests that triggering mechanisms play a crucial
484 role in the case of modelling the natural flows. This stresses the necessity of accounting for
485 initiation mechanisms while modelling the run-out behaviour using continuum approaches to
486 predict realistic granular flow behaviour. The role of the initiation mechanism on the run-out
487 behaviour and the ability of MPM in modelling transient flows that does not involve collision
488 are investigated in section 4.4. The initial material property has a significant influence
489 on the run-out behaviour. This aspect has attracted less research. In the next section, 2D
490 DEM simulations are performed to understand the influence of initial grain properties on
491 the collapse. This gives us a better understanding of the input parameters required in the
492 continuum modelling.

493 **4.3 Role of initial grain properties on the collapse of gran-
494 ular columns**

495 The role of material properties and the distribution of mass in the system have been shown to
496 have a non-trivial influence on the flow kinematics and the internal flow structure. Hence
497 it is important to understand the role of initial packing density on the run-out behaviour in
498 the case of granular column collapse. Lube et al. (2005) observed that the run-out distance
499 scales with the initial aspect ratio of the column, independent of the material properties.
500 The run-out evolution after the initial transition regime is a frictional dissipation process,
501 and the lack of influence of material properties on the run-out behaviour is inconsistent
502 with frictional dissipation in continuum modelling of granular flow behaviour. Balmforth
503 and Kerswell (2005) observed that the material properties have almost no influence on the
504 exponent of the normalised run-out as a function of the initial aspect ratio. The numerical
505 constant of proportionality, however, showed clear material dependence. This corroborates
506 the conclusions of Lajeunesse et al. (2004) and refutes that of Lube et al. (2005). Daerr and
507 Douady (1999) also observed strong influence of initial packing density and the internal
508 structure on the behaviour of granular flows.

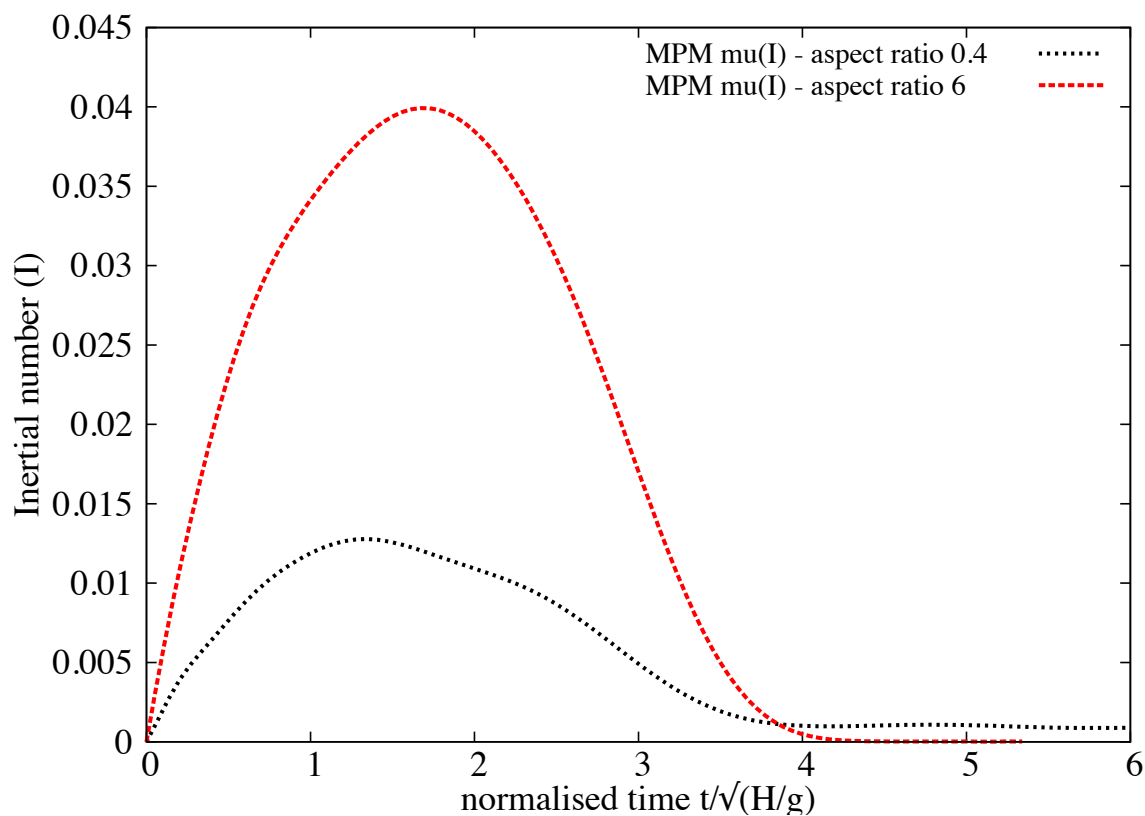


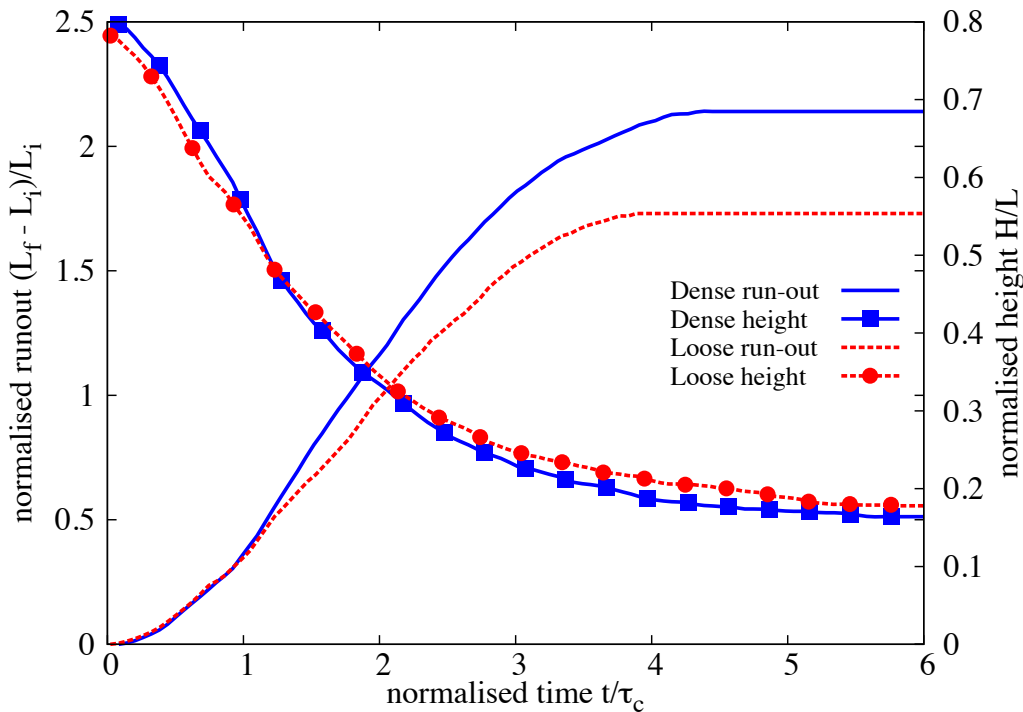
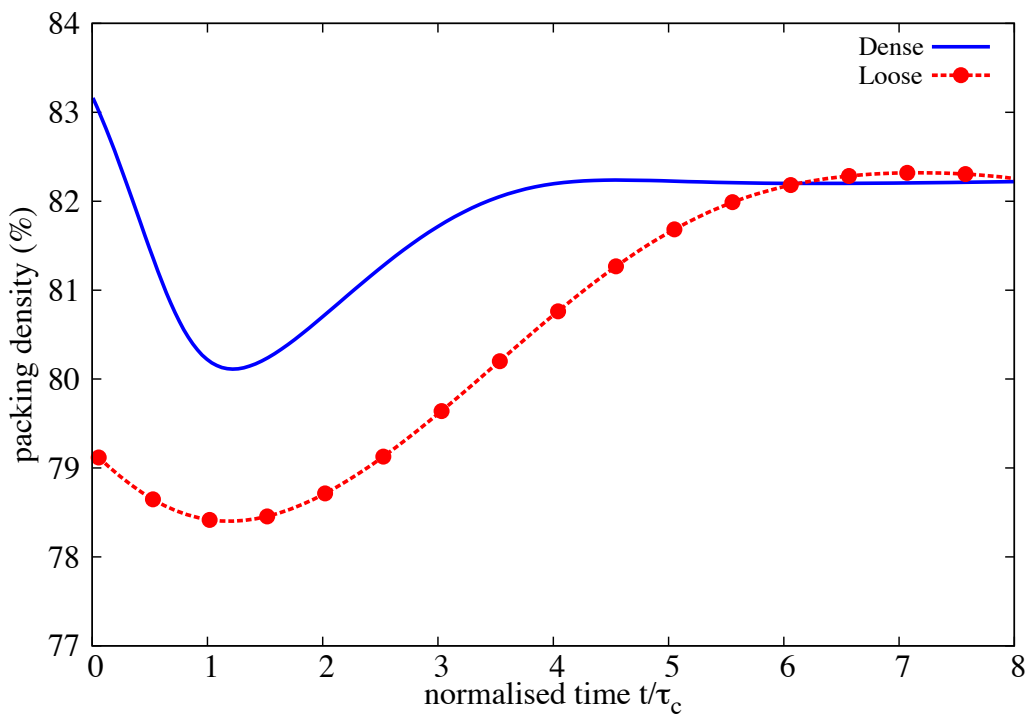
Figure 4.15 MPM simulation of evolution of inertial number with time for columns with $a = 0.4$ and $a = 6$.

509 It should be noted that the collapse experiment is highly transient and no clear stationary
510 regime is observed. On the contrary, the acceleration and the deceleration phases cover nearly
511 the whole duration of the spreading. This makes it difficult to analyse the flow structure
512 and its relation with other characteristic of the system. The knowledge of the final run-out
513 is not a sufficient characterization of the deposit; one also needs to know how the mass is
514 distributed during the flow to understand the dynamics and the dissipation process. This
515 is expected to be true in natural contexts as well as in experiments. While the inter-grain
516 friction does not affect the early vertical dynamics, nor the power-law dependence, it controls
517 the effective frictional properties of the flow, and its internal structure (Staron and Hinch,
518 2007). It is interesting to note that the details of the structure of the flow do not influence the
519 final run-out dependence, and thus seem to play a marginal role in the overall behaviour of
520 the spreading. This could explain why a simple continuum model with a frictional dissipation
521 could reproduce the run-out scaling for columns with small aspect ratios.

522 Most research has been focussed on the run-out behaviour of mono-disperse grain sizes.
523 However, the influence of initial packing density and poly-dispersity have attracted less
524 interest. In the present study, DEM simulations of collapse of loose (79% packing density)
525 and dense (83% packing density) granular columns with an initial aspect ratio a of 0.8 are
526 performed to understand the influence of material properties on the run-out behaviour. The
527 evolution of normalised run-out with time for two different initial packing densities are
528 presented in figure 4.16. At the initial stage of collapse $t = \tau_c$, the flow evolution is identical
529 in both dense and loose conditions. However, the dense column flows for 30% longer than
530 the loose columns. Both the columns come to rest at around $t = 4\tau_c$. The columns, however,
531 show similar evolution of the normalised height. This shows that only a part of the column is
532 destabilised during the collapse.

533 Figure 4.18 shows the evolution of potential and kinetic energy with time. Similar
534 potential energy evolution in both dense and loose conditions reveals that there is no change
535 in the overall mechanism of collapse. The dense condition has a slightly higher peak
536 kinetic energy than the loose column. In the free-fall phase, the dense column shows a
537 steeper increase in the horizontal kinetic energy in comparison to the loose column. This
538 indicates that the dense granular mass is pushed farther away more quickly than with the
539 loose column. A loose column exhibits higher vertical kinetic energy which may be due to
540 particle rearrangement resulting in densification of the granular mass. Figure 4.17 shows
541 that the loose sample densifies as the flow evolves. Both dense and loose granular columns
542 dilate during the initial stage of collapse, this is due to grains experiencing shear along the
543 shear-failure surface. In both cases, the granular mass attains similar packing density at the
544 end of the flow. The dense granular column dilates, while the loose column compacts to

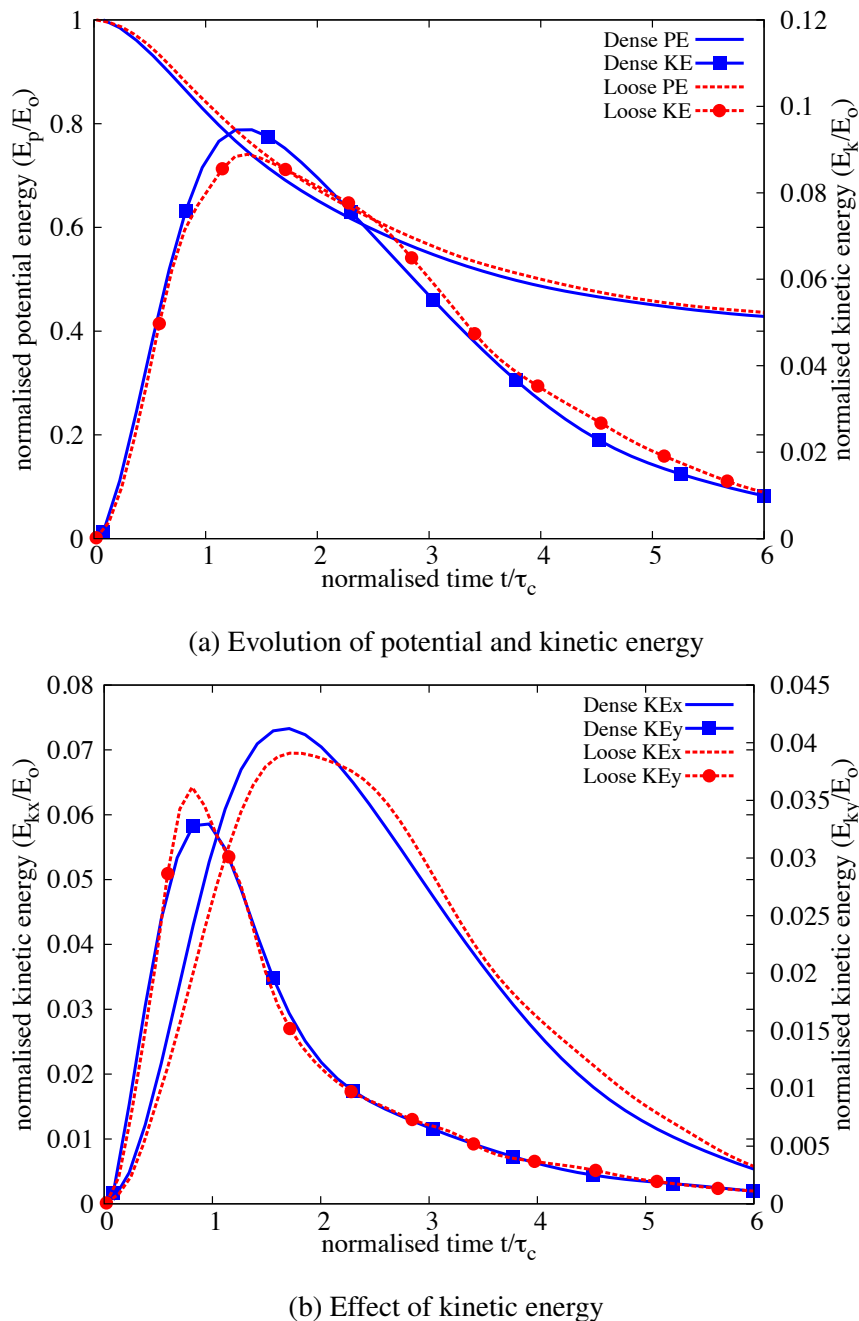
4.3 Role of initial grain properties on the collapse of granular columns

Figure 4.16 Effect of density on the run-out evolution $a = 0.8$.Figure 4.17 Evolution of local packing density with time $a = 0.8$.

545 achieve the same critical density. The dense condition has higher mobilised potential energy
546 during the initial stage of collapse, which yields higher horizontal kinetic energy for the
547 flow. However in loose conditions, a higher proportion of the available energy is lost during
548 compaction. This behaviour in addition to higher mobilised potential energy results in longer
549 run-out distance in dense granular column. Lajeunesse et al. (2004) observed that the flow
550 comes to rest at around $3\tau_c$, but the grains continue to re-arrange until $6\tau_c$. Similar behaviour
551 is observed in DEM simulations.

552 In order to remove the effect of crystallisation on the run-out behaviour, a highly poly-
553 disperse sample ($r = d_{max}/d_{min} = 6$) is used. The flow kinematics of a dense (relative
554 density $D_r = 74\%$) and a loose ($D_r = 22\%$) granular column with aspect ratio of 0.8 is
555 studied. Figure 4.19 shows the evolution of the normalised run-out with time for dense and
556 loose granular columns with an initial aspect ratio of 0.4. Similar to the previous case, the
557 dense granular column exhibits longer run-out distance (figure 4.19). Figure 4.21a show
558 the evolution of energy with time for dense and loose conditions. The peak kinetic energy
559 in the dense condition is $\sim 20\%$ higher than the loose condition. Due to compaction of
560 grains in loose condition, almost 20% of the normalised initial potential energy available
561 for the collapse is lost in densification due to grain rearrangements in comparison to the
562 dense condition (figure 4.21). The compaction of grains in loose column and the dilation
563 in dense column results in significantly different flow structure, especially at the flow front
564 (figure 4.20). As the loose column densifies, more granular mass is pushed to the flow front
565 resulting in higher vertical effective stress. The loose column exhibits a more parabolic final
566 deposit profile in comparison to the dense column, which shows a triangular deposit at the
567 front.

568 In short columns, only a part of the granular column above the failure surface participates
569 in the flow. However, it appears that the collapse for large aspect ratios mixes two very
570 different dynamics: the first stage shows a large vertical acceleration, while the second stage
571 consists of a “conventional” horizontal granular flows. This section investigates the effect
572 of density on the run-out behaviour of tall columns. Similar to short columns, the dense
573 granular column with an aspect ratio of 6 shows higher run-out distance in comparison to
574 the loose condition. The dense granular column flows almost twice as much as that of the
575 loose column. Unlike short columns, the evolution of run-out is different even at the initial
576 stage of the collapse. The dense granular column, which has higher initial potential energy
577 shows a rapid increase in the run-out due to free-fall and higher mobilised potential energy.
578 During this stage of collapse, the dense granular column has 15 % higher normalised kinetic
579 energy available for the horizontal push. This results in a longer run-out distance for a dense
580 granular column in comparison to an initially loose granular column.

Figure 4.18 Effect of density on the energy evolution $a = 0.8$.

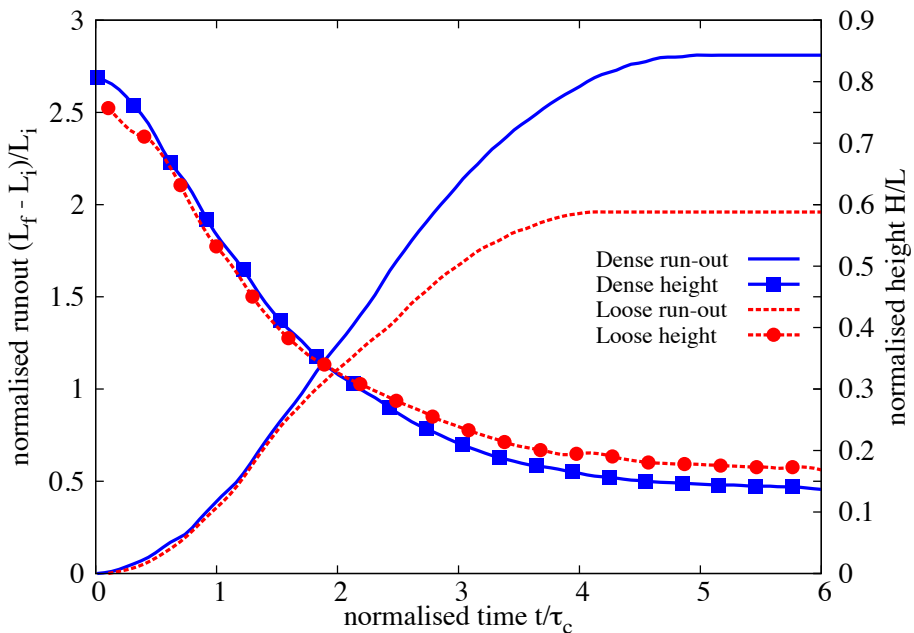


Figure 4.19 Effect of density on the run-out evolution $a = 0.8$ (poly-dispersity $r = 6$).

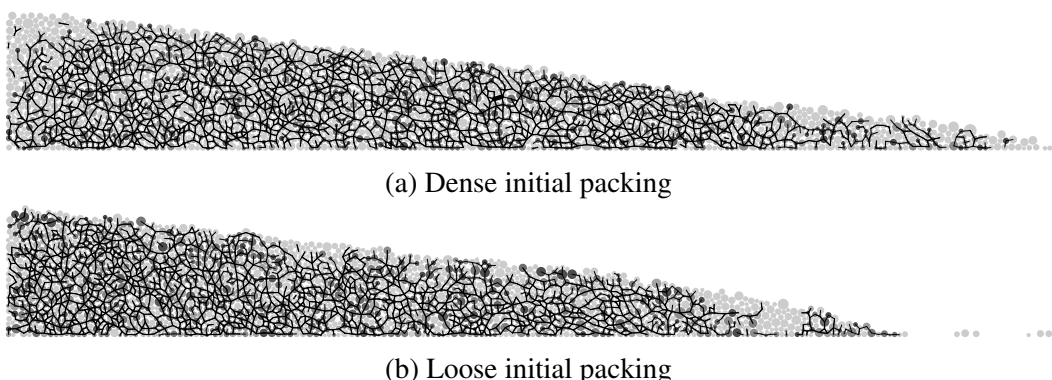


Figure 4.20 Snapshots of granular column collapse at $t = 6\tau_c$ ($a = 0.8$).

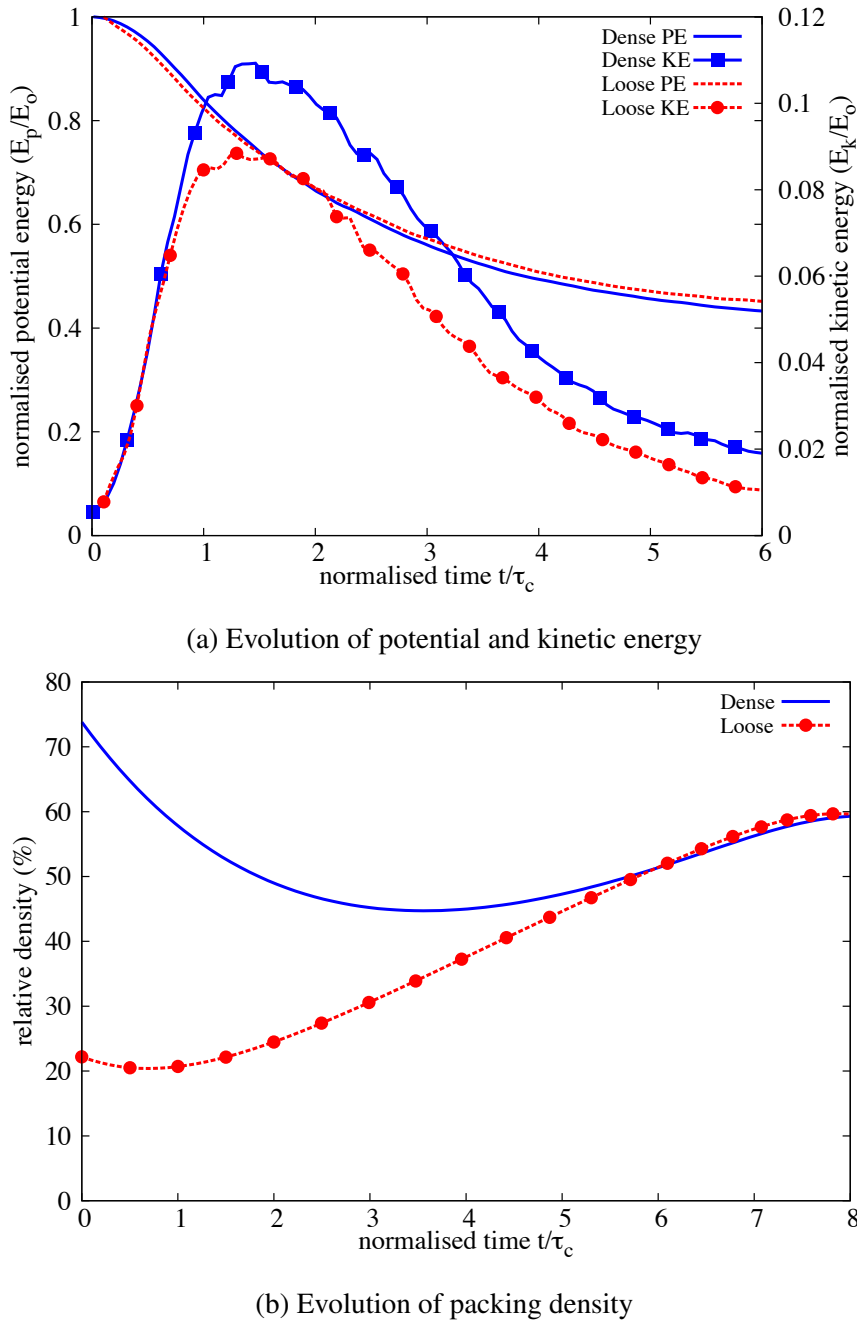
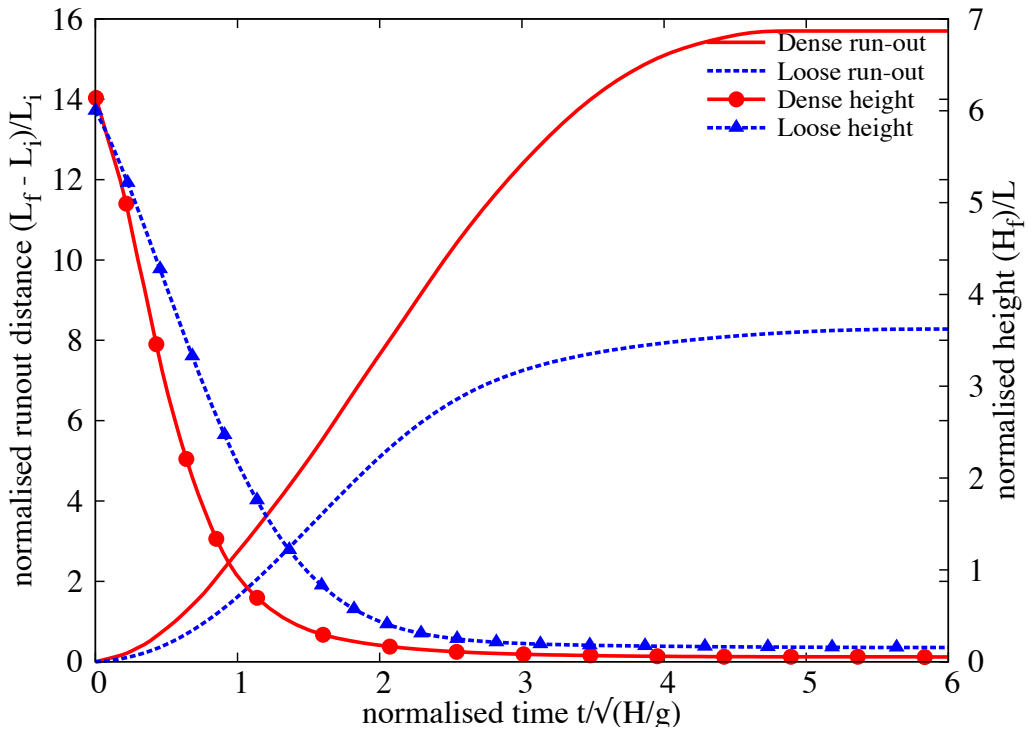
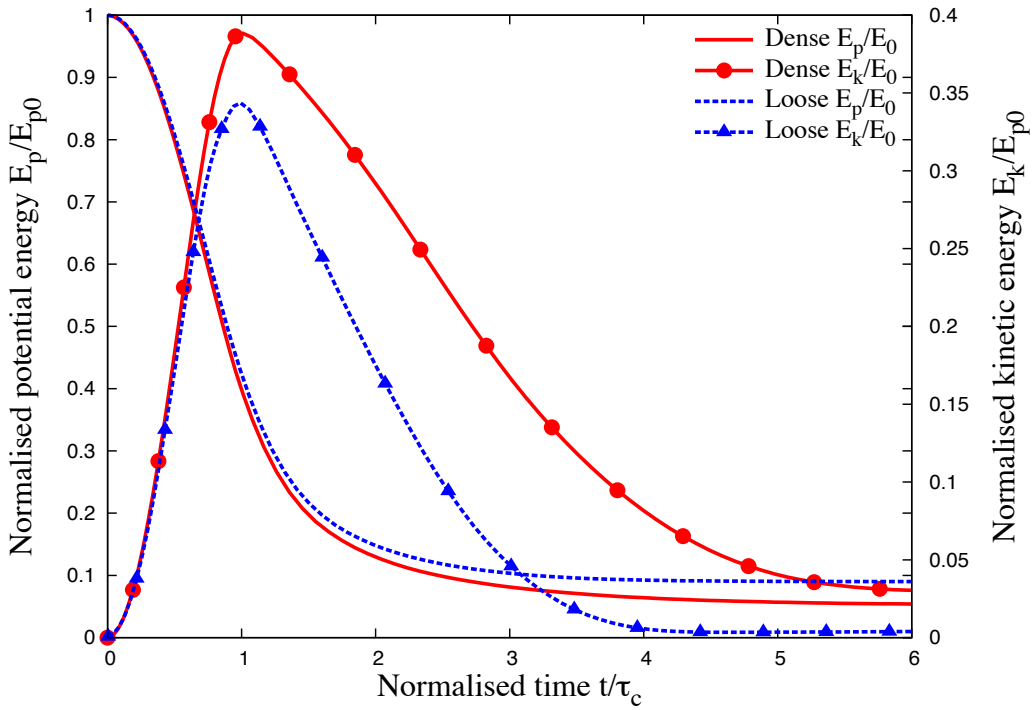


Figure 4.21 Effect of density on the evolution of energy and packing fraction $a = 0.8$ (poly-dispersity ‘r’ = 6).



(a) Effect of density on run-out evolution.



(b) Effect of density on energy evolution.

Figure 4.22 Effect of density on the run-out behaviour and energy evolution $a = 0.6$.

The initial packing fraction and the distribution of kinetic energy in the system has a 581
 significant influence on the flow kinematics and the run-out behaviour. The next section will 582
 discuss the influence of triggering mechanism and the distribution of the kinetic energy in 583
 the granular system on the run-out behaviour. 584

4.4 Slopes subjected to horizontal excitation

585

Transient granular flows occur very often in nature. Well-known examples are rockfalls, 586
 debris flows, and aerial and submarine avalanches. In the geotechnical context, transient 587
 movements of large granular slopes is a substantial factor of risk due to their destructive 588
 force and the transformations they may produce in the landscape. Natural granular flows 589
 may be triggered as a result of different processes such as gradual degradation induced by 590
 weathering or chemical reactions, liquefaction and external forces such as earthquakes. Most 591
 contemporary research on granular materials deals with steady-state flow. Transients and 592
 inhomogeneous boundary conditions are much less amenable to observation and analysis, 593
 and have thus been less extensively studied despite their primary importance in engineering 594
 practice. In most cases of granular flow, an initially static pile of grains is disturbed by external 595
 forces, it then undergoes an abrupt accelerated motion and spreads over long distances before 596
 relaxing to a new equilibrium state. The kinetic energy acquired during destabilisation is 597
 dissipated by friction and inelastic collisions. 598

This section investigates the ability of MPM, a continuum approach, to reproduce the 599
 evolution of a granular pile destabilised by an external energy source. In particular, a central 600
 issue is whether the power-law dependence of run-out distance and time observed with 601
 respect to the initial geometry or energy can be reproduced by a simple Mohr-Coulomb 602
 plastic behaviour for granular slopes subjected an horizontal excitation. The effects of 603
 different input parameters, such as the distribution of energy and base friction, on the run-out 604
 kinematics are studied by comparing the data obtained from DEM and MPM simulations. 605

4.4.1 Numerical set-up

606

The DEM sample was composed of ~ 13000 disks with a uniform distribution of diameters 607
 by volume fractions ($d_{max} = 1.5d_{min}$). The mean grain diameter and mass are $d \simeq 2.455$ mm 608
 and $m \simeq 0.0123$ kg, respectively. The grains are first poured uniformly into a rectangular 609
 box of given width and then the right-hand side wall is shifted far to the right to allow the 610
 grains to spread. A stable granular slope of 13.2° is obtained when all grains come to rest; 611
 see figure 4.23. This procedure leads to a mean packing fraction $\simeq 0.82$. Soil grains with 612

613 a mean density of 2600 kg/m³ and internal friction coefficient of 0.4 between grains are
 614 considered.

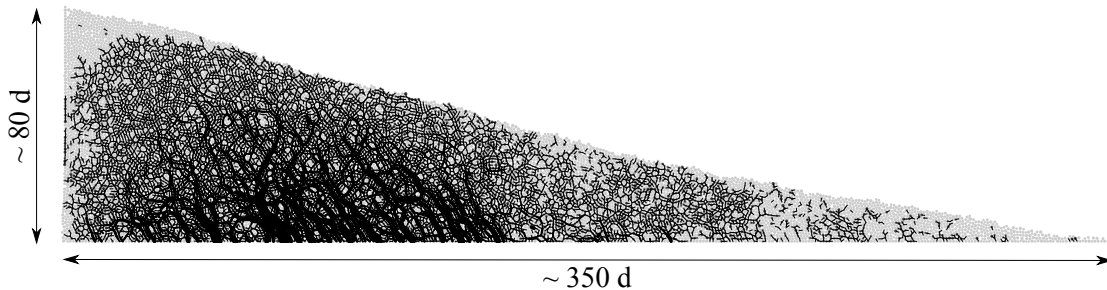


Figure 4.23 Initial geometry and dimensions of the pile subjected to a horizontal excitation.

615 The initial static pile was set into motion by applying a horizontal gradient velocity
 616 $v_{0x}(y) = k(y_{max} - y)$ with $k > 0$. The evolution of the pile geometry and the total kinetic
 617 energy as a function of the initial input energy E_0 is studied. The run-out distance L_f is the
 618 distance of the rightmost grain, which is still in contact with the main mass when the pile
 619 comes to rest. The run-out will be normalised by the initial length L_0 of the pile, as in the
 620 experiments of collapsing columns. The total run-out duration t_f is the time taken by the pile
 621 to reach its final run-out distance L_f .

622 For grain-scale simulations, classical DEM and Contact Dynamics approaches were used.
 623 This research was done in collaboration with Patrick Mutabaruka, University of Montpellier,
 624 who performed Contact Dynamics (CD) simulations that are presented in this section. A
 625 detailed description of the Contact Dynamics method can be found in Jean (1999); Moreau
 626 (1993); Radjai and Dubois (2011); Radjai and Richefeu (2009). The CD method is based on
 627 implicit time integration of the equations of motion and a non-smooth formulation of mutual
 628 exclusion and dry friction between particles. The CD method requires no elastic repulsive
 629 potential and no smoothing of the Coulomb friction law for the determination of forces. For
 630 this reason, the simulations can be performed with large time steps compared to discrete
 631 element simulations. The unknown variables are particle velocities and contact forces, which
 632 are calculated at each time step by taking into account the conservation of momenta and the
 633 constraints due to mutual exclusion between particles and the Coulomb friction. An iterative
 634 algorithm based on a non-linear Gauss-Seidel scheme is used. The only contact parameters
 635 within the CD method are the friction coefficient μ , the normal restitution coefficient ϵ_n and
 636 the tangential restitution coefficient ϵ_t between grains.

637 In MPM simulations, the material point spacing is adopted to be the same as the mean
 638 grain diameter in DEM. A mesh size of 0.0125m is adopted with 25 material points per
 639 cell. The effect of mesh size and the number of material points per cell is investigated
 640 in section 4.4.2. The initial configuration of the slope in MPM is shown in figure 4.24a.

Frictional boundary conditions are applied on the left and the bottom boundaries by applying constraints to the nodal acceleration. The initial vertical stress of the granular pile in equilibrium, before the horizontal excitation, in the MPM simulation is shown in figure 4.24b. The distribution of the initial gradient horizontal excitation energy of 50 J on the granular pile is shown in figure 4.24c. The Mohr-Coulomb model with no dilation is used to simulate the continuum behaviour of the granular pile. Periodic shear tests using CD (figure 4.25a), reveals a macroscopic friction coefficient of 0.22. The evolution of inertial number with friction is presented in figure 4.25b.

The natural units of the system are the mean grain diameter d , the mean grain mass m and acceleration due to gravity g . For this reason, the length scales are normalised by d , time by $(d/g)^{1/2}$, velocities by $(gd)^{1/2}$ and energies by mgd .

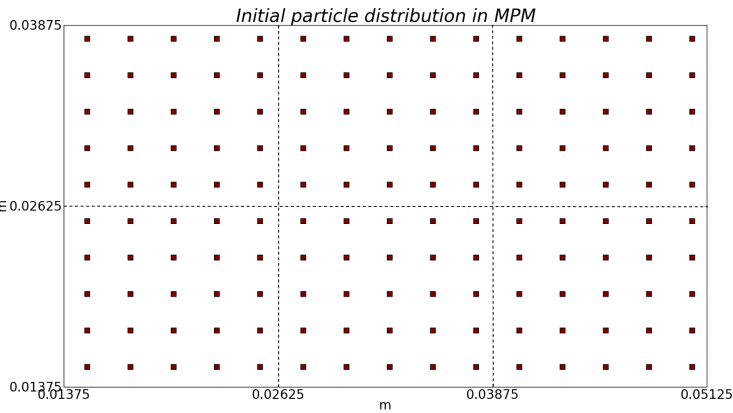
4.4.2 Effect of mesh size and number of material points per cell

The accuracy of MPM simulations largely depends on the number of material points representing the continuum. MPM utilises a grid to compute the deformation of a continuum, hence the size of the cells affects the accuracy of the results. Generally in MPM, the number of particles per cell controls the accuracy of the simulation. Guilkey et al. (2003) recommends higher particle density, such as 4 particles per cell, for large deformation problems. Very low particle density will result in non-physical opening of cracks in large deformation simulations. However, a higher value of particle density affects the computational time.

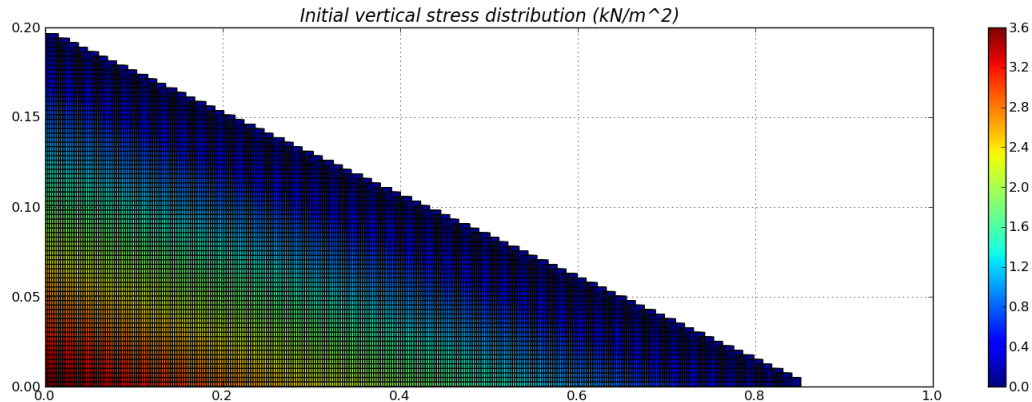
Abe et al. (2013) observed that for a coarse mesh, the numerical error decreases with an increase in the number of material points per cell. In contrast, they observed an opposite trend for fine meshes. The influence of numerical noise due to particles crossing the background mesh is not observed in coarse meshes. Coetzee et al. (2005) also found that the numerical error decreases with increase in mesh refinement.

In the present study, the effect of mesh size and the number of material points per cell on the run-out behaviour of a static slope subjected to a horizontal excitation is investigated. A mesh size of 0.0125 m is adopted. The number of material points per cell (PPC) is varied as 4, 16, 25, 36, 64, 81 and 100.

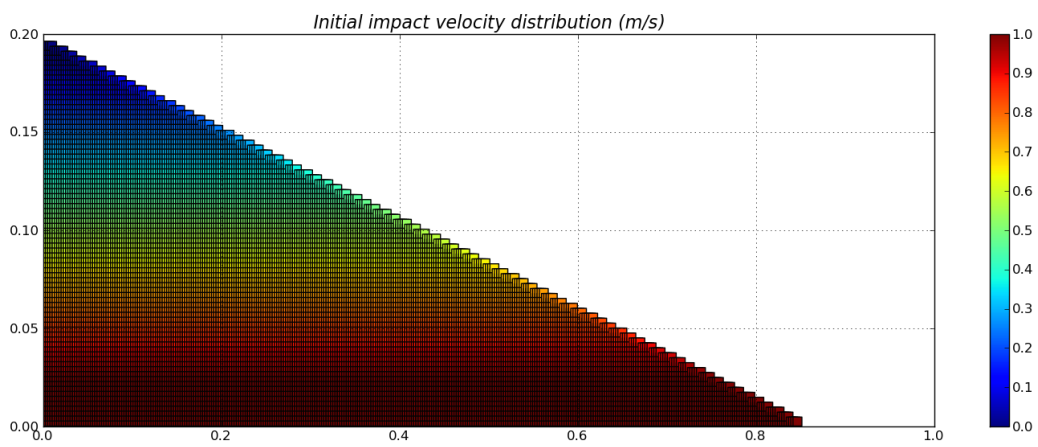
The effect of the number of material points on the run-out behaviour is presented in figure 4.26. At a low input energy of 50 J, 4 and 16 material points per cell result in a longer run-out distance, whereas the run-out distance converges when the number of PPC is more than 25. However, at a high input energy of 500 J, both 4 and 16 PPC predict almost the same run-out distance, but the run-out is higher than the run-out predicted with more than 25 material points per cell.



(a) Initial configuration of material points per cell. 25 material points per cell. Cell size of 0.0125m.



(b) Initial stress in MPM



(c) Initial horizontal velocity for a pile subjected to a horizontal velocity of 50J.

Figure 4.24 Initial configuration for the MPM simulation of a pile subjected to horizontal velocities.

4.4 Slopes subjected to horizontal excitation

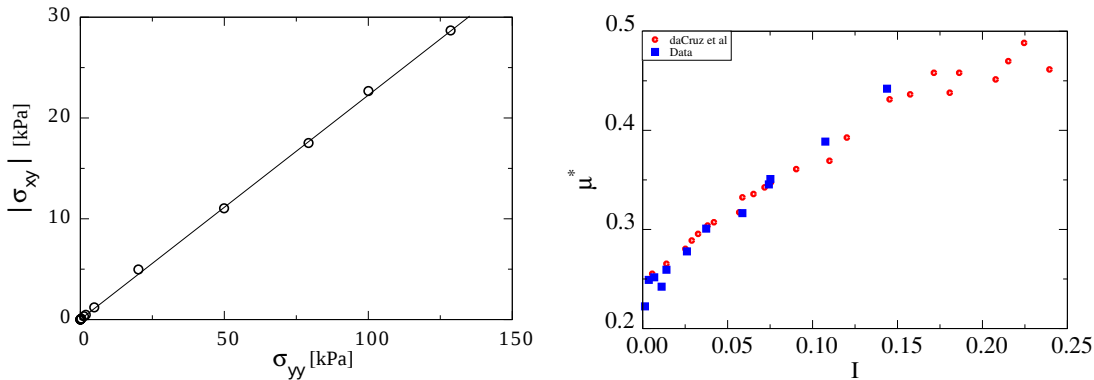
(a) Evaluation of the critical state friction angle. (b) Evolution of Inertial number with friction μ .

Figure 4.25 Periodic shear test using CD (Mutabaruka, 2013).

The evolution of the granular pile during the initial stage of flow is shown in figure 4.27 for different numbers of material points per cell. At low input energy, fewer material points per cell results in a larger separation of the spreading mass from the left wall. Distinct shear bands can be observed for more than 16 PPC. The flow structure remains unchanged with increase in PPC of more than 25. At a higher input energy (figure 4.28), almost all cases predict similar flow structure, except in the case of 4 PPC.

Figure 4.29 shows the evolution of kinetic energy with time for varying number of material points per cell. At low input energy, the horizontal kinetic energy evolution is identical for all cases. A slightly quicker run-out evolution during the spreading phase can be observed for the case of 4 PPC. However, increase in the number of material points per cell significantly affects the evolution of the vertical kinetic energy E_{ky} . At low energy, a large proportion of the input energy is dissipated in the destabilisation process. This results in material points falling behind the spreading mass to the fill the cavity. Fewer material points per cell results in cell-crossing noise as the material points filling the cavity experience free-fall due to gravity. The effect of cell-crossing noise can be seen in the oscillation of vertical kinetic energy for fewer material points per cell. However, at high input energy, most of the input velocity is dissipated during the spreading process. This means that only a small fraction of energy is available in the vertical component resulting in almost identical behaviour for all cases. Four material points per cell predicts a higher peak vertical kinetic energy in comparison with other case and unlike the low energy case, no oscillations are observed for high input energy.

The effect of mesh size on the flow kinematics is studied by comparing two mesh sizes: 0.01 m and 0.0125 m (figure 4.30). It can be observed that the run-out distance converges with an increase in the number of material points per cell in both cases. Less than 1% difference in the run-out distance is observed between a mesh size of 0.0125 m and 0.01 m.

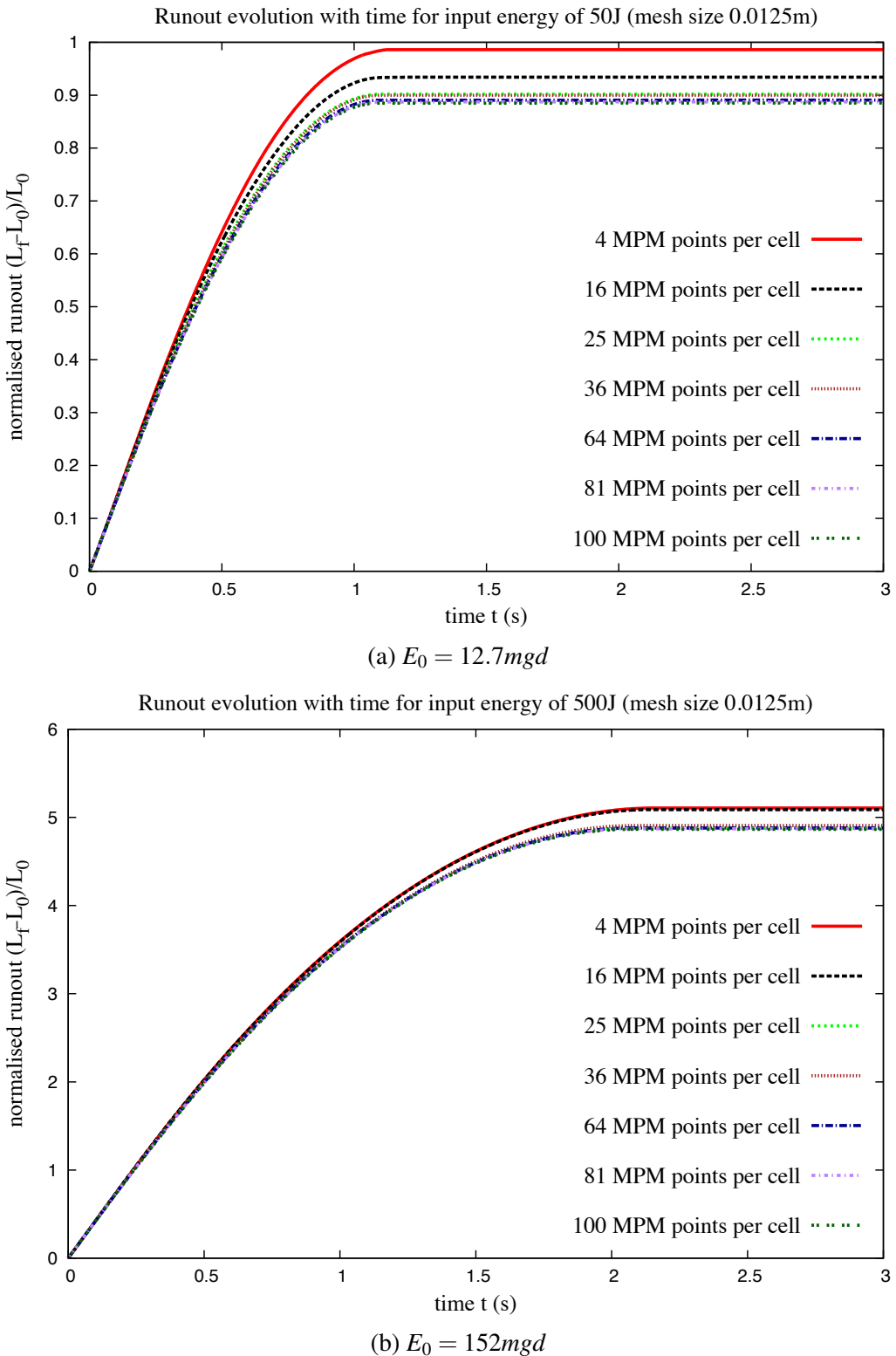


Figure 4.26 Evolution of run-out with time for varying material points per cell for a slope subjected to a horizontal velocity.

4.4 Slopes subjected to horizontal excitation

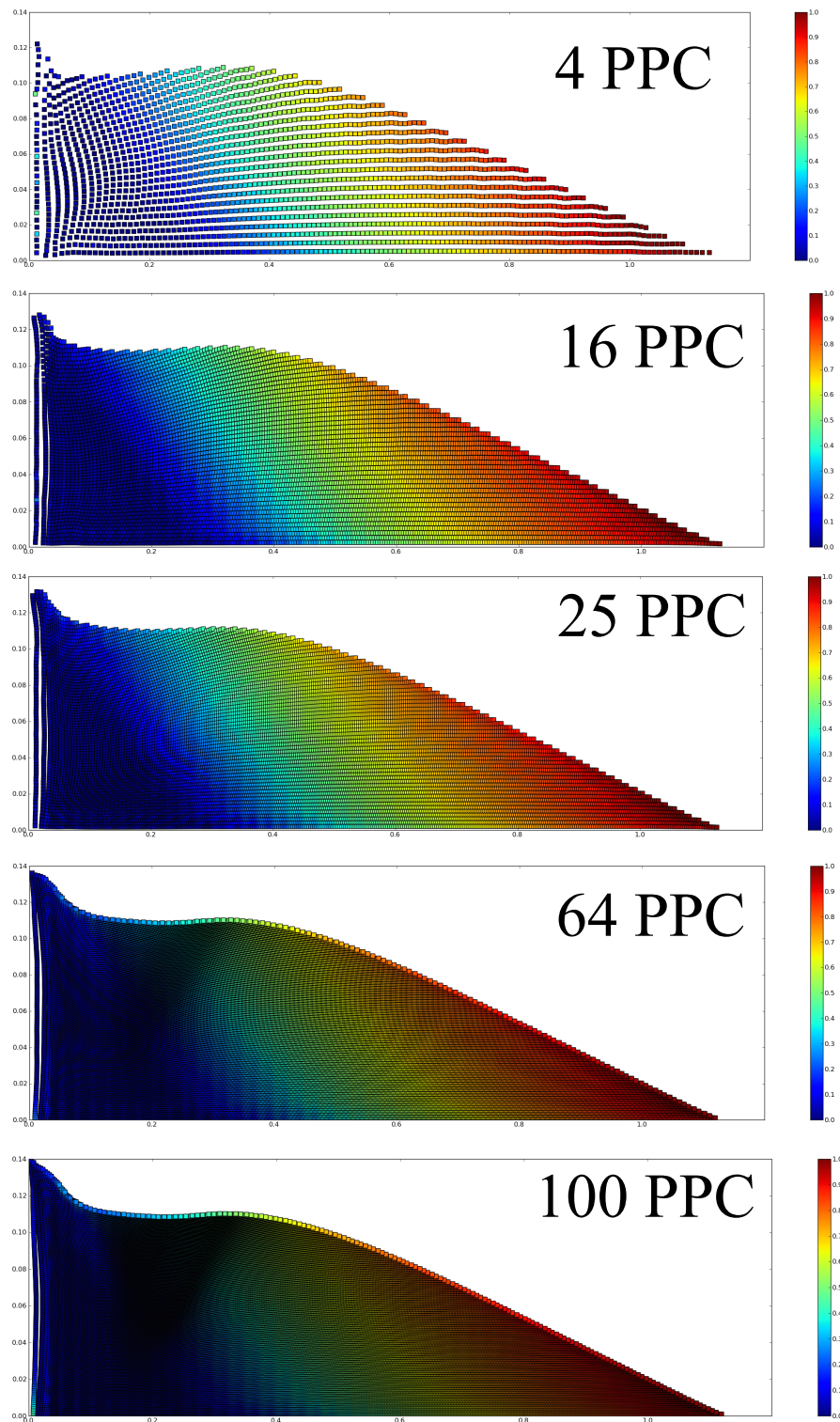


Figure 4.27 Effect of number of material points on cell on the run-out behaviour $E_0 = 12.7mgd$. Velocity profile (m/s) of granular pile subjected to gradient horizontal loading.

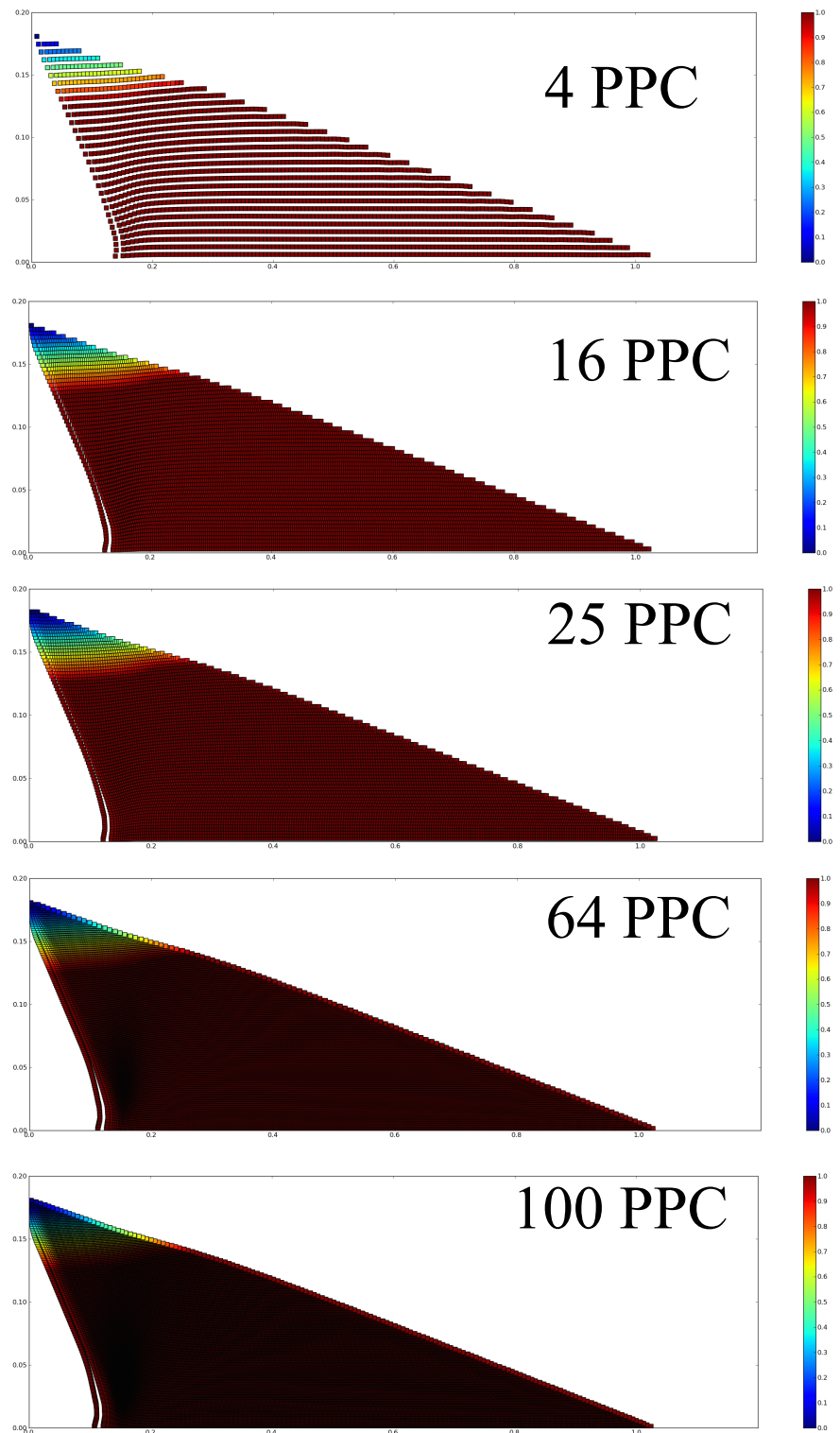


Figure 4.28 Effect of number of material points on cell on the run-out behaviour $E_0 = 152mgd$. Velocity profile (m/s) of granular pile subjected to gradient horizontal loading.

4.4 Slopes subjected to horizontal excitation

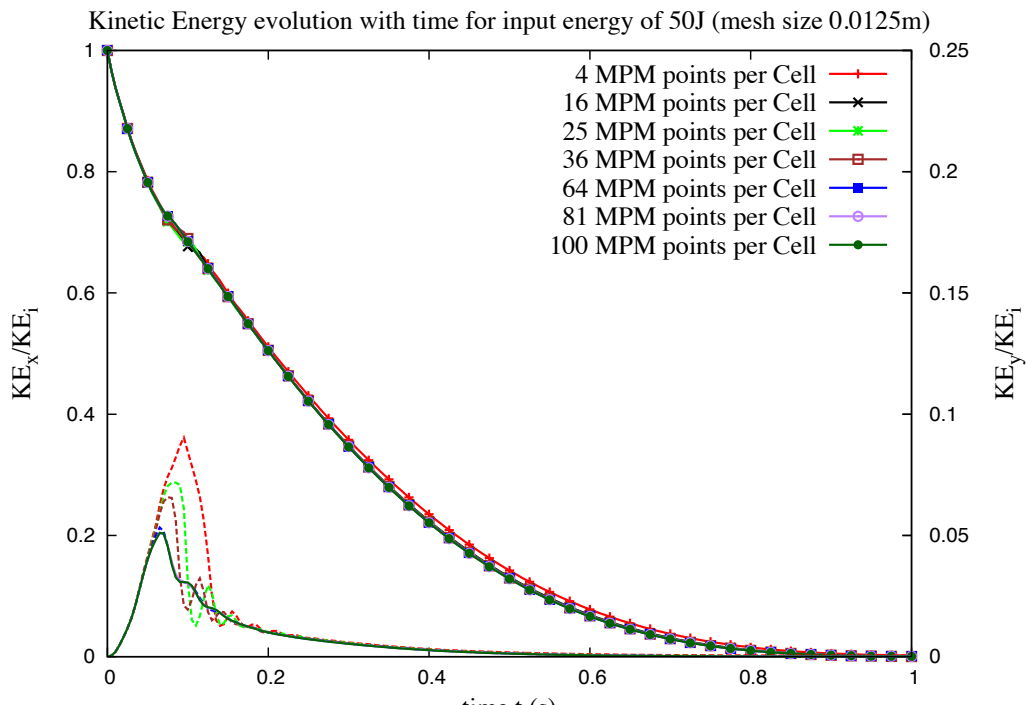
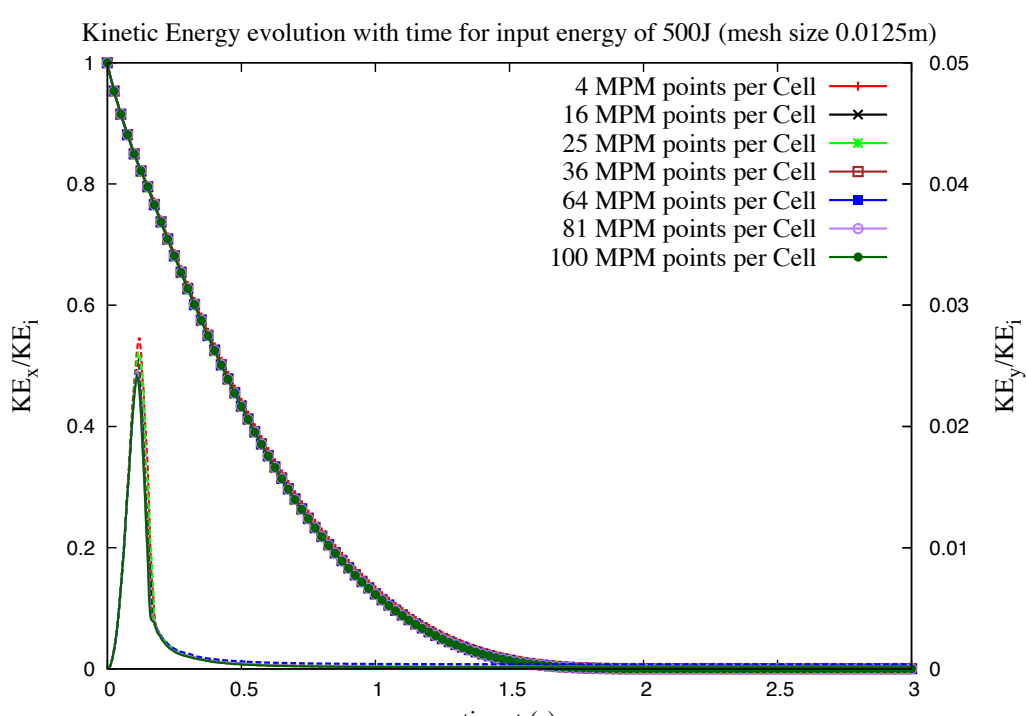
(a) $E_0 = 12.7mgd$ (b) $E_0 = 152mgd$

Figure 4.29 Evolution of kinetic with time for varying material points per cell for a slope subjected to a horizontal excitation.

700 The final run-out duration is almost unaffected by the increase in the number of material
701 points per cell.

702 This shows that the run-out distance is affected by the number of material points per cell.
703 However, the duration of the run-out is independent of the number of material points per
704 cell. The computation time increases with increase in the number of material points per cell
705 and decrease in the mesh size. However, the run-out distance converges with increase in
706 number of material points per cell. Hence, an optimum number of 25 material points per cell
707 is adopted in this case. In summary, for conducting a successful MPM analysis, a careful
708 selection of the mesh size and the number of particles is necessary.

709 4.4.3 Evolution of pile geometry and run-out

710 Figure 4.31 shows the initial evolution of the granular slope subjected to an initial horizontal
711 energy $E_0 = 61$ (in dimensionless units) using MPM. As the granular slope is sheared along
712 the bottom, the shear propagates to the top leaving a cavity in the vicinity of the left wall. This
713 cavity gets partially filled as the granular mass at the top collapse behind the flowing mass
714 due to inertia. Similar behaviour is observed during the initial stages of the flow evolution
715 using CD technique (figure 4.32). Due to inertia, the grains at the top of the granular heap
716 roll down to fill the cavity, while the pile continues to spread.

717 The flow involves a transient phase with a change in the geometry of the pile followed by
718 continuous spreading. The gradient of input energy applied to the granular slope mimics a
719 horizontal quake. Despite the creation of a cavity behind the flowing mass, the granular heap
720 remains in contact with the left wall irrespective of the input energy. Figure 4.33a shows the
721 normalised run-out distance $(L_f - L_0)/L_0$ and total run-out time t_f as a function of the input
722 energy E_0 . Two regimes characterised by a power-law relation between the run-out distance
723 and time as a function of E_0 can be observed. In the first regime, corresponding to the range
724 of low input energies $E_0 < 40 \text{ mgd}$, the run-out distance observed varies as $L_f \propto (E_0)^\alpha$ with
725 $\alpha \simeq 0.206 \pm 0.012$ over nearly one decade. Overall, the run-out distance predicted by the
726 continuum approach matches the DEM simulations. At very low energies, DEM simulations
727 show longer run-out distance due to local fluidisation. The difference in the run-out between
728 DEM and CD arise mainly from the scales of description and the inelastic nature of Contact
729 Dynamics. Similar behaviour between DEM and CD approaches was observed by Radjai
730 et al. (1997).

731 While the run-out exhibits a power-law relation with the initial input energy, the DEM
732 simulations show that the flow duration remains constant at a value $t_f \simeq 60 (d/g)^{0.5}$ irrespec-
733 tive of the value of E_0 . The constant run-out time, in grain-scale simulations, indicates the
734 collapse of grain into the cavity left behind the pile. An average run-out speed can be defined

4.4 Slopes subjected to horizontal excitation

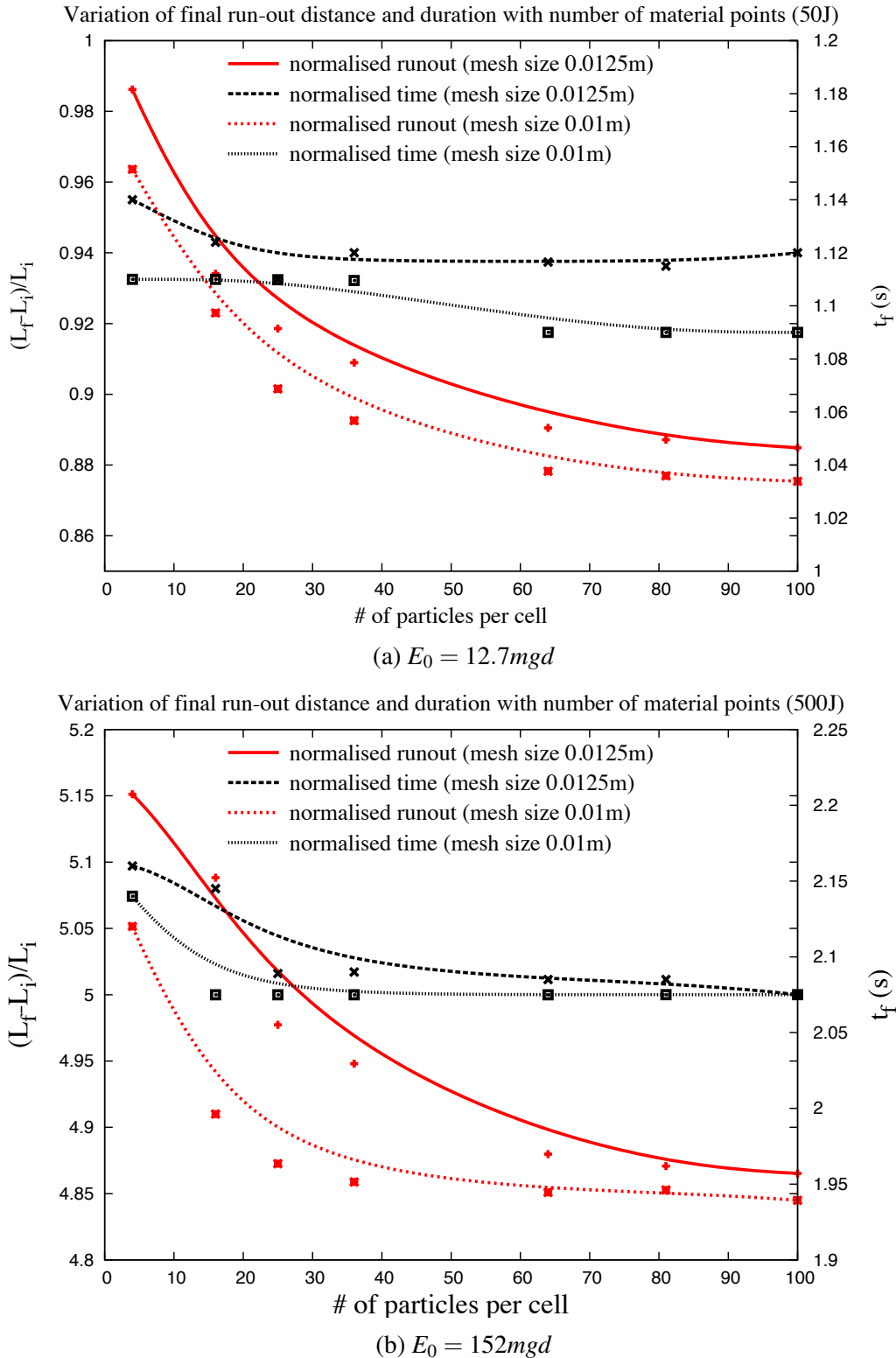


Figure 4.30 Evolution of run-out and duration of flow for varying material points per cell for a slope subjected to a horizontal excitation.

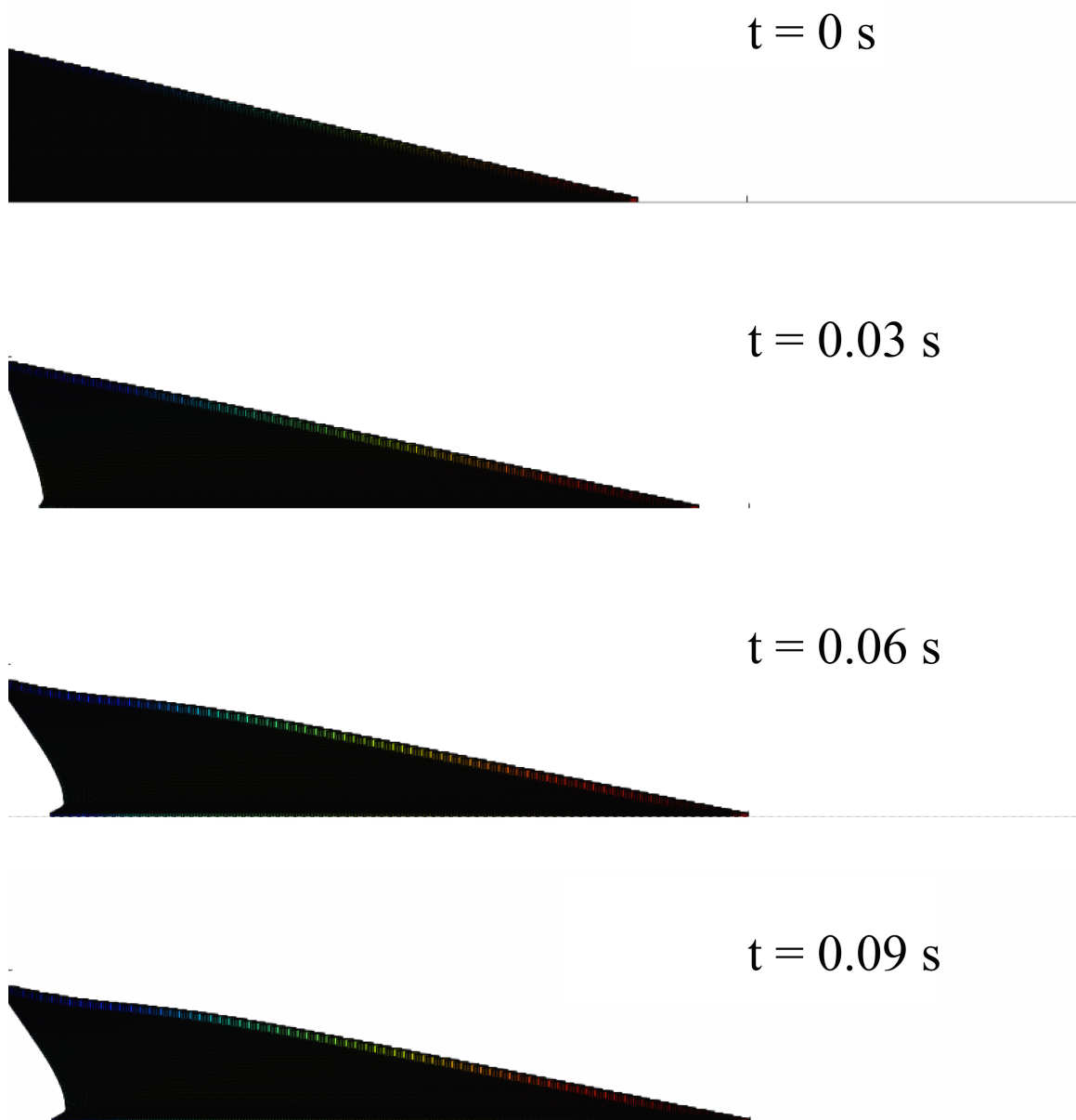


Figure 4.31 MPM simulation of the initial stages of granular pile subjected to a gradient horizontal energy.

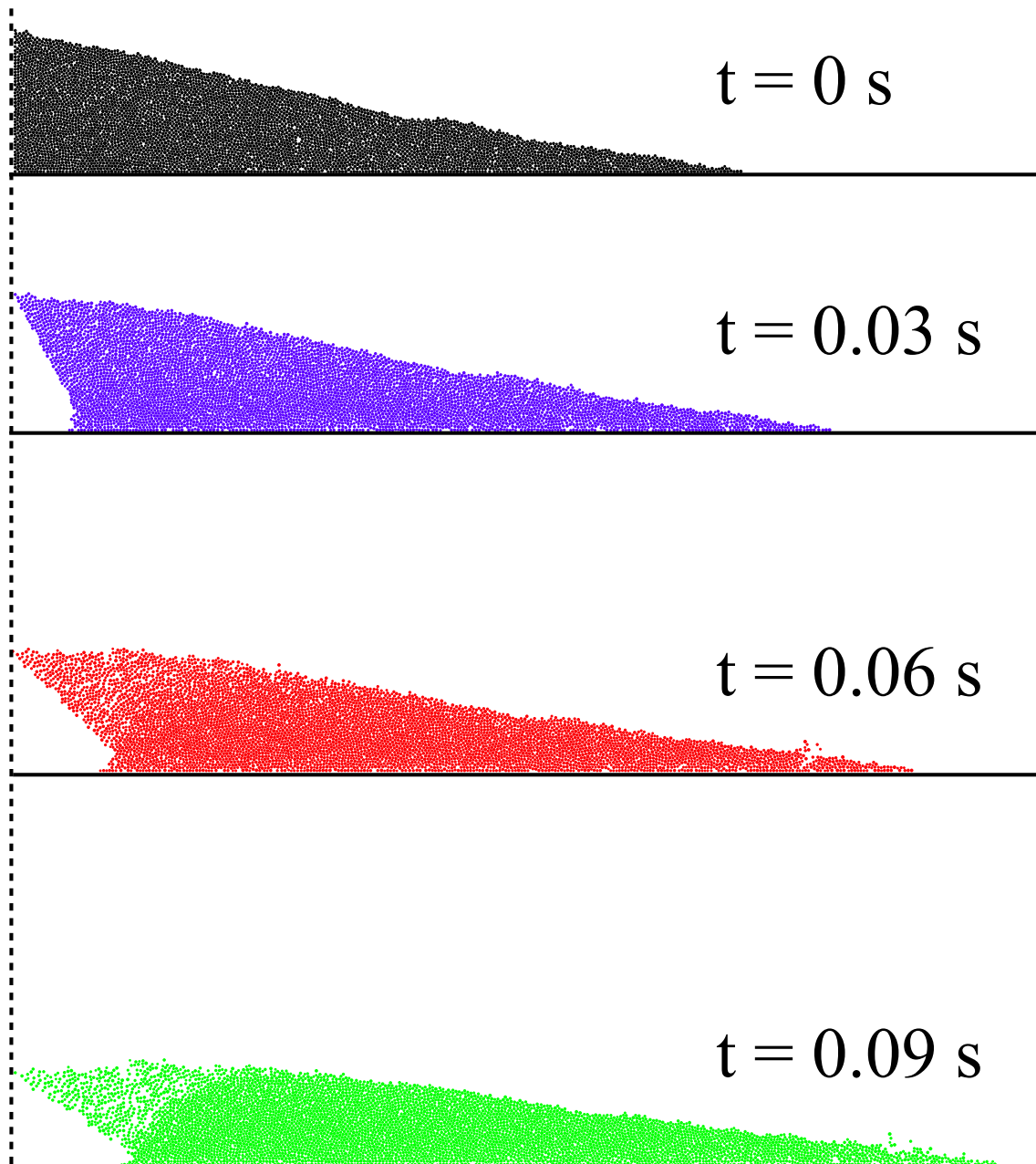


Figure 4.32 CD simulation of the initial stages of granular pile subjected to a gradient horizontal energy. (Mutabaruka, 2013).

as $v_s = (L_f - L_0)/t_f$. According to the data, $v_s \propto (E_0)^{0.52 \pm 0.012}$. The error on the exponent represents the error due to the linear fit on the logarithmic scale. Since the initial average velocity varies as $v_0 \propto (E_0)^{0.5}$, this difference between the values of the exponents suggests that the mobilised mass during run-out declines when the input energy is increased.

In the second regime, corresponding to the range of high input energies $E_0 > 40 \text{ mgd}$, the run-out distance varies as $L_f \propto (E_0)^{\alpha'}$ over one decade with $\alpha' \simeq 0.56 \pm 0.04$ while the duration increases as $t_f \propto (E_0)^{\beta'}$ with $\beta' \simeq 0.33 \pm 0.02$. Hence, in this regime the average run-out speed varies as $v_s \propto (E_0)^{0.498 \pm 0.01}$. This exponent is close to the value 0.5 in $v_0 \propto (E_0)^{0.5}$, and hence, within the confidence interval of the exponents. In the second regime, both DEM and MPM predict almost the same run-out behaviour. However, MPM predicts longer duration with increase in the input energy.

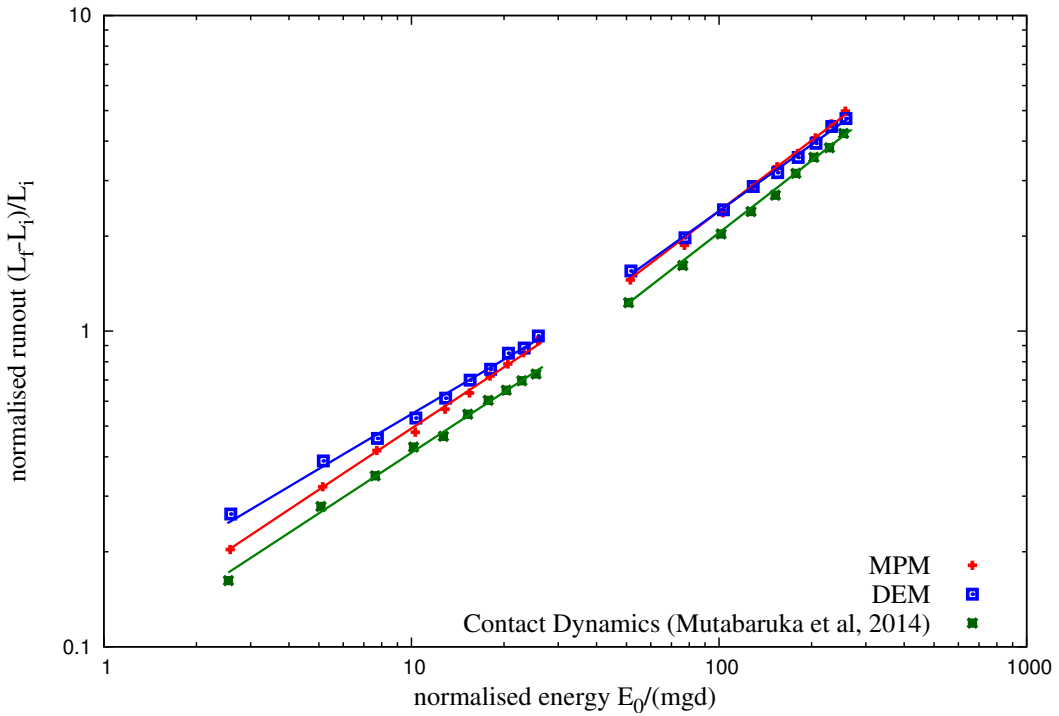
It is worth noting that a similar power-law dependence of the run-out distance and time are found in the case of granular column collapse with respect to the initial aspect ratio. In the column geometry, the grains spread away owing to the kinetic energy acquired during gravitational collapse of the column. Topin et al. (2012) found that the run-out distance varies as a power-law of the available peak kinetic energy at the end of the free-fall stage with an exponent $\simeq 0.5$. This value of exponent is lower than the run-out evolution observed in the second regime. This is, however, physically plausible since the distribution of kinetic energies at the end of the collapse is more chaotic than in this case where the energy is supplied from the very beginning in a well-defined shear mode. As pointed out by Staron et al. (2005), the distribution of kinetic energies is an essential factor for the run-out distance.

4.4.4 Decay of kinetic energy

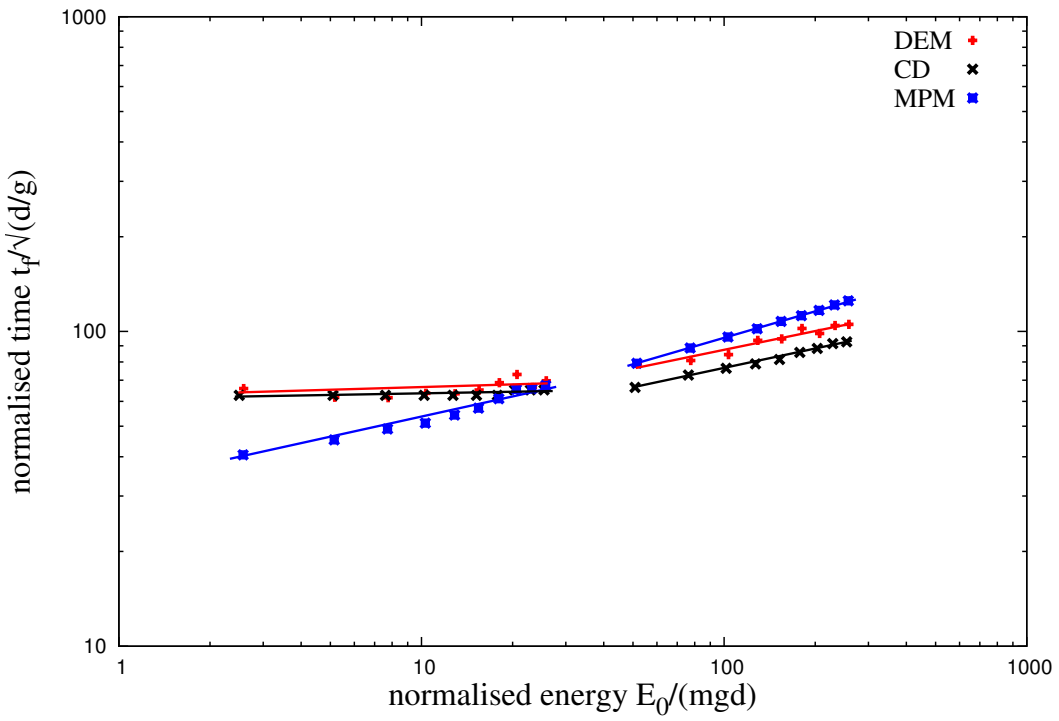
The non-trivial evolution of the pile geometry in two regimes suggests that the energy supplied to the pile is not simply dissipated by shear and friction along the bottom plane. It is important to split the kinetic energy into vertical and horizontal components (K_{Ex} and K_{Ey}) of the velocity field. Although, the input energy is in the x component, a fraction of the energy is transferred to the vertical component of the velocity field and dissipated during the transient phase. The evolution of kinetic energy is studied to understand the behaviour of granular flow that is consistent with the evolution of the pile shape.

The evolution of total kinetic energies E_k with time for different values of the input energy E_{ki} based on MPM simulations are shown in figure 4.34. The MPM simulation shows two distinct regimes in the normalised kinetic energy plot as a function of normalised time in figure 4.34b. However, the DEM simulations (figure 4.35) show that the energy evolution corresponding to the low energy regime nearly collapse on to a single time evolution. This is consistent with the observation of run-out time t_f being independent of the input energy.

4.4 Slopes subjected to horizontal excitation



(a) Run-out distance as a function of normalised input kinetic energy.



(b) Duration of run-out as a function of normalised input kinetic energy.

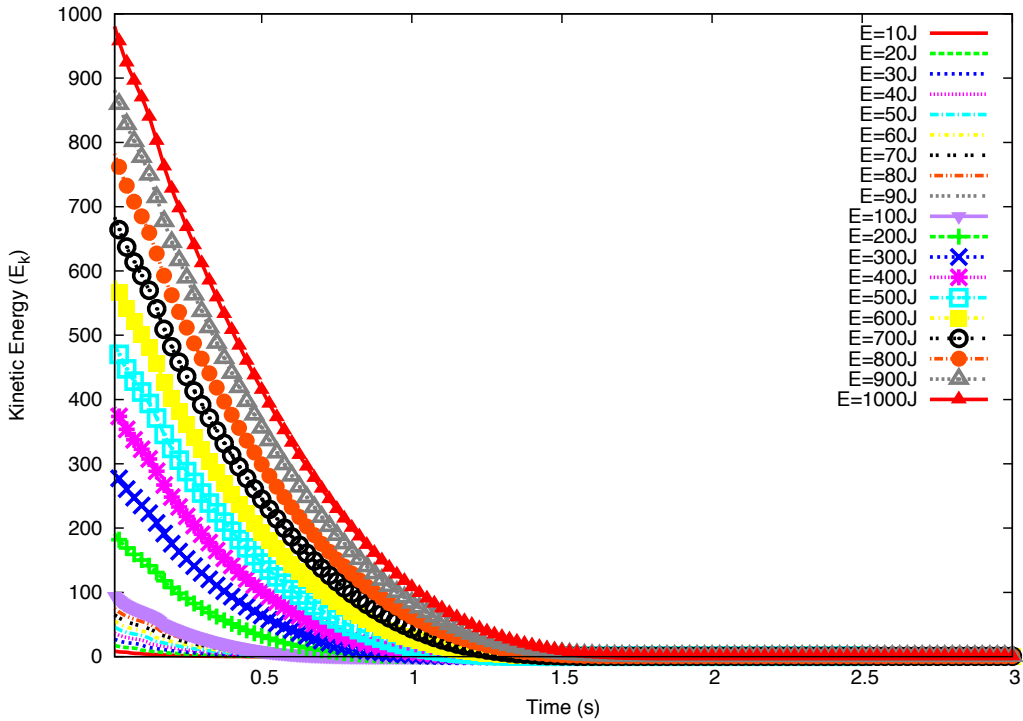
Figure 4.33 Evolution of run-out and time as a function of the normalised input energy for a pile subjected a gradient horizontal energy.

In contrast, MPM simulations predict a power law relation between the run-out duration and input energy. However, the plots corresponding to the high energy regime (figure 4.34), collapse only at the beginning of the run-out i.e. for $t < t_1 \simeq 7.5 (d/g)^{0.5}$. Although MPM simulations show a longer duration of run-out (figure 4.34), the total kinetic energy is completely dissipated at $t = 60\sqrt{d/g}$. DEM simulations predict $t = 80\sqrt{d/g}$ for the kinetic energy to be completely dissipated. This is due to grain rearrangement at the free surface (figure 4.36). The granular mass densifies as the flow progresses, after the initial dilation phase for $t = 20\sqrt{d/g}$.

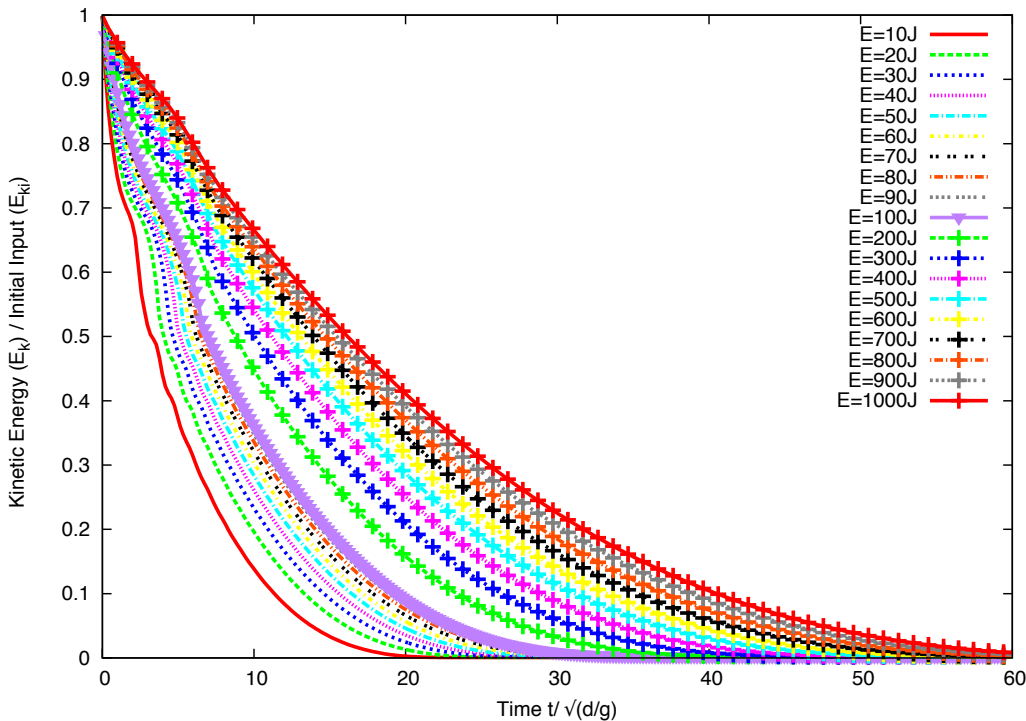
Figure 4.37 displays the evolution of kinetic energy in the translational (E_x and E_y) degrees of freedom. E_x decays similar to the total energy dissipation, but E_y increases and passes through a peak before decaying rapidly to a negligible level. The transient is best observed for E_y , which has significant values only for $t < t_1$. This energy represents the proportion of kinetic energy transferred to the y component of the velocity field due to the destabilisation of the pile and collapse of grains in the cavity behind the pile. Higher proportion of vertical acceleration E_{ky}/E_0 is observed for lower values of input energy E_0 . This means that, at lower input energies a larger fraction of the energy is consumed in the destabilisation process. Whereas at a higher input energies, most of the energy is dissipated in the spreading phase. For this reason, the total duration t_1 of this destabilisation phase is nearly the same in both regimes and its value is controlled by gravity rather than the input energy. The height of the pile being of the order of $80 d$, the total free-fall time for a particle located at this height is $\simeq 12 (d/g)^{0.5}$, which is of the same order as t_1 . DEM simulations show that the contribution of the rotational energy during the transient stage and the spreading stage is negligible.

To analyse the second phase for higher input energies, the kinetic energy E'_{kx0} at the end of the transient phase is considered. This energy is responsible for most of the run-out, hence it is expected to control the run-out distance and time. Figure 4.38 shows the evolution of E_{kx} normalised by E'_{kx0} as a function of time. The plots have seemingly the same aspect but they show different decay times. A decay time τ can be defined as the time required for E_{kx} to decline by a factor $1/2$. Figure 4.39 shows the same data in which the time t' elapsed since t_1 , normalised by τ . Interestingly, now all the data nicely collapse on to a single curve. However, this curve can not be fitted by simple functional forms such as variants of exponential decay. This means that the spreading of the pile is not a self-similar process in agreement with the fact that the energy fades away in a finite time t'_f .

4.4 Slopes subjected to horizontal excitation



(a) Evolution of total kinetic energy with time.



(b) Evolution of normalised kinetic energy with normalised time.

Figure 4.34 Evolution of kinetic energy with time (MPM) for a pile subjected to gradient input velocities.

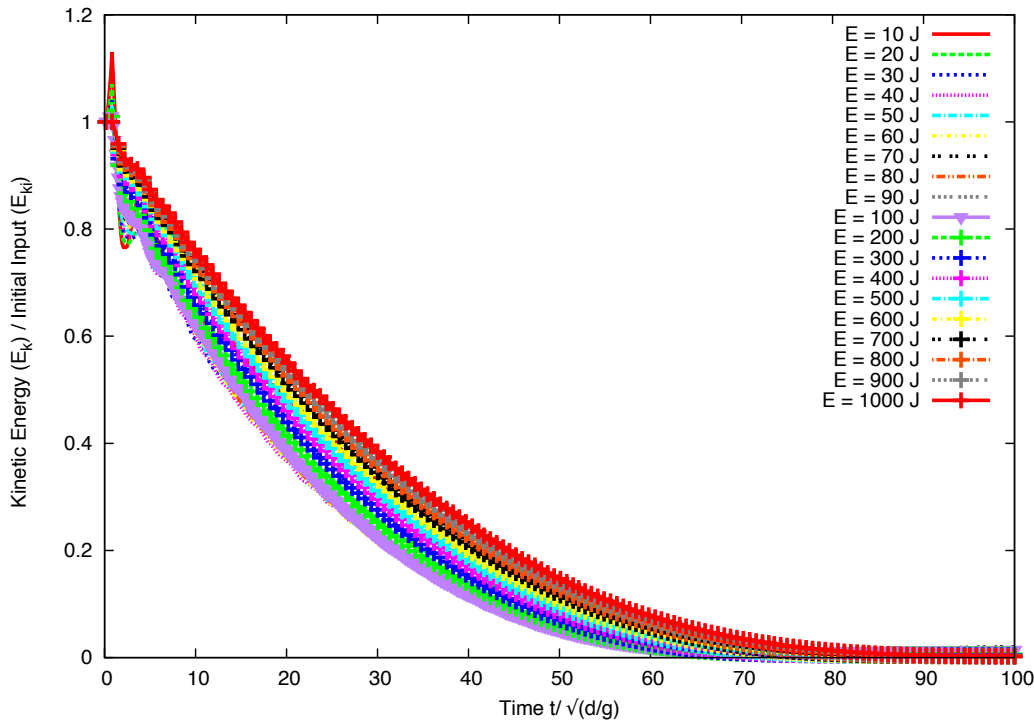


Figure 4.35 Evolution of normalised kinetic energy with normalised time for a pile subjected to gradient input velocities.

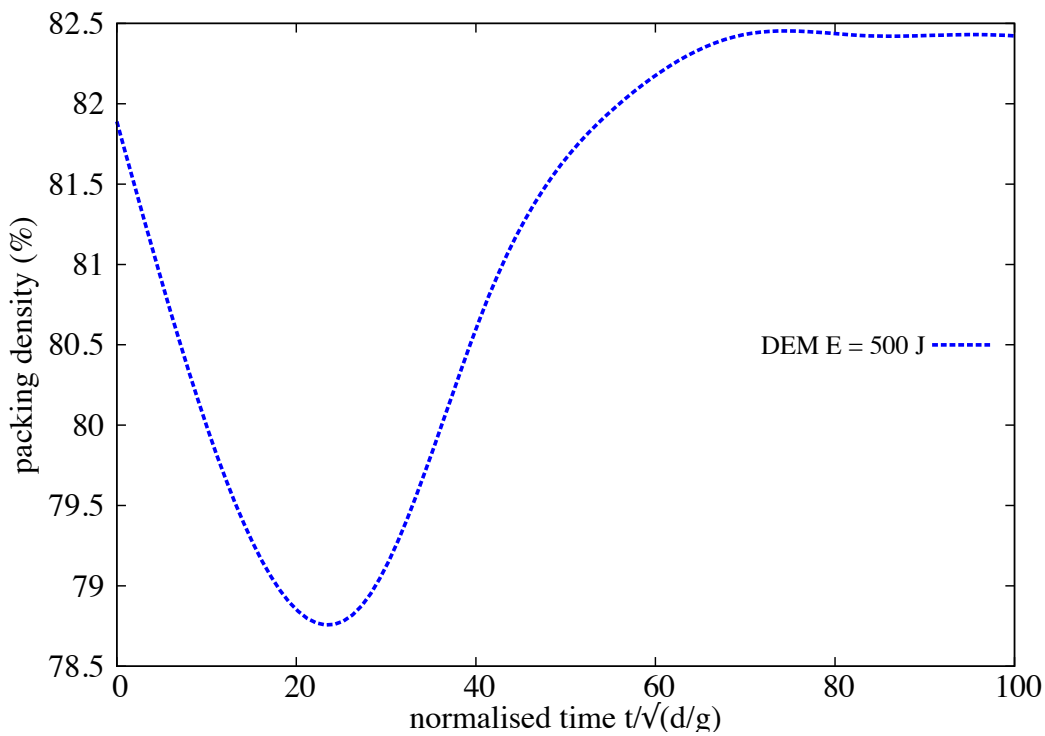
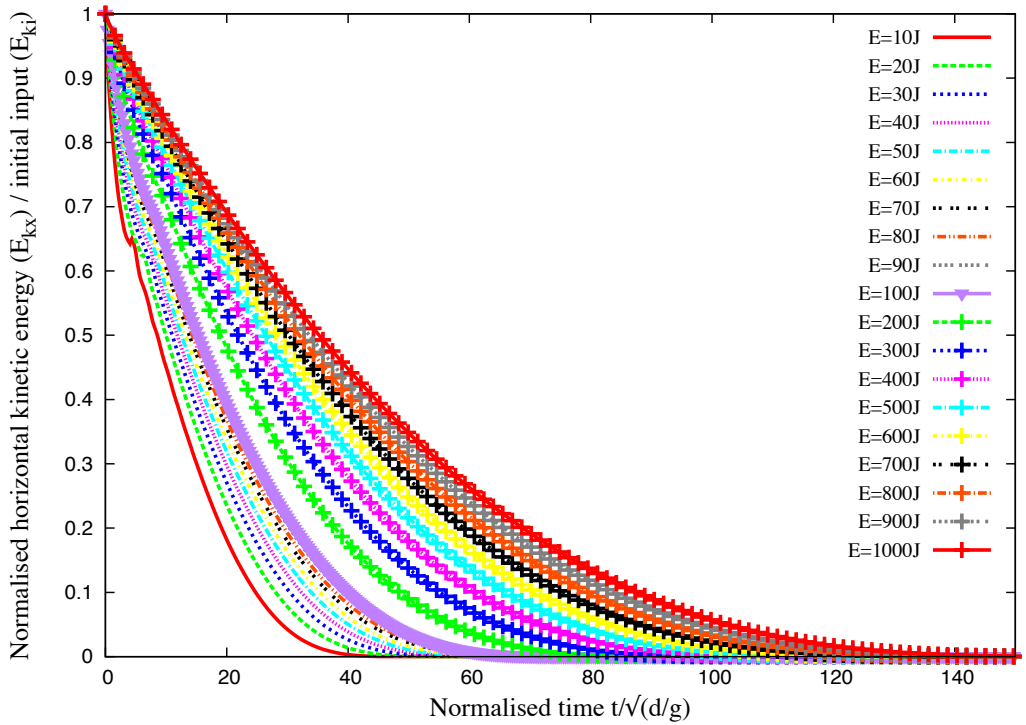
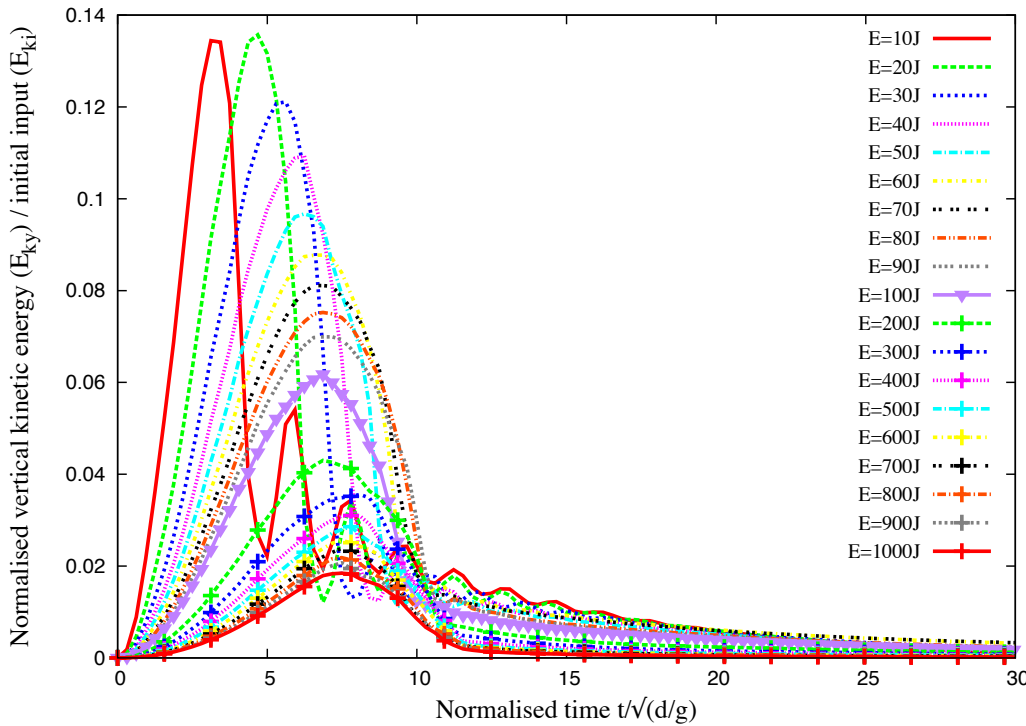


Figure 4.36 Evolution of packing density with time $E_0 = 152\text{mgd}$ (DEM).

4.4 Slopes subjected to horizontal excitation



(a) Evolution of normalised horizontal kinetic energy with time.



(b) Evolution of normalised vertical kinetic energy with time.

Figure 4.37 Evolution of vertical and horizontal kinetic energy with time (MPM) for a pile subjected to gradient input velocities.

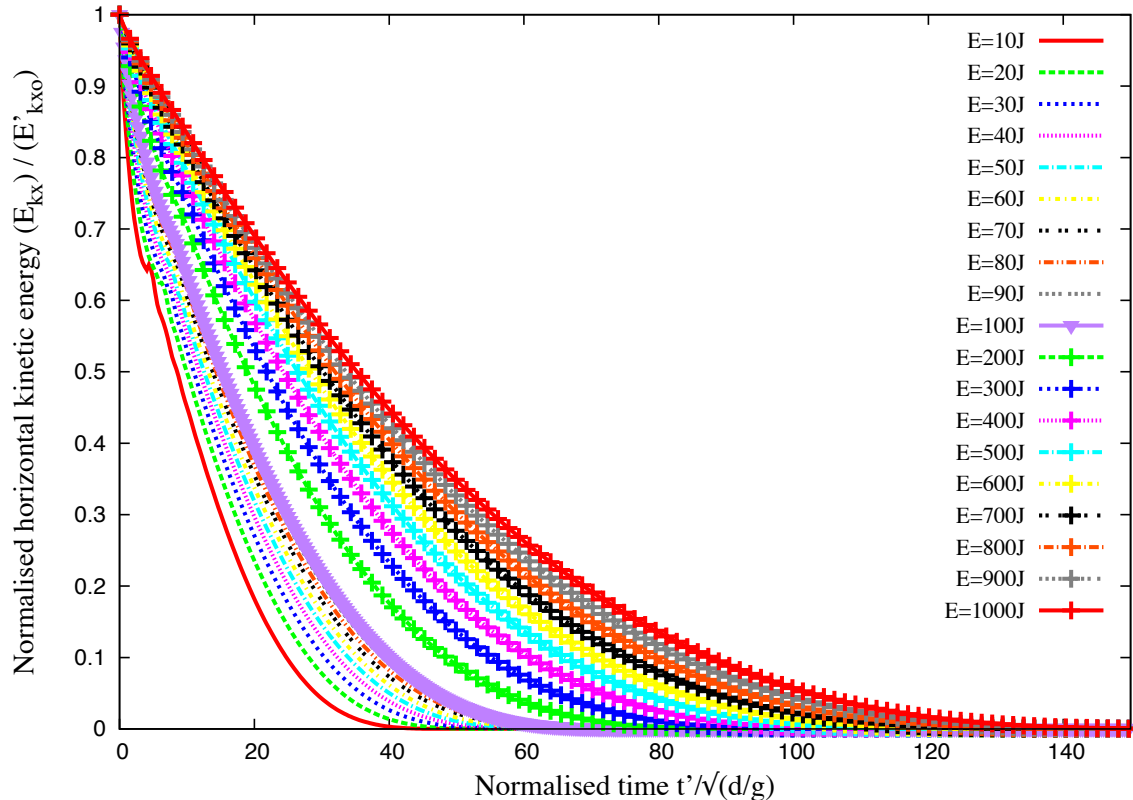


Figure 4.38 Evolution of kinetic energy in the x component of the velocity field normalised by the available kinetic energy at the end of the transient phase as a function of time elapsed since the same instant (MPM).

803 The scaling of the data with the decay time τ suggests that the run-out time, since the
 804 beginning of the second phase, t'_f might be a simple function of τ . Figure 4.40a shows both t'_f
 805 and τ as a function of E'_{x0} , where a power-law relation can be observed for both time scales.
 806 The run-out time $t'_f \propto (E'_{x0})^{\beta'}$ has the same exponent $\beta' \simeq 0.33 \pm 0.02$ as t_f as a function of
 807 E_0 . For the decay time we have $\tau \propto (E'_{x0})^{\beta''}$ with $\beta'' \simeq 0.38 \pm 0.03$. The relation between
 808 the two times can thus be expressed as (figure 4.40b)

$$809 \quad t'_f = k \tau (E'_{x0})^{\beta'' - \beta'}, \quad (4.13)$$

810 where $k \simeq 5.0 \pm 0.4$ and $\beta'' - \beta' \simeq 0.05 \pm 0.05$. This value is small enough to be neglected.
 811 It is therefore plausible to assume that the run-out time is a multiple of the decay time and
 812 the spreading process is controlled by a single time. A weak dependence on the energy E'_{kx0}
 813 is consistent with the fact that the energy available at the beginning of the second phase is
 814 not dissipated in the spreading process (calculated from the position of the tip of the pile)
 815 since the pile keeps deforming by the movements of the grains at the free surface even when

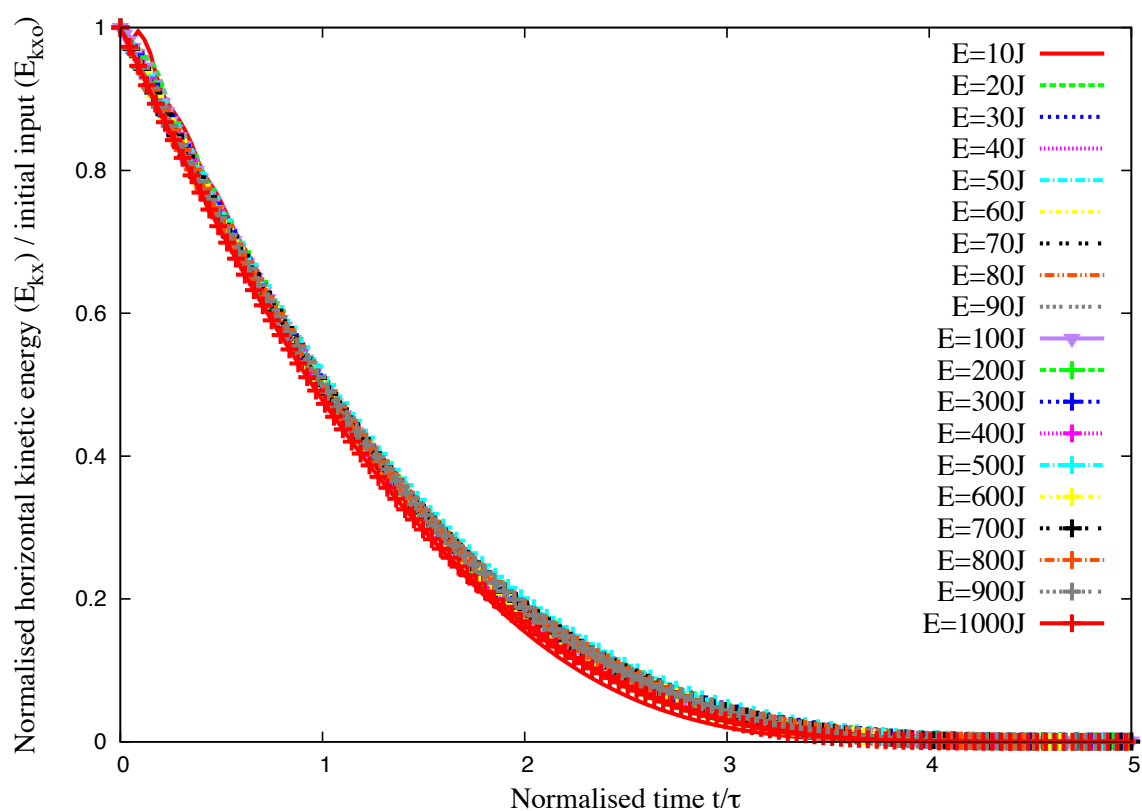


Figure 4.39 Evolution of kinetic energy in the x component of the velocity field normalised by the available kinetic energy at the end of the transient as a function of normalised time (MPM).

816 the tip comes to rest. This can explain the small difference between the two exponents as
817 observed here.

818 **4.4.5 Effect of friction**

819 The run-out distance, duration of flow, and the dissipation of kinetic energy are controlled by
820 the input energy and collective dynamics of the whole pile. However, the run-out behaviour
821 is also expected to depend on the base friction. A series of simulations with different values
822 of base friction was performed using MPM to analyse the influence of friction on the run-out
823 behaviour. The influence of friction on the run-out behaviour for different input energies
824 is shown in figure 4.41a. The run-out distance decreases with increase in the basal friction.
825 The exponent of the power-law relation between the run-out and input energy has a weak
826 dependence on the base friction, however, the proportionality constant is affected by the
827 change in the base friction. This behaviour is similar to that observed in granular column
828 collapse with varying initial properties (Balmforth and Kerswell, 2005; Lajeunesse et al.,
829 2005).

830 CD simulations using different values of coefficient of restitution show no difference
831 in the run-out behaviour. At large input energies, the pile remains in a dense state so that
832 multiple collisions inside the pile occur at small time scales compared to the deformation
833 time. When the restitution coefficients are increased, more collisions occur during a longer
834 time interval but the overall energy dissipation rate by collisions remains the same. This
835 effect is a seminal example of collective effects which erase the influence of local parameters
836 at the macroscopic scale.

837 In contrast to the restitution coefficients, the effect of friction coefficient is quite important
838 for the run-out. MPM simulations with varying friction coefficient show that, both the run-out
839 distance and the decay time decrease as the friction coefficient is increased. This effect
840 is much more pronounced at low values of the friction coefficient. The run-out time, for
841 example, is reduced by a factor of approximately 4 as μ_s is increased from 0.1 to 0.2 while the
842 change in the run-out and duration is less affected with increase in friction coefficient. This
843 “saturation effect” can be observed in a systematic way in simple shear tests. The dissipation
844 rate may reach a saturation point where the dilation of granular materials and rolling of the
845 grains change in response to increase in friction coefficient (Estrada et al., 2008).

846 **Effect kinetic energy distribution**

847 Staron et al. (2005) observed that the distribution of kinetic energy in the granular system is
848 an essential factor for the run-out distance. In order to understand the influence of energy

4.4 Slopes subjected to horizontal excitation

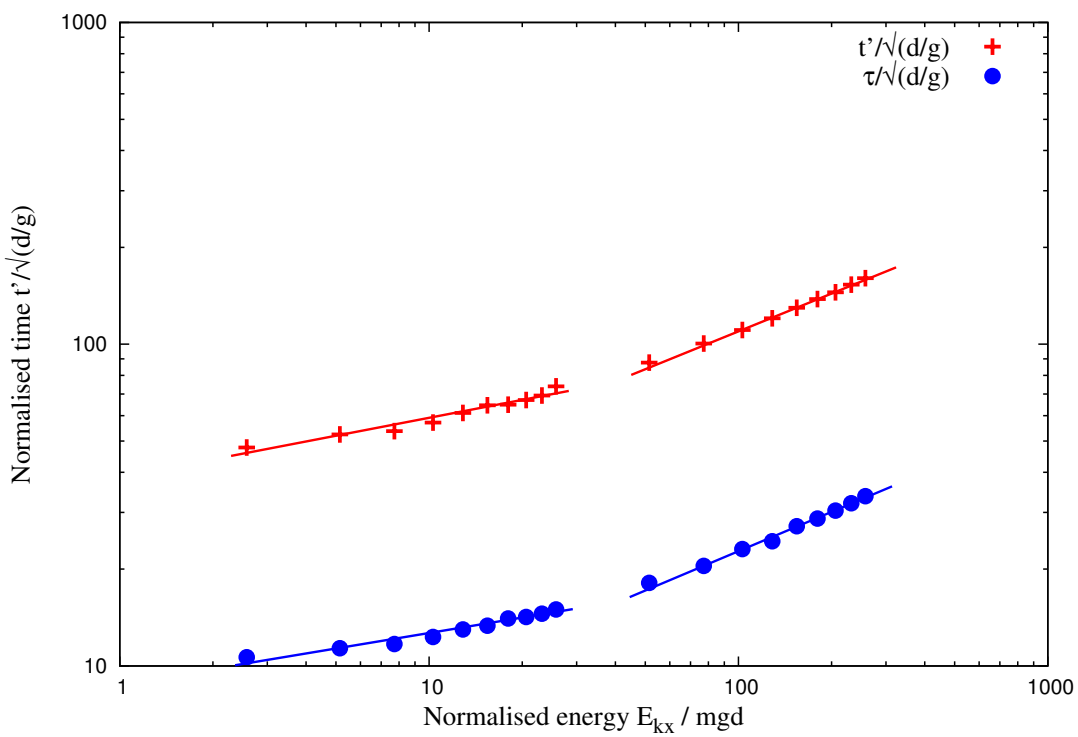
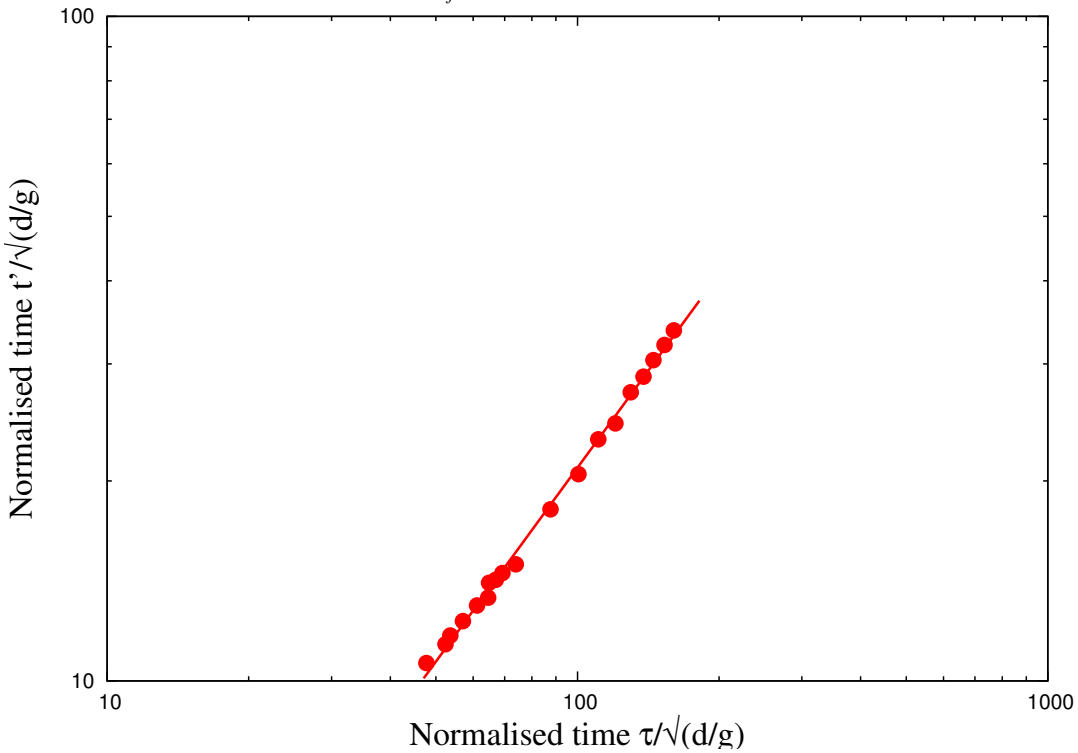
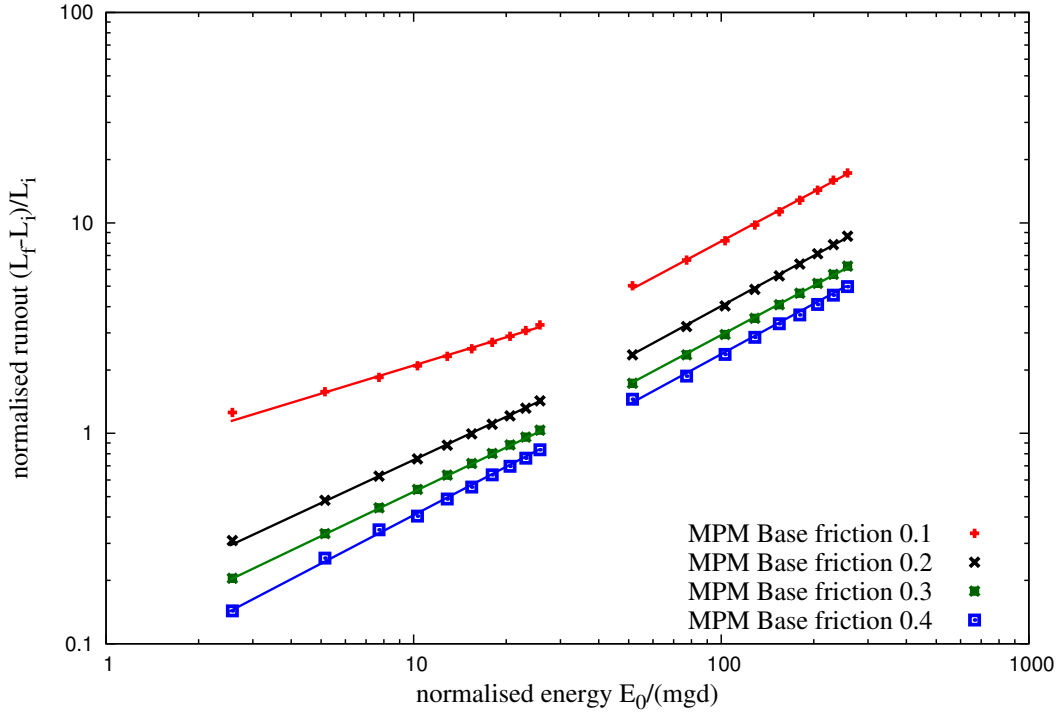
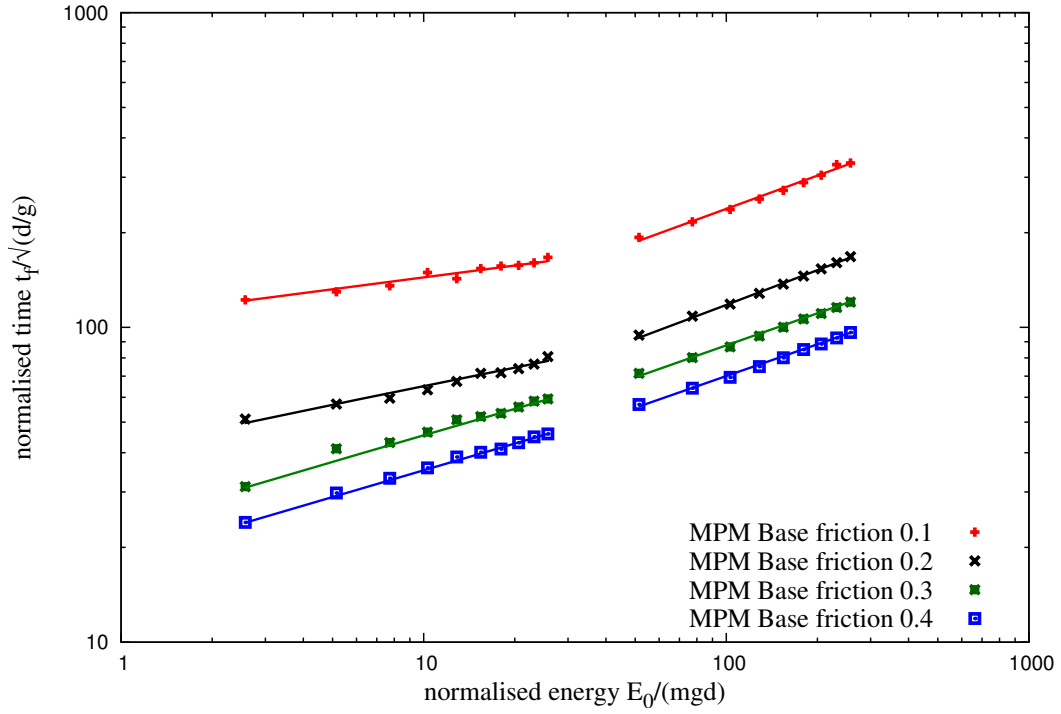
(a) Power law evolution of t'_f and τ as a function of kinetic energy E'_{kx0} .(b) Linear relationship between decay time and run-out time after the transient as a function of the normalised kinetic energy E_{kx0} .

Figure 4.40 Decay time and run-out time as a function of the normalised kinetic energy E_{kx0} .



(a) Effect of friction on the run-out distance



(b) Effect of friction on the duration of run-out.

Figure 4.41 MPM simulations of effect of friction on the run-out behaviour of slopes subjected to horizontal excitation.

4.4 Slopes subjected to horizontal excitation

63

distribution on the run-out behaviour, granular pile subjected to two different velocity fields
 are studied. A uniform velocity $V_{xo}(y) = V_0$ is applied to the entire pile, in contrast to
 the gradient horizontal velocity. Snapshots of flow kinematics at initial stages are shown
 in figure 4.42 (MPM simulations) and figure 4.43 (DEM). It can be observed from the figures
 that the continuum behaviour is identical to that of grain-scale simulations. As each grain
 experiences the same velocity, grains located at the top of the slope are pushed farther away
 and unlike the gradient input velocity, the cavity left behind the granular mass is not filled by
 the soil grains at the top.

Figure 4.44a shows the influence of velocity distribution on the run-out behaviour. At
 low input energy, the gradient velocity distribution shows significantly longer run-out in
 comparison to uniform velocity distribution. Section 4.4.4 shows that at low input energies a
 larger fraction of the energy is consumed in the destabilisation process. This means that the
 amount energy available for flow is less in uniform velocity distribution than the gradient
 velocity profile, this energy is even smaller as the initial velocity is distributed uniformly
 throughout the granular mass. However at higher input energy, where most of the energy
 is dissipated during the spreading phase, the run-out distance has a weak dependence on
 the distribution of velocity in the granular mass. The duration of the flow shows similar
 behaviour to the run-out, however, a slope subjected to a gradient velocity flows quicker than
 a slope subjected to a uniform horizontal velocity. The gradient velocity distribution provides
 more input energy at the initial stage to overcome the frictional resistance at the base. This
 shows that the material property and the distribution of kinetic energy in the system has a
 non-trivial influence on the flow kinematics and the internal flow structure.

4.4.6 Comparison with granular column collapse

871

Figure 4.45 shows the run-out behaviour of granular column collapse and the slope subjected
 to horizontal excitations as a function of normalised kinetic energy. In the case of column
 collapse, the peak energy at τ_c is used as the energy available for the flow. It can be observed
 that MPM and DEM predict similar run-out behaviour for low energy regime (short columns),
 which undergo frictional failure along the flanks. However MPM predicts longer run-out
 for high energy regime (corresponding to $a > 2.7$), where the granular column experiences
 significant collisional dissipation. The lack of a collisional energy dissipation mechanism in
 MPM results in over prediction of run-out distances. In the case of granular column subjected
 to horizontal velocity, the dissipation is friction and MPM is able to predict the run-out
 response in good agreement with DEM simulations. At very low energy, DEM simulations
 show longer run-out in the case of slope subjected to excitations due to local destabilisation
 at the flow front. Both granular flows, column collapse and slope subjected to horizontal

$t = 0 \text{ s}$



$t = 0.03 \text{ s}$



$t = 0.06 \text{ s}$



$t = 0.09 \text{ s}$



Figure 4.42 Snapshots of MPM simulations of the evolution of granular pile subjected to a gradient horizontal energy $E_0 = 61 \text{ mgd}$.

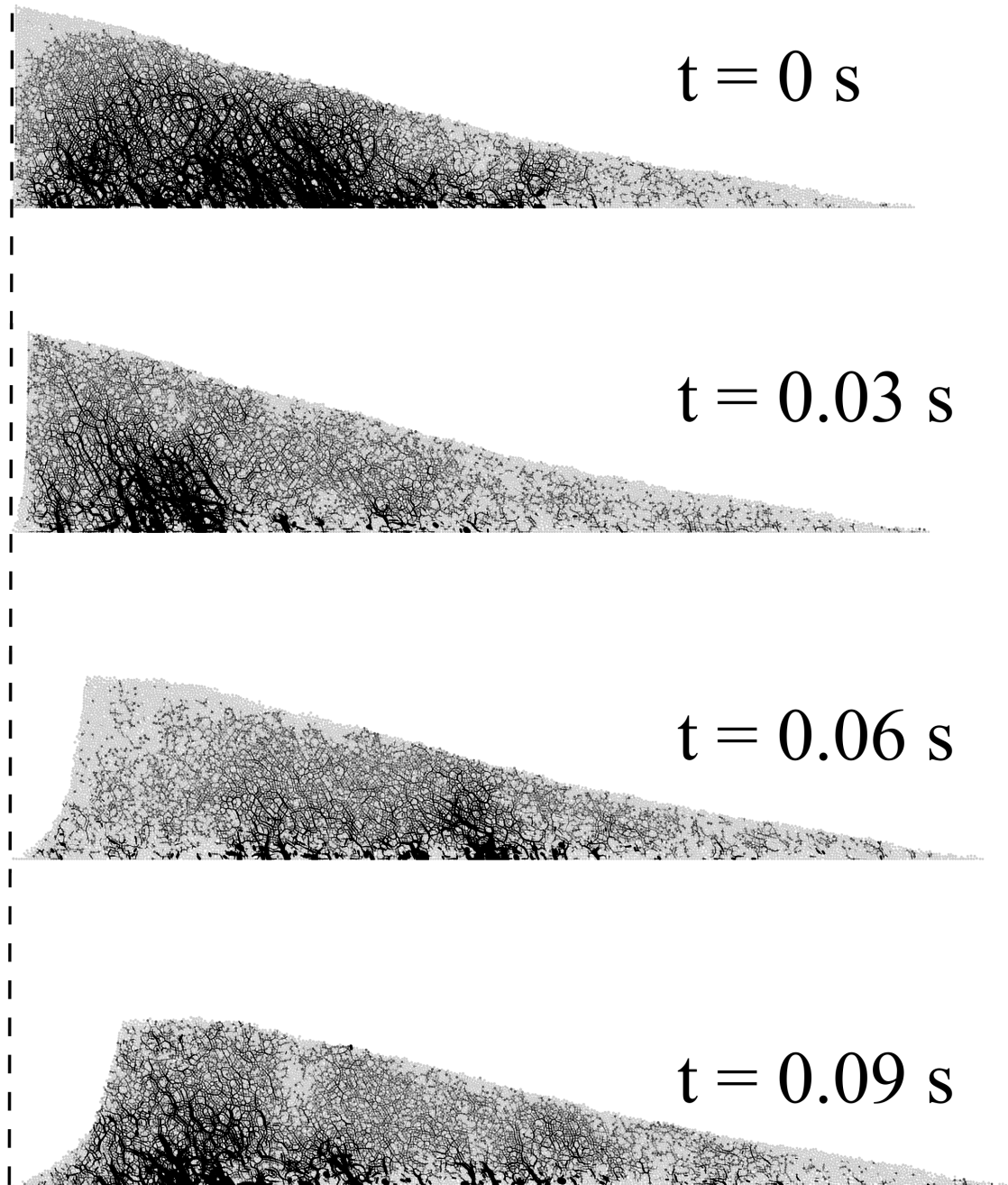
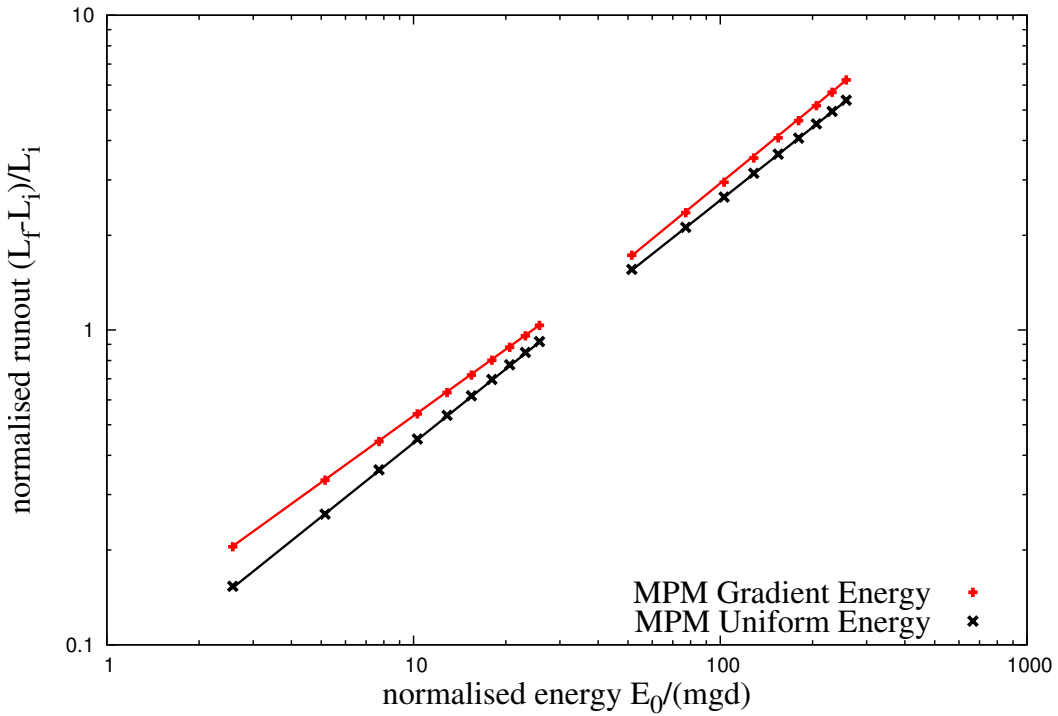
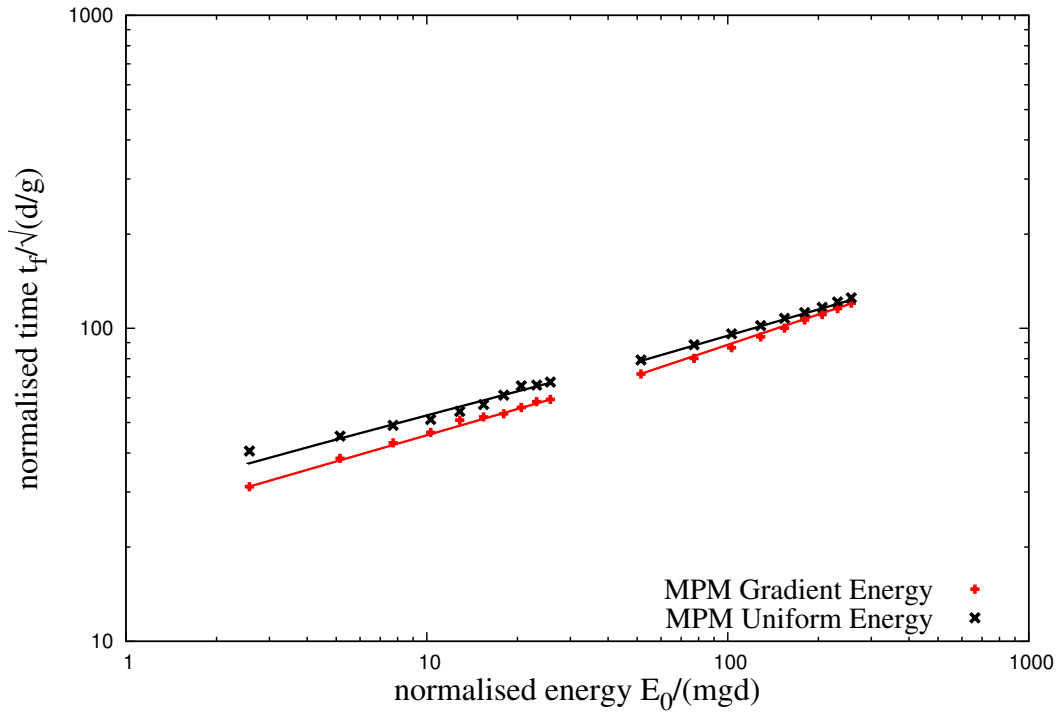


Figure 4.43 Snapshots of DEM simulations of the evolution of granular pile subjected to a gradient horizontal energy $E_0 = 61 \text{ mgd}$.



(a) Run-out distance as a function of normalised input kinetic energy.



(b) Duration of run-out as a function of normalised input kinetic energy.

Figure 4.44 Effect of input velocity distribution on the run-out behaviour of slopes subjected to horizontal velocities.

4.5 Summary

67

excitation, show power-law relation with the energy. This shows that the power-law behaviour is a granular flow characteristic. 884
885

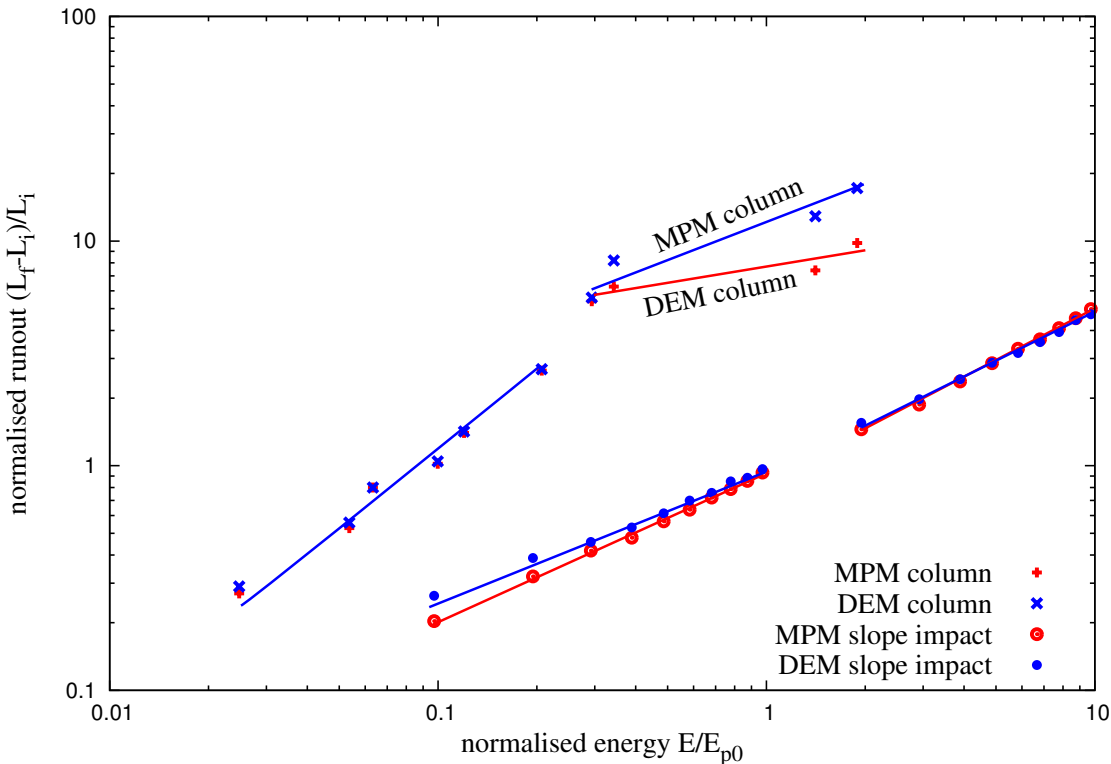


Figure 4.45 Comparison of the normalised run-out between the collapse of granular columns and granular slope subjected to horizontal loading.

4.5 Summary

886

Multi-scale simulations of dry granular flows were performed to capture the local rheology, and to understand the capability and limitations of continuum models in realistic simulation of granular flow dynamics. Previous studies on granular collapse have shown a power-law dependence between the run-out and the initial aspect ratio of the column. The change in the run-out behaviour for tall columns has remained unexplained. Continuum approach predict longer run-out distance, however, the reason for this behaviour was still lacking. Most studies were focused on mono-disperse grain sizes. In the present study, multi-scale simulations of granular column collapse are performed. Studies on the role of initial packing density and a poly-disperse sample on the run-out behaviour are also performed. The following conclusions can be derived based on MPM and DEM simulations of granular column collapse: 887
888
889
890
891
892
893
894
895
896

- 897 • Both DEM and MPM simulations show a power-law dependence of the run-out and
898 time with the initial aspect ratio of the column.
- 899 • A continuum approach, such as MPM, with a simple frictional dissipation model is
900 able to capture the flow kinematics of dry granular collapse for short columns. The
901 collapse of a short column is a frictional dissipation process.
- 902 • DEM simulations reveal collisional dissipation mechanism in the initial stage of
903 collapse of tall columns.
- 904 • MPM simulations show longer run-out behaviour in the case of tall columns. MPM sim-
905 ulation assumes that the total initial potential energy stored in the system is completely
906 dissipated through friction over the entire run-out distance. The lack of collisional
907 dissipation in MPM results in longer run-outs for tall columns.
- 908 • The initial configuration and the material properties have a significant influence on the
909 run-out behaviour. The run-out distance increases with increase in density of granular
910 packing. This effect is significant in the case of tall columns.
- 911 • DEM simulations with different initial packing shows evolution of packing density
912 with time. Hence it is important to consider macroscopic parameters like packing
913 fraction and dilatancy behaviour, which are due to meso-scale grain arrangements,
914 when modelling the granular system as a continuum.

915 Natural granular flows are triggered by different mechanisms. The distribution of kinetic
916 energy in the granular mass is found to have an effect on the flow kinematics. A multi-scale
917 analyses of a granular slope subjected to horizontal velocities are performed and the following
918 conclusions are derived:

- 919 • A power-law dependence of the run-out distance and time as a function of the input
920 energy is observed. The power-law behaviour is found to be a generic feature of
921 granular flow dynamics.
- 922 • The values of the power-law exponents are not simple functions of the geometry.
- 923 • Two regimes with different values of the exponents: a low-energy regime and a
924 high-energy regime are observed.
- 925 • The low energy regime reflects mainly the destabilisation of the pile, with a run-out
926 time independent of the input energy.

4.5 Summary

69

- The second regime is governed by the spreading dynamics induced by higher input energy. The evolution of granular slope in the high-energy regime can be described by a characteristic decay time, which is the time required for the input energy to decay by a factor of 0.5. 927
928
929
930
 - The run-out distance and the decay time decrease as the friction increases. This effect is much more pronounced at low values of friction. 931
932
 - At low input energy, the distribution of kinetic energy in the system is found have a significant effect on the run-out, as the energy is mostly consumed in the destabilisation process. 933
934
935
 - At higher input energy, where most of the energy is dissipated during the spreading phase, the run-out distance has a weak dependence on the distribution of velocity in the granular mass. 936
937
938
 - The duration of the flow shows similar behaviour to the run-out, however, a slope subjected to a gradient velocity flows quicker than a slope subjected to a uniform horizontal velocity. 939
940
941
 - The material property and the distribution of kinetic energy in the system has a non-trivial influence on the flow kinematics and the internal flow structure. 942
943
 - MPM is successfully able to simulate the transient evolution with a single input parameter, the macroscopic friction angle. 944
945
- This study exemplifies the ability of MPM, a continuum approach, in modelling complex granular flow dynamics and opens the possibility of realistic simulation of geological-scale flows on complex topographies. 946
947
948

Draft - v1.0

Tuesday 20th January, 2015 – 10:11

References

949

- Abe, K., Soga, K., and Bandara, S. (2013). Material Point Method for Coupled Hydromechanical Problems. *Journal of Geotechnical and Geoenvironmental Engineering*, 140(3). 950
951
- Balmforth, N. J. and Kerswell, R. R. (2005). Granular collapse in two dimensions. *Journal of Fluid Mechanics*, 538:399–428. 952
953
- Bandara, S. (2013). *Material Point Method to simulate Large Deformation Problems in Fluid-saturated Granular Medium*. PhD thesis, University of Cambridge. 954
955
- Bardenhagen, S. and Kober, E. (2004). The generalized interpolation material point method. *Computer Modeling in Engineering and Sciences*, 5(6):477–496. 956
957
- Cambou, B., Jean, M., and Radjaï, F. (2009). *Micromechanics of granular materials*. Wiley-ISTE. 958
959
- Coetzee, C. J., Vermeer, P. A., and Basson, A. H. (2005). The modelling of anchors using the material point method. *International Journal for Numerical and Analytical Methods in Geomechanics*, 29(9):879–895. 960
961
962
- Crosta, G. B., Imposimato, S., and Roddeman, D. (2009). Numerical modeling of 2-D granular step collapse on erodible and nonerodible surface. *Journal of Geophysical Research*, 114(F3):F03020. 963
964
965
- Da Cruz, F., Emam, S., Prochnow, M., Roux, J. N., and Chevoir, F. (2005). Rheophysics of dense granular materials: Discrete simulation of plane shear flows. *Physical Review E - Statistical, Nonlinear, and Soft Matter Physics*, 72(2):1–17. 966
967
968
- Daerr, A. and Douady, S. (1999). Two types of avalanche behaviour in granular media. *Nature*, 399(6733):241–243. 969
970
- Dey, R., Hawlader, B., Philips, R., and Soga, K. (2012). Effects of Shear Band Propagation on Submarine Landslide. In *Proceedings of the twenty-second International Offshore and Polar Engineering Conference*, Greece. International Society of Offshore and Polar Engineers (ISOPE). 971
972
973
974
- Estrada, N., Taboada, A., and Radjai, F. (2008). Shear strength and force transmission in granular media with rolling resistance. *Physical Review E*, 78(2):021301. 975
976
- Girolami, L., Hergault, V., Vinay, G., and Wachs, A. (2012). A three-dimensional discrete-grain model for the simulation of dam-break rectangular collapses: comparison between numerical results and experiments. *Granular Matter*, 14(3):381–392. 977
978
979

- 980 Guilkey, J., Harman, T., Xia, A., Kashiwa, B., and McMurtry, P. (2003). An Eulerian-
981 Lagrangian approach for large deformation fluid structure interaction problems, Part 1:
982 algorithm development. *Advances in Fluid Mechanics*, 36:143–156.
- 983 Hogg, A. J. (2007). Two-dimensional granular slumps down slopes. *Physics of Fluids*,
984 19(9):9.
- 985 Iverson, R. M. (1997). The physics of debris flows. *Rev. Geophys.*, 35(3):245–296.
- 986 Iwashita, K. and Oda, M. (1998). Rolling Resistance at Contacts in Simulation of Shear
987 Band Development by DEM. *Journal of Engineering Mechanics*, 124(3):285–292.
- 988 Jean, M. (1999). The non-smooth contact dynamics method. *Computer Methods in Applied
989 Mechanics and Engineering*, 177(3-4):235–257.
- 990 Kerswell, R. (2005). Dam break with Coulomb friction: A model for granular slumping?
991 *Physics of Fluids*, 17:057101.
- 992 Lajeunesse, E., Mangeney-Castelnau, A., and Vilotte, J. P. (2004). Spreading of a granular
993 mass on a horizontal plane. *Physics of Fluids*, 16(7):2371.
- 994 Lajeunesse, E., Monnier, J. B., and Homsy, G. M. (2005). Granular slumping on a horizontal
995 surface. *Physics of Fluids*, 17(10).
- 996 Larrieu, E., Staron, L., and Hinch, E. J. (2006). Raining into shallow water as a description
997 of the collapse of a column of grains. *Journal of Fluid Mechanics*, 554:259–270.
- 998 Lo, C. Y., Bolton, M., and Cheng, Y. P. (2009). Discrete element simulation of granular
999 column collapse. In *AIP Conf. Proc. Powders and Grains 2009*, volume 1145 of *6th
1000 International Conference on Micromechanics of Granular Media, Powders and Grains
1001 2009*, pages 627–630.
- 1002 Lube, G., Huppert, H. E., Sparks, R. S. J., and Freundt, A. (2005). Collapses of two-
1003 dimensional granular columns. *Physical Review E - Statistical, Nonlinear, and Soft Matter
1004 Physics*, 72(4):1–10.
- 1005 Marketos, G. and Bolton, M. D. (2009). Flat boundaries and their effect on sand testing.
1006 *International Journal for Numerical and Analytical Methods in Geomechanics*, pages
1007 n/a–n/a.
- 1008 Mast, C. M., Arduino, P., Mackenzie-Helnwein, P., and Miller, G. R. (2014). Simulating
1009 granular column collapse using the Material Point Method. *Acta Geotechnica*, page In
1010 print.
- 1011 Mitchell, J. K. and Soga, K. (2005). *Fundamentals of soil behavior*. John Wiley & Sons.
- 1012 Moreau, J. J. (1993). New computation methods in granular dynamics. In Thornton, C.,
1013 editor, *Powders and Grains*, page 227. A. A. Balkema.
- 1014 Mutabaruka, P. (2013). *Modélisation numérique des milieux granulaires immergés : initiation
1015 et propagation des avalanches dans un fluide*. Phd thesis, University of Montpellier 2.

- Radjai, F. and Dubois, F. (2011). *Discrete-element modeling of granular materials*. ISTE 1016
Wiley, London; Hoboken, N.J. 1017
- Radjai, F. and Richefeu, V. (2009). Contact dynamics as a nonsmooth discrete element 1018
method. *Mechanics of Materials*, 41(6):715–728. 1019
- Radjai, F., Schafer, J., Dipple, S., and Wolf, D. (1997). Collective Friction of an Array of 1020
Particles: A Crucial Test for Numerical Algorithms. *Journal de Physique I*, 7(9):1053– 1021
1070. 1022
- Rondon, L., Pouliquen, O., and Aussillous, P. (2011). Granular collapse in a fluid: Role of 1023
the initial volume fraction. *Physics of Fluids*, 23(7):073301–073301–7. 1024
- Rycroft, C. H., Orpe, A. V., and Kudrolli, A. (2009). Physical test of a particle simulation 1025
model in a sheared granular system. *Physical Review E*, 80(3):031305. 1026
- Staron, L. and Hinch, E. J. (2007). The spreading of a granular mass: Role of grain properties 1027
and initial conditions. *Granular Matter*, 9(3-4):205–217. 1028
- Staron, L., Radjai, F., and Vilote, J. P. (2005). Multi-scale analysis of the stress state in 1029
a granular slope in transition to failure. *The European physical journal. E, Soft matter*, 1030
18(3):311–20. 1031
- Topin, V., Monerie, Y., Perales, F., and Radjaï, F. (2012). Collapse Dynamics and Runout of 1032
Dense Granular Materials in a Fluid. *Physical Review Letters*, 109(18):188001. 1033
- Utili, S., Zhao, T., and Houlsby, G. (2014). 3D DEM investigation of granular column 1034
collapse: Evaluation of debris motion and its destructive power. *Engineering Geology*, 1035
page In print. 1036
- Warnett, J. M., Denissenko, P., Thomas, P. J., Kiraci, E., and Williams, M. A. (2013). Scalings 1037
of axisymmetric granular column collapse. *Granular Matter*, 16(1):115–124. 1038
- Zenit, R. (2005). Computer simulations of the collapse of a granular column. *Physics of 1039
Fluids*, 17(Compendex):031703–1–031703–4. 1040